

# Modelling the Installation of a Cone

Using a 2D-Axisymmetric Material Point Method Model

J.W.T.A. Schuringa

  
**TU Delft**

**FUGRO**



# Modelling the Installation of a Cone

## Using a 2D-Axisymmetric Material Point Method Model

by

J.W.T.A. Schuringa

to obtain the degree of Master of Science  
at the Delft University of Technology,  
to be defended publicly on Friday January 24, 2020 at 3:00 PM.

Student number: 4174089

Project duration: 23 April 2019 – 24 January 2020

Supervisors: Dr. P.J. Vardon, TU Delft  
Dr. F. Pisanò, TU Delft  
Dr. ir. W. Broere, TU Delft  
Dr. M. Martinelli, TU Delft  
ir. L.W. Schadee, Fugro

An electronic version of this thesis is available at <http://repository.tudelft.nl/>.



*“An opportunity of a lifetime must be seized within the lifetime of the opportunity”*

- Leonard Ravenhill

## Acknowledgements

*Den Haag, 15-01-2020*

This document marks the end of my time as a student of the Technical University of Delft. In this period I have had the pleasure to meet a lot wonderful people which have helped reach this moment. I would like to express my gratitude to a few people which have provided support during this final piece of work.

First of all I would like to thank my graduation committee Phil Vardon, Federico Pisanò, Wout Broere, Mario Martinelli and Leon Schadee for their guidance and for the feedback they have provided during all the meetings. Especially Mario Martinelli who has helped me a lot with the modelling process and Leon Schadee for the additional discussions and guidance at Fugro.

Secondly, I would like to express my gratitude to the colleagues at Fugro for the pleasant working environment and support. A special thanks to Jeroen for all the discussions leading to essential insights, coffee breaks and of course for letting me win once during one of our two dozen ping-pong matches. I strongly believe it is a good thing they had to store the table due to a lack of office space since I would probably not be writing this passage right now if they hadn't.

I would like to thank my family for their continuous support. My friends from the Geo-Engineering group for the wonderful two and a half years. And finally Rosa for her never-ending support and patience during the majority of my studies. I could not have done it without you.

Johan Schuringa

**Abstract**

In this work the installation process of a cone penetrating into a sand system is modelled using a 2D-axisymmetric material point method (MPM) model in order to investigate the installation processes and to predict the plastic radius. One meter of cone penetration is modelled under a surcharge of 50 kPa. The used constitutive model is Mohr-Coulomb Strain Softening (MCSS). The validation of the model has been conducted by comparing the MPM results to those obtained from laboratory experiments performed by Arshad et al. (2014). It was found that the qualitative behaviour from the MPM model and the experiments were in agreement but the quantitative behaviour showed some discrepancies. These discrepancies could be caused by the fact that, in the MCSS model, the stiffness is constant and independent of stress which it is not in reality. The performed sensitivity analysis showed that the stiffness has the most influence on the numerical predictions further adding to the importance of accurately capturing the soil stiffness throughout the simulation. The 2D-axisymmetric MPM model showed to have the potential to be a good tool for modelling the installation process of a cone and predicting the plastic radius.

# Contents

<b>Preface</b>	<b>i</b>
Acknowledgements . . . . .	i
Abstract . . . . .	ii
List of Figures . . . . .	v
List of Tables . . . . .	vi
<b>1 Introduction</b>	<b>1</b>
1.1 Background Information . . . . .	1
1.2 Objectives and Limitations . . . . .	1
1.3 Research Questions . . . . .	2
1.4 Thesis Outline . . . . .	2
<b>2 Literature Study</b>	<b>3</b>
2.1 Introduction . . . . .	3
2.2 The Pressuremeter . . . . .	3
2.2.1 Introduction . . . . .	3
2.2.2 Types of Pressuremeters . . . . .	4
2.2.2.1 Prebored Pressuremeter . . . . .	5
2.2.2.2 Self-bored Pressuremeter . . . . .	5
2.2.2.3 Pushed-in Pressuremeter . . . . .	6
2.2.3 Analytical Solution . . . . .	7
2.2.3.1 Basic Stress-Strain-Deformation Concept . . . . .	7
2.2.3.2 Cavity Expansion Theory . . . . .	10
2.2.3.3 The Expansion Curve . . . . .	11
2.2.4 Installation Effects . . . . .	13
2.2.5 Conclusion . . . . .	16
2.3 Numerical Methods . . . . .	17
2.3.1 Introduction . . . . .	17
2.3.2 Spatial Discretization . . . . .	17
2.3.3 Small-Medium Deformation Models: Finite Element Method . . . . .	18
2.3.4 Large Deformation Models: Material Point Method . . . . .	19
2.3.4.1 Mathematical Formulation . . . . .	20
2.3.4.2 Impact/Contact Formulation . . . . .	20
2.3.4.3 Moving Mesh . . . . .	21
2.3.4.4 2D-Axisymmetric Formulation . . . . .	21
2.3.5 Comparison Between FEM and MPM . . . . .	21
2.3.6 Constitutive Models . . . . .	22
2.3.6.1 Basic Principles Soil Modelling . . . . .	24
2.3.6.2 Elastic-Plastic Models . . . . .	24
2.3.6.3 Hardening and Softening . . . . .	25
2.3.6.4 Limitations of Soil Models . . . . .	25
2.3.7 Conclusion . . . . .	26
2.4 Modelling of a Pressuremeter Test . . . . .	27
2.4.1 Modelling of the Installation . . . . .	27
2.4.2 Conclusion . . . . .	29

<b>3</b>	<b>Model Verification</b>	<b>30</b>
3.1	Introduction . . . . .	30
3.2	Mesh Description . . . . .	30
3.2.1	2D-Axisymmetric Formulation and Conversion to 3D . . . . .	30
3.2.2	Mesh Size . . . . .	31
3.2.3	Mesh Refinement . . . . .	37
3.3	Material Points . . . . .	38
3.4	Model Features . . . . .	40
3.4.1	Surcharge . . . . .	40
3.4.2	Moving Mesh . . . . .	42
3.4.3	Strain Smoothing . . . . .	42
3.5	Constitutive Model . . . . .	43
3.6	Calculation Method . . . . .	44
3.7	Determination of the Plastic Radius . . . . .	46
3.8	Conclusion . . . . .	49
<b>4</b>	<b>Model Validation</b>	<b>50</b>
4.1	Introduction . . . . .	50
4.2	Validation Strategy . . . . .	50
4.2.1	Experimental Data . . . . .	50
4.2.2	Image-Based Analysis . . . . .	51
4.2.3	Empirical Correlations . . . . .	53
4.3	Numerical Simulations . . . . .	54
4.3.1	Model Series . . . . .	54
4.3.2	Results . . . . .	54
4.4	Conclusion . . . . .	61
<b>5</b>	<b>Sensitivity Analysis</b>	<b>62</b>
5.1	Introduction . . . . .	62
5.2	Parameter Sensitivity of the Cone Resistance . . . . .	63
5.2.1	Variation of the Shear Modulus $G$ . . . . .	63
5.2.2	Variation of the Peak Friction Angle $\phi'_{max}$ . . . . .	64
5.2.3	Variation of the Peak Dilatancy Angle $\psi_{max}$ . . . . .	65
5.2.4	Variation of $\phi'_{max}$ and $\psi_{max}$ combined . . . . .	65
5.2.5	Variation of the Shape Factor $\eta$ . . . . .	67
5.2.6	Summary of Parameter Sensitivity of Cone Resistance . . . . .	67
5.3	Parameter Sensitivity of the Plastic Radius . . . . .	69
5.4	Conclusion . . . . .	71
<b>6</b>	<b>Conclusions &amp; Recommendations</b>	<b>72</b>
6.1	Conclusions . . . . .	72
6.2	Recommendations . . . . .	74
	<b>References</b>	<b>74</b>
	<b>Appendices</b>	<b>78</b>
A	Meshes Used for Mesh Refinement Analysis . . . . .	80
B	Final Mesh . . . . .	81
C	Test Series Performed by Arshad et al. (2014) . . . . .	83
D	Strain paths of elements in MPM model . . . . .	85

# List of Figures

2.1	Definition of a pressuremeter (Clarke, 2014) . . . . .	4
2.2	Schematics of PBP (Ali et al., 2016), SBP (Cambridge Insitu, 2018) & CPM (Cambridge Insitu, 2019) . . . . .	5
2.3	Change of length in the radial direction (Wierzbicki, 2013) . . . . .	7
2.4	Two deformation modes responsible for the circumferential strain (Wierzbicki, 2013) . . . . .	8
2.5	Prapaharan & Thevanayagam (1989) . . . . .	9
2.6	Stress field for purely elastic soil (Baguelin et al., 1978) . . . . .	10
2.7	Stress field for an elastic plastic soil (Baguelin et al., 1978) . . . . .	11
2.8	Different types of expansion curves. (a) PBP, (b) SBP & (c) PIP (Clarke, 2014) . . . . .	12
2.9	Different Disturbance Types . . . . .	14
2.10	Overpushing disturbance: (a) pressuremeter curve; (b) apparent and true stress-strain curves (Silvestri, 2004). . . . .	15
2.11	MPM procedure for one time step (Zhang et al., 2017) . . . . .	20
2.12	Model used by Moug et al. (2019) . . . . .	27
2.13	Geometry and discretization of the model used by Ceccato et al. (2016) . . . . .	28
2.14	Cone resistance profile from MPM analysis (Tehrani & Galavi, 2018) . . . . .	29
3.1	Conversion of forces in 2D to stresses in 3D for the cone tip . . . . .	30
3.2	Cone resistance profile for different mesh sizes . . . . .	32
3.3	Location of the stress state cross-sections . . . . .	32
3.4	Horizontal stresses at different cross-sections in radial direction . . . . .	33
3.5	Vertical stresses at different cross-sections in radial direction . . . . .	34
3.6	Horizontal stresses at different cross-sections in vertical direction . . . . .	35
3.7	Vertical stresses at different cross-sections in vertical direction . . . . .	35
3.8	Horizontal stresses at cross-section $E' - E'$ . . . . .	36
3.9	Vertical stresses at cross-section $E' - E'$ . . . . .	36
3.10	Cone resistance profiles for mesh refinement analysis . . . . .	37
3.11	Mesh dependency of model . . . . .	38
3.12	Unstructured mesh along the shaft . . . . .	38
3.13	General MP density distribution . . . . .	39
3.14	$K_0$ stresses with 50 kPa surcharge . . . . .	40
3.15	Vertical stress contour plot . . . . .	41
3.16	Moving mesh concept: (a) Initial state, (b) End of simulation (Phuong, 2019) . . . . .	42
3.17	Example of kinematic locking in MPM/FEM modelling (Ceccato et al., 2019) . . . . .	43
3.18	Effect of shape factor on strain softening rate (Ceccato et al., 2019) . . . . .	44
3.19	Cone resistance profiles to investigate strain softening behaviour . . . . .	45
3.20	Cone resistance profile for both calculation methods . . . . .	45
3.21	Plastic Radius at 0.5m depth . . . . .	46
3.22	Radius at 0.5m depth where the soil has fully softened . . . . .	47
3.23	Mohr circle close to the cone . . . . .	48
3.24	Stress state as function of radial distance . . . . .	48
4.1	Volumetric strain development from DIC analysis by Arshad et al. (2014) . . . . .	52
4.2	Strain contour plots of 45% relative density test (Arshad et al., 2014) . . . . .	52
4.3	Strain contour plots of 82% relative density test (Arshad et al., 2014) . . . . .	53

4.4	Comparison between experimental data (derived from Arshad et al. (2014)) and the empirical relationship by Salgado & Prezzi (2007)	53
4.5	Comparison between the MPM models, the experimental data and the empirical relationship	55
4.6	Comparison of contour plots of $\varepsilon_{rr}$	56
4.7	Comparison of contour plots of $\varepsilon_{zz}$	57
4.8	Comparison of contour plots of $\varepsilon_{rz}$	58
4.9	Comparison of contour plots of $\varepsilon_{vol}$	59
4.10	Strain paths comparison for element E. Left: experiments; Right: MPM model	60
4.11	Strain paths comparison for element B. Left: experiments; Right: MPM model	61
5.1	Cone resistance profiles for different shear moduli	63
5.2	Oscillations for lowest and highest shear modulus	63
5.3	Steady state cone resistance for different shear moduli	64
5.4	Cone resistance profile for different peak friction angles	65
5.5	Cone resistance profile for different peak dilatancy angles	66
5.6	Steady state cone resistance for different peak dilatancy angles	66
5.7	Cone resistance profile for different peak friction and dilatancy angles	67
5.8	Cone resistance profile for different shape factors	68
5.9	Tornado plot of parameter sensitivity of the cone resistance	68
5.10	Tornado plot of parameter sensitivity of the plastic radius	69
5.11	Stress state over radial distance including the Mohr circle at plastic radius	70
5.12	Stress state over radial distance including the Mohr circle at plastic radius	70
5.13	Tornado plot of the overestimation of the plastic radius	71
A.1	Meshes for models MR1, MR2 and MR3 (from left to right)	80
A.2	Meshes for models MR4, MR5 and MR6 (from left to right)	80
A.3	Full mesh	81
A.4	Zoomed view of the mesh near the cone	82
A.5	Test serie performed by Arshad et al. (2014)	83
A.6	Cone resistance, $q_c$ , for tests with a 50kPa surcharge (Arshad et al., 2014)	84
A.7	Strain paths comparison for element B. Left: experiments; Right: MPM model	85
A.8	Strain paths comparison for element C. Left: experiments; Right: MPM model	85
A.9	Strain paths comparison for element D. Left: experiments; Right: MPM model	86
A.10	Strain paths comparison for element E. Left: experiments; Right: MPM model	86

## List of Tables

3.1	Different mesh sizes used for boundary effects analysis	31
3.2	Model parameters for mesh refinement analysis	37
4.1	Properties of #2Q-ROK sand (Arshad et al., 2014)	51
4.2	Input parameters MPM models	54
5.1	Input parameters MC Strain Softening model	62
5.2	Input parameters for sensitivity analysis	62
5.3	Steady state cone resistance for different shear moduli	64

# Chapter 1

## Introduction

### 1.1 Background Information

In soil mechanics, knowing the properties of the subsoil is an important aspect for all geotechnical problems. In order to better understand the subsoil, many different types of tests can be conducted. These consist of laboratory tests like the triaxial test, in-situ tests like a cone penetration test and making numerical predictions using finite element calculations. All types of tests have different advantages and disadvantages. Laboratory tests are performed in a controlled environment, but the sample is almost inevitably disturbed in a way. In-situ tests can be performed in undisturbed soil but boundary conditions are not always known. In simulation testing, the boundary conditions can be exactly defined and are relatively cheap. However, simulations have to be validated to ensure that the results represent the actual mechanisms in the soil.

One of the in-situ tests is the pressuremeter test. This test assesses both the strength and the stiffness of the soil by expanding a membrane located at depth and measuring the pressure needed to displace the soil. The pressuremeter can be installed in several ways: Pre-bored, self-boring or pushed into the soil. A pressuremeter test will, regardless of the installation method used, always introduce some level of disturbance to the soil directly surrounding the pressuremeter module. This disturbance results in the first part of the obtained expansion curve being practically unusable for the determination of the in-situ soil stiffness. While the self-boring pressuremeter result in the least amount of disturbance, the pushed-in pressuremeter is known to introduce the most repeatable amount of disturbance much like the cone penetration test. This repeat-ability of the test has peaked the interest of engineers for years and has ultimately led to the development of the cone pressuremeter (CPM). The current CPM is a quasi-static test which is able to determine the engineering strength and stiffness of soil. However, for off-shore applications, the dynamic soil properties are also of interest. This has led to the initiation of a research project between Fugro and the TU Delft to develop a dynamic cone pressuremeter (DCPM) which should be capable to determine the dynamic in-situ properties of the soil. In order to assess the feasibility of this new device, research has to be conducted using numerical models. One of the first aspects which has to be addressed is the disturbance of the soil due to the installation of the CPM module. This will enable future numerical models, which will simulate the actual DCPM test, to be calibrated in terms of the initial stress state in the soil after the installation of the cone. Since the installation of a cone is accompanied with large deformations, using the material point method (MPM) is chosen as the method to simulate this problem.

### 1.2 Objectives and Limitations

In order to improve the determination of the soil parameters from a cone pressuremeter test, the disturbance of the soil surrounding the pressure model should be accounted for when processing the test data. Several problems complicate this:

- The behaviour of the soil next to the shaft during the installation is complex.
- In-situ measurements of the disturbance due to installation are impossible to obtain.
- Most analytical methods that calculate stresses and strains during the installation process rely on simplifications and assumptions which omit essential mechanisms that drive the disturbance. This makes using these methods to validate the numerical results difficult.

Therefore, the goal of this research is to model the installation effects of a cone pressuremeter test using a material point method code and assess the level of disturbance typically encountered with pushing a cone into the soil. These installation effects are a change in stress state and, for granular soils, a change in void ratio. How many aspects of the behaviour can be modelled depends on the

constitutive model. The installation of a cone into the soil is in essence an axisymmetric problem. The MPM code, provided by Deltares, is able to simulate 2D axisymmetric problems and will therefore be used in this research. In terms of soil types different options can be chosen. Given the standard CPT penetration speed of 0.02 m/s, each option will simulate a separate soil behaviour; Drained behaviour for sand, undrained behaviour for clay and partially drained for peat or silt like soils. In this thesis, the installation in sand will be researched. Initially, a simple state independent model (e.g. Mohr-Coulomb) will be used to setup the model. The Mohr-Coulomb model will introduce certain limitations (Chen, 2013). For example, the negligence of the influence of the intermediate principle stress. Also, strain softening is not taken into account in the linear elastic-perfectly plastic model. There are, however, Mohr-Coulomb based models which can take strain softening into account. Using a state independent model does also limit the research to the use of a state dependent models like the critical state models. This limitation could induce disagreements between the model and the experimental data.

The validation process of the model will be done by using a combination of experimental data and empirical correlations. For the experimental data, the aim is to use calibration chamber data and DIC/PIV data to compare the qualitative behaviour. The cavity expansion theory will be used as a theoretical verification of the obtained plastic radius. The previous work of i.e. Ceccato et al. (2016) will be used as a reference point for the models. After the model is calibrated and properly set up in terms of geometry, element size, particle distribution and parameters, a sensitivity analysis will be performed in order to assess influence of the different parameters and the robustness of the solution.

It must be noted that this research focuses solely on the initial quasi-static installation process of a CPM and that, even given that the envisioned DCPM is a dynamic device, no dynamics are considered in this work.

### 1.3 Research Questions

The main research question of this work is formulated as follows:

*‘Can the installation effects, which are the result of a cone pressuremeter penetrating the soil, be accurately modelled in a 2D-axisymmetric model using the material point method?’*

In order to answer this question, the following points can be considered the main objectives of this research: (1) Setting up the model: Creating and verifying a model for sand, (2) Model validation: Validate the model using available data, analytical solutions and previous research and (3) Sensitivity analysis: Small differences in input can lead to large differences in output. From these objectives, a set of sub-questions can be formulated:

- *‘What is the most suitable, currently available, elastic-plastic constitutive model in order the model the installation effects of a cone pressuremeter?’*
- *‘Can the MPM model be validated using experimental and image-based data?’*
- *‘What parameter(s) have the most influence of the installation effects encountered with the installation of a cone pressuremeter?’*

### 1.4 Thesis Outline

This thesis consists of six chapters. In Chapter 2, the literature study is presented explaining the basis for this research. Chapter 3 will give the verification of the model which is used in this research. Chapter 4 presents the validation process of the model using a combination of various validation methods. Next, in Chapter 5, a sensitivity analysis is conducted to further understand the influence of the parameters on the results. Lastly, Chapter 6 presents the conclusions and recommendations.

# Chapter 2

## Literature Study

### 2.1 Introduction

This chapter contains the literature study which has been conducted prior to this research. The literature study consists of three sections. Firstly, the pressuremeter device is elaborated. Following that, a selection of numerical methods are explained. Lastly, a selection of previous research work relevant to this research is discussed.

### 2.2 The Pressuremeter

#### 2.2.1 Introduction

The pressuremeter is a device well suited for directly assessing the both the in situ shear stiffness and strength parameters of soils. The definition of a pressuremeter which is internationally recognised by the ISSMFE is as follows:

*‘A pressuremeter is a cylindrical probe that has an expandable flexible membrane designed to apply a uniform pressure to the walls of a borehole.’*

In this thesis, the definition of a pressuremeter test is the same as used by Clarke (2014). This definition states that the pressuremeter test is the expansion of the membrane after the probe is installed in the test pocket. Pressure and displacement are monitored during a test and these data are used to produce a stress-strain curve from the which design parameters or ground properties are determined. Figure 2.1 shows the general set up of a pressuremeter. The stress and strain level acting around the pressuremeter during test does influence the measured stiffness. Therefore, the correct interpretation and application of the test results are an important factor (Bellotti et al., 1989).

The pressuremeter is primarily used for determining the shear modulus,  $G$ . The shear modulus can be obtained from the local slope of parts of the pressure/strain test curve. Multiple cycles or ‘loops’ are taken during the test, giving several estimates of modulus and revealing the strain and stress dependency of the modulus. In soils, these cycles appear hysteretic and this non-linearity allows the degradation of stiffness with increasing strain to be described (Bolton & Whittle, 1999). In a drained expansion the mean effective stress in the surrounding material increases throughout the loading, and so does the shear modulus. It is not straightforward to quantify this stress dependency. Whittle & Liu (2013) is a published solution that specifically addresses this problem, but at least three unload/reload cycles are needed and the disturbance of the soil further limits the use of the solution.

In a pressuremeter test the material is sheared and thus the modulus obtained is the shear modulus,  $G$ . If the Young’s modulus,  $E$ , is required then, provided the material is isotropic, the following relationship applies:

$$E = 2G(1 + \nu) \quad (1)$$

Where  $\nu$  is Poisson’s ratio. The shear modulus is derived from a horizontally oriented cavity expansion and may need to be adjusted when used to calculate vertically influenced deformation.

One of the more difficult aspect of the pressuremeter test is providing reliable values for the insitu lateral stress  $\sigma_{ho}$ , and subsequently the coefficient of earth pressure at rest,  $K_0$ . For undrained conditions, the analysis by Houlsby & Withers (1988) can be used but the estimates will be high unless the some modifications which take account of the non-linearity in the elastic phase of the test are applied (Bolton & Whittle, 1999). This section first describes the different types of pressuremeters which have been developed over the years. Following that, the analytical solution from which the stiffness parameters can be derived is discussed along with the underlying theories.

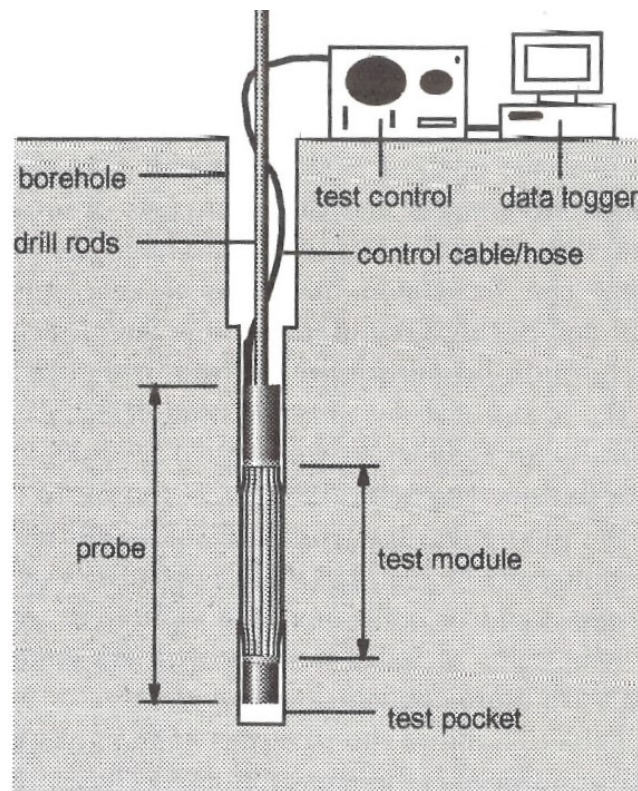


**Figure 2.1:** Definition of a pressuremeter (Clarke, 2014)

### 2.2.2 Types of Pressuremeters

In this subsection the different types of pressuremeters (PM) are explained. During a pressuremeter test, a module is brought to depth and a membrane is then expanded by forcing water, oil or gas into the module. This gives a direct relationship between the pressure and subsequent expansion of the cavity. There exists different types of pressuremeter tests. The different types of pressuremeter generally look the same but they differ in detail. They can be categorized by the method of installation. The installation of the test module to the required depth can be divided in three categories:

- Prebored pressuremeters (PBP)
- Self-boring pressuremeters (SBP)
- Pushed-in pressuremeters (CPM)

Figure 2.2 shows a schematic of each type of pressuremeter. Each category can subsequently be divided in two groups by the way the movement of the membrane is measured. The movement of the membrane can be monitored by using displacement transducers in the probe or by observing the amount of fluid forced into the probe. The first method are radial displacement type probes. The second method are described as volume displacement type probes. For this test the volume of the membrane is assumed to remain constant as it expands. Therefore, the measured change in volume of water or oil injected is equal to the change in volume of the pocket. This gives direct measurements of the average displacement of the cavity wall. For the radial displacement type probes, the displacements of the inner surface of the membrane are given at several points. Displacement transducers include linear variable differential transformers, Hall effect gauges and strain gauges. The thickness of the membrane reduces as the membrane is expanded hence the measured displacement must be corrected. The need for this correction can be reduced by making the membrane as thin as possible. Some membrane, which are designed for high pressures, contain buttons that pass through the membrane which measure the displacement of the soil directly, removing the need for this correction. These buttons are, however, a point of weakness and are more susceptible to a rupture of the membrane. It is assumed that the test section expands as a right circular cylinder. However, the test section of the PM has a finite length and in practice only the middle third of is cylindrical since the ends are restrained. Volume displacement

types usually contain flexible guard cells which are inflated with the middle measuring cell to ensure the measuring cell retains its shape. This is known as a tricell probe. Radial displacement probes only have one expanding section and is called a monocell probe. The test section of a monocell probes is usually longer than the measuring cell of a tricell probe but the overall length of the expanding section is similar (Cambridge Insitu, 2018).

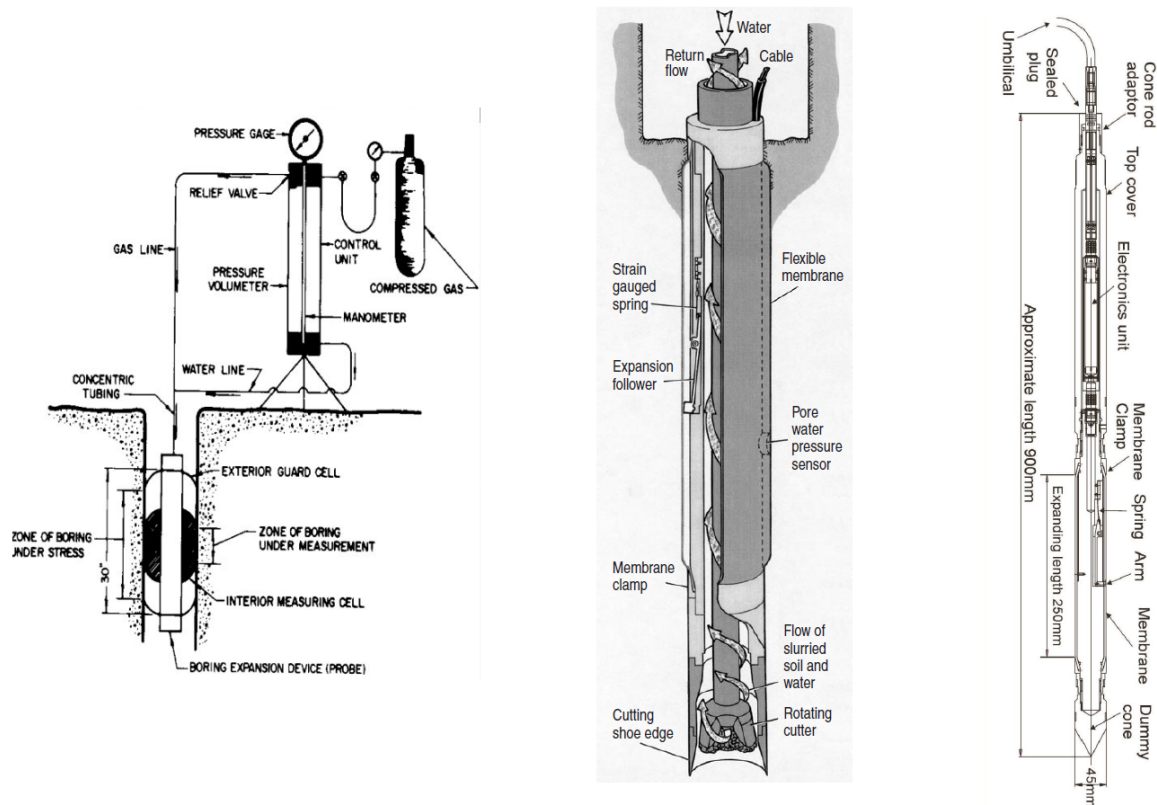


**Figure 2.2:** Schematics of PBP (Ali et al., 2016), SBP (Cambridge Insitu, 2018) & CPM (Cambridge Insitu, 2019)

### 2.2.2.1 Prebored Pressuremeter

The prebored pressuremeter (PBP) is designed to be lowered into prebored hole. The PBP were first developed in France and Japan. An example of a PBP is the Menard pressuremeter. This is a volume displacement systems as described above. The Menard pressuremeter was developed in the 1950's by the Centre d'Etudes Menard and has since evolved as a part of a standard procedure to give design parameters directly referred to as the Menard method. It is based on using the theory of cavity expansion to determine the parameters from PBP test. The procedure is developed specifically for this type of pressuremeter. Another examples of a PBP is the Oyometer, developed by the OYO Corporation in Japan, and the high-pressure dilatometer, developed by Hughes and Ervin in 1980 (Clarke, 2014).

### 2.2.2.2 Self-bored Pressuremeter

The installation process of the PBP disturbs the soil and changes the soil response. It is therefore not possible to obtain a true stress-strain response using a PBP. Regardless of the pressuremeter type, the stiffness of the ground can be obtained from an unload-reload cycle provided that the pocket has been expanded to test undisturbed ground. This is not the in situ ground response. In order to best measure the in situ soil response, the self-boring pressuremeter (SBP) was developed to minimize the

soil disturbance due to the installation. The principle of SBP is based on the balance between two extreme cases. On the one hand inserting an extremely thin walled tube in the ground and removing the soil as the tube advances. This reduces the total vertical stress at the base of the tube to zero. This will result in vertical straining of the soil in front of tube which is accompanied by horizontal straining and thus a reduction in horizontal stress. On the other hand consider pushing a solid rod into the soil. This will lead to an increase in the total vertical stress leading to compression in front of the tube. This results in an increase of the horizontal stress. There must be some point in between this two extremes where there is no change in the stress state in front of the probe. The resulting disturbance is often small enough to lie within the elastic range of the material and is therefore recoverable. The SBP is therefore the only technique with the potential to determine directly the insitu lateral stress,  $\sigma_{ho}$ .  $\sigma_{ho}$  is the major source of uncertainty when calculation the coefficient of earth pressure at rest,  $K_0$ . However the other methods allow the confining stress to be inferred. Examples of SBP are the pressiometre autoforeur, developed by Jezequel et al. (1968) and the Cambridge self-boring pressuremeter, developed at the Cambridge University, UK, in 1971.

### 2.2.2.3 Pushed-in Pressuremeter

Pushed-in pressuremeters can be divided in two groups. The full displacement pressuremeters or cone pressuremeter (CPM) which completely displace the soil during installation. The required jacking forces are a function of the cone resistance and sleeve friction and can therefore be used in the same soil as a static penetrometer, like a cone penetration test (CPT), depending on the reaction system. The CPT is a well established method for making detailed soil profiles from the soils properties. A reasonably reliable classification of the soils can be made by using the cone resistance, sleeve friction and, if a piezocone is used, pore pressure measurements. Absolute values of cone resistance can be used to estimate strength parameters in either sands or clays (Houlsby & Withers, 1988). A downside of a CPT is that it gives a poor indication of the soil stiffness. A pressuremeter can, however, give reliable results when measuring the soil stiffness and strength parameters of the soil.

Most research focused on the self-boring pressuremeter as these are assumed to result in minimal disturbance of the soil during installation. This is unfortunately difficult to achieve in practice. Even if the SBP may result in the highest quality pressuremeter results, the CPM allows for a repeatable amount of ground disturbance prior to the pressuremeter test. This will result in repeatable results from several CPM tests. The initial installation of the full-displacement pressuremeter is modelled theoretically as the expansion of a cylindrical cavity within the soil. The expansion phase of the pressuremeter test can be modelled as a continued expansion of the same cylindrical cavity and the contraction phase as a cylindrical contraction. The modelling of the installation will be somewhat in error, as the penetration of a rod tipped by a 60° cone involves different stress paths from the cavity expansion (Houlsby & Withers, 1988). Baligh (1986a,b) developed the strain path method for soil elements, and this method has been implemented for the analysis of the 60° cone by Teh & Houlsby (1991). It has been shown that the stress distribution far behind the cone tip is similar to the distribution created by the expansion of a cylindrical cavity from zero initial radius. It is believed that if the bottom of the pressuremeter module is located at more than 10D behind the cone tip, it is possible to use the simpler cylindrical cavity expansion theory.

Engineers using the CPT as their standard in situ test, which is the case in the Netherlands, realised the potential of the pressuremeter test since it can provide the engineers with valuable geotechnical information. However, the delicate and fragile nature of the equipment, frequently cumbersome execution of the test using PBP or SBP techniques and the subsequent high costs caused for a lot of hesitation towards using the pressuremeter test. To overcome this, Fugro developed a new CPM with no downhole moving parts. As a part of the modular CPT system of Fugro, the CPM is able to fit on any standard 15 cm<sup>2</sup> penetrometer. This allows for the pressuremeter test to be performed during interruptions of the CPT process. This results in the operational benefits of the CPT test and its efficiency to be applied to the pressuremeter test. The CPM was originally developed for the offshore industry but more recent versions are designed for onshore use with cone trucks. Partial displacement pressuremeters, eg. the Stressprobe, are modified versions of PBPs and SBPs (Zuidberg & Post, 1995).

### 2.2.3 Analytical Solution

Once the pressuremeter is in the ground, a cylindrical cavity is loaded by applying increments of pressure to the inside of the membrane forcing it to press against the material. By analyzing the cylindrical cavity expansion and contraction by using the theory of cavity expansion (Baguelin et al., 1978), empiricism can be avoided. The test is usually carried out in a vertical hole so the derived parameters are appropriate to the horizontal plane (Cambridge Insitu, 2018).

In essence, the pressuremeter test is the expansion of an infinitely long cylinder. It can be noted that there are end effects due to the fact that the probe is of finite length and the membrane is restrained at each end. In order to cope with these end effects, fairly long test probes are used and guard cells (tricell test probe) are in place to protect the measurement cell. This makes the end effects as small as possible. This section assumes ideal cylindrical expansion. The expansion of a cylindrical cavity can be analysed rigorously by existing theories which can take even very complex soil properties into account (Baguelin et al., 1978). First, the basic stress-strain-deformation concepts as described by Wierzbicki (2013) are given in the following subsection. Thereafter, the analytical cavity expansion solution by Baguelin et al. (1978) is presented and lastly the expansion curves are discussed.

#### 2.2.3.1 Basic Stress-Strain-Deformation Concept

Engineering strain in 1D is given by:

$$\varepsilon = \frac{l - l_0}{l_0} = \frac{\Delta l}{l_0} \quad (2)$$

In a cylindrical coordinate system  $(r, \theta, z)$ , the components of the displacement vector are  $\{u_r, u_\theta, u_z\}$ . The special case with  $z = 0$  is called the polar coordinate system. The diagonal strain tensor components are  $\{\varepsilon_{rr}, \varepsilon_{\theta\theta}, \varepsilon_{zz}\}$ . The non-diagonal (shear) components of the strain tensor describe the change of angles.

The radial strain occurs solely due to the displacement gradient in the  $r$ -direction.

$$\varepsilon_{rr} = \frac{u_r + \frac{\partial u_r}{\partial r} dr - u_r}{dr} = \frac{\partial u_r}{\partial r} \quad (3)$$

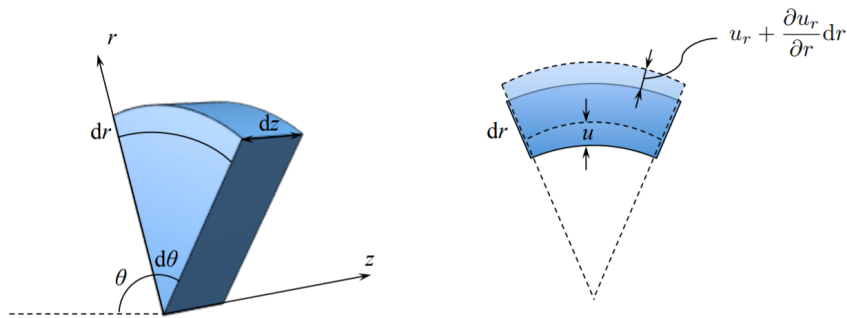


**Figure 2.3:** Change of length in the radial direction (Wierzbicki, 2013)

Circumferential strain,  $\varepsilon_{\theta\theta}$ , has two components. The first component is the strain due to radial displacement and the second is the strain due to the circumferential displacement. These two components are calculated using the following equation:

$$\varepsilon_{\theta\theta}^{(1)} = \frac{(r + u_r)d\theta - rd\theta}{rd\theta} = \frac{u_r}{r} \quad (4a)$$

$$\varepsilon_{\theta\theta}^{(2)} = \frac{u_\theta + \frac{\partial u_\theta}{\partial \theta} d\theta - u_\theta}{r d\theta} = \frac{1}{r} \frac{\partial u_\theta}{\partial \theta} \quad (4b)$$

The total circumferential strain is then given by:

$$\varepsilon_{\theta\theta} = \frac{u_r}{r} + \frac{1}{r} \frac{\partial u_\theta}{\partial \theta} \quad (5)$$

The strain component in the  $z$ -direction is simply given by:

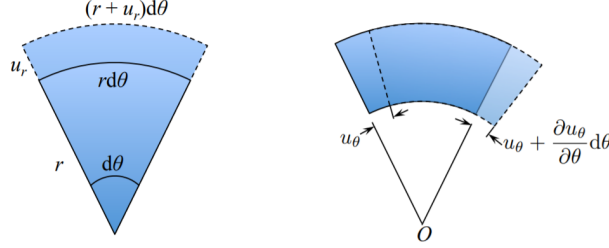


**Figure 2.4:** Two deformation modes responsible for the circumferential strain (Wierzbicki, 2013)

$$\varepsilon_{zz} = \frac{\partial u_z}{\partial z} \quad (6)$$

The shear components are given by the following equations:

$$\varepsilon_{r\theta} = \varepsilon_{\theta r} = \frac{1}{2} \left( \frac{1}{r} \frac{\partial u_r}{\partial \theta} + \frac{\partial u_\theta}{\partial r} - \frac{u_\theta}{r} \right) \quad (7a)$$

$$\varepsilon_{\theta z} = \varepsilon_{z\theta} = \frac{1}{2} \left( \frac{\partial u_z}{r \partial \theta} + \frac{\partial u_\theta}{\partial z} \right) \quad (7b)$$

$$\varepsilon_{zr} = \varepsilon_{rz} = \frac{1}{2} \left( \frac{\partial u_r}{\partial z} + \frac{\partial u_z}{\partial r} \right) \quad (7c)$$

When considering the case of axial (rotational) symmetry, a couple of simplifications can be made. In this case  $u_\theta = 0$  and  $\frac{\partial}{\partial \theta}[\ ] = 0$ . Resulting in the following strain tensor

$$\varepsilon_{rr} = \frac{\partial u_r}{\partial r} \quad (8a)$$

$$\varepsilon_{\theta\theta} = \frac{u_r}{r} \quad (8b)$$

$$\varepsilon_{zz} = \frac{\partial u_z}{\partial z} \quad (8c)$$

$$\varepsilon_{r\theta} = 0 \quad (8d)$$

$$\varepsilon_{\theta z} = 0 \quad (8e)$$

$$\varepsilon_{zr} = \frac{1}{2} \left( \frac{\partial u_r}{\partial z} + \frac{\partial u_z}{\partial r} \right) \quad (8f)$$

Consider a cylindrical cavity of infinite length in a limitless mass, the soil, which is weightless, isotropic and homogeneous. The axis of the cavity is vertical and denotes the direction  $Oz$ . Initially, a pressure  $p_0$  exists in the cavity, while throughout the mass there is a uniform horizontal stress equal to  $p_0$  and a uniform vertical stress,  $\sigma_{v0}$ .

A pressure increase,  $\Delta p$ , to a higher pressure,  $p = p_0 + \Delta p$ , causes an expansion of the cavity and only radial movement in the mass such that a particle located initially at a radial distance  $r_0$  will find itself in the deformed state at a distance  $\varrho = r_0 + u$ , where  $u$  is the distance the particle moved. All movement takes place in the horizontal plane, plane strain, therefore only this plane needs to be considered in the analysis. A short linear element with length  $dr$ , which lies in a radial direction will undergo contraction without rotation, and a short linear element of length  $r d\theta$  will elongate and will remain perpendicular to  $dr$ . The circumferential strain at the wall,  $\varepsilon_o$ , can be described by  $\varepsilon_o = \frac{u_o}{r_o}$ . Using this element we can describe the distortion  $\Gamma$  and the change in volume  $\mu$ . The sides of the deformed rectangle is given by:

$$d\zeta = (1 + \varepsilon_{rr})dr \quad (9a)$$

$$\zeta d\theta = (1 + \varepsilon_{\theta\theta})dr \quad (9b)$$

Considering the assumption that the strain are small, meaning that second or higher order terms can be neglected,  $\Gamma$  and  $\mu$  are given by:

$$\Gamma = \varepsilon_{\theta\theta} - \varepsilon_{rr} \quad (10)$$

$$\mu = \varepsilon_{\theta\theta} + \varepsilon_{rr} \quad (11)$$

When the deformations are large, so called Green strains,  $g$ , can be used to account for the second order strains. Green strains are defined by:

$$g = \frac{1}{2} \frac{dl^2 - dl_0^2}{dl_0^2} \quad (12)$$

They are related to  $\varepsilon$  by:

$$(1 + \varepsilon)^2 = 1 + 2g \quad (13)$$

Prapaharan & Thevanayagam (1989) stated that a plane strain, cylindrical cavity expansion problem must satisfy three constraints: (1) Strain compatibility; (2) equilibrium of stresses; and (3) constitutive behavior of the material in terms of effective stresses. These three constraints implicate that the magnitude and distribution of the effective stresses during the cavity expansion are independent of the specimen size. However, the total stresses and the pore pressure distribution are affected by the boundary condition imposed on the external wall, especially at large strains as schematically shown in Fig 2.5

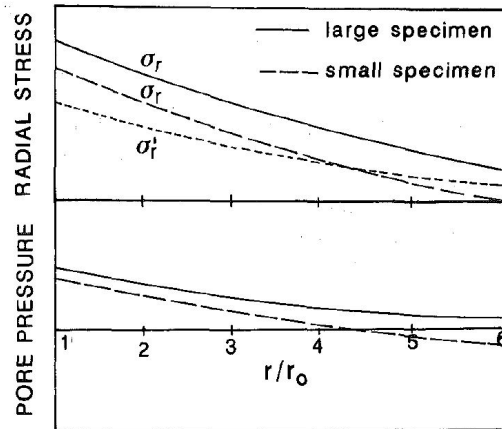
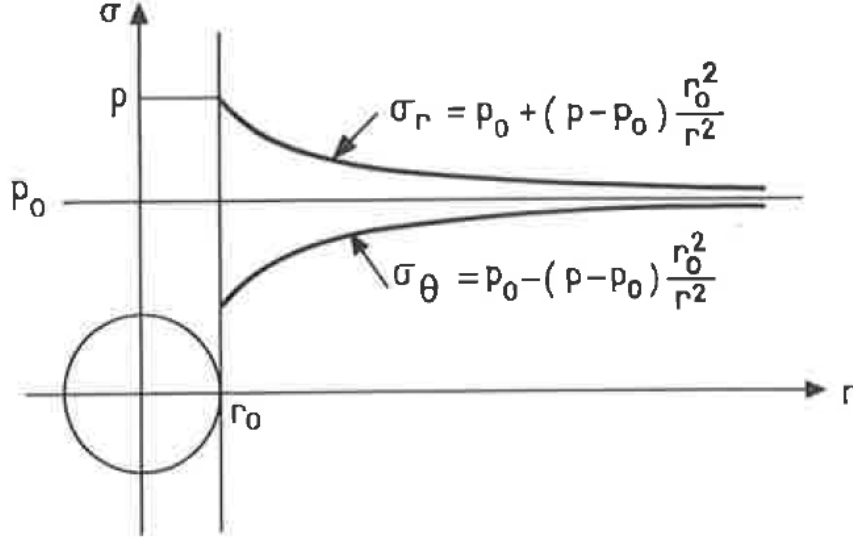


Figure 2.5: Prapaharan & Thevanayagam (1989)

### 2.2.3.2 Cavity Expansion Theory

Baguelin et al. (1978) provides an analytical solution for the stress field of an elastic-plastic soil. In this solution the domain is divided in an elastic zone and a plastic zone. In the elastic zone, the stress increments and strains decrease with the square of the distance, i.e.  $\Delta\sigma$  and  $\epsilon$  vary with  $1/r^2$ . Since  $\Delta\sigma_r = -\Delta\sigma_\theta = G \frac{\epsilon_0 \cdot r_0^2}{r^2}$ , the curves of  $\Delta\sigma_r$  and  $\sigma_\theta$  are symmetrical around the initial pressure  $p_0$ . The stress state for a purely elastic soil is shown in Figure 2.6. When a specific value for the deviatoric



**Figure 2.6:** Stress field for purely elastic soil (Baguelin et al., 1978)

stress is reached, the soil yields and become plastic. Baguelin et al. (1978) considered two cases: (1) a purely cohesive soil which behaves according to the Tresca failure criterion and (2) a both cohesive and frictional soil which behaves according to the Mohr-Coulomb failure criteria. Given that the focus in this research lies on a sand soil, only the second case is elaborated. The Mohr-Coulomb failure criterion is given in Equation 14

$$\sigma_\theta + c \cdot \cot\phi' = K_a(\sigma_r + c \cdot \cot\phi') \quad (14)$$

Where:

$$K_a = \tan^2\left(\frac{\pi}{4} - \frac{\phi'}{2}\right) \quad (15)$$

The soil will enter the plastic phase when  $\sigma_r = P_F$ , which occurs first at the wall of the cavity.  $P_F$  is the stress at failure and can be calculated with:

$$P_F = p_0 + (p_0 + c \cdot \cot\phi') \cdot \sin\phi' = p_0(1 + \sin\phi') + c \cdot \cot\phi' \quad (16)$$

In order to solve the stress field, an equilibrium equation is used. This equilibrium equation is given by:

$$\frac{d\sigma_r}{d\rho} + \frac{\sigma_r - \sigma_\theta}{\rho} = 0 \quad (17)$$

By combining Equations 14 and 17 the variation of  $\sigma_r$  and subsequently  $\sigma_\theta$  can be written as a function of the radial distance,  $\rho$ :

$$\sigma_r + c \cdot \cot\phi' = (P_F + c \cdot \cot\phi') \cdot \frac{\rho^2}{\rho_0^2}^{\frac{1-K_a}{2}} \quad (18)$$

and

$$\sigma_\theta = K_a \cdot (\sigma_r + c \cdot \cot\phi') - c \cdot \cot\phi' \quad (19)$$

Figure 2.7 shows the stress field for an elastic plastic soil assuming that a cavity of initial zero radius has been expanded to a radius  $\rho_0 = a$ . In the elastic zone ( $\rho > \rho_F$ ), the coordinates  $r$  and  $\rho$  are interchangeable, and the values of  $\sigma_r$  and  $\sigma_\theta$  can be calculated from their known value at  $\rho_F$ . With this solution, it is possible to calculate the theoretical plastic radius,  $\rho_F$ , using either  $\sigma_r$  or  $\sigma_\theta$  as a reference.

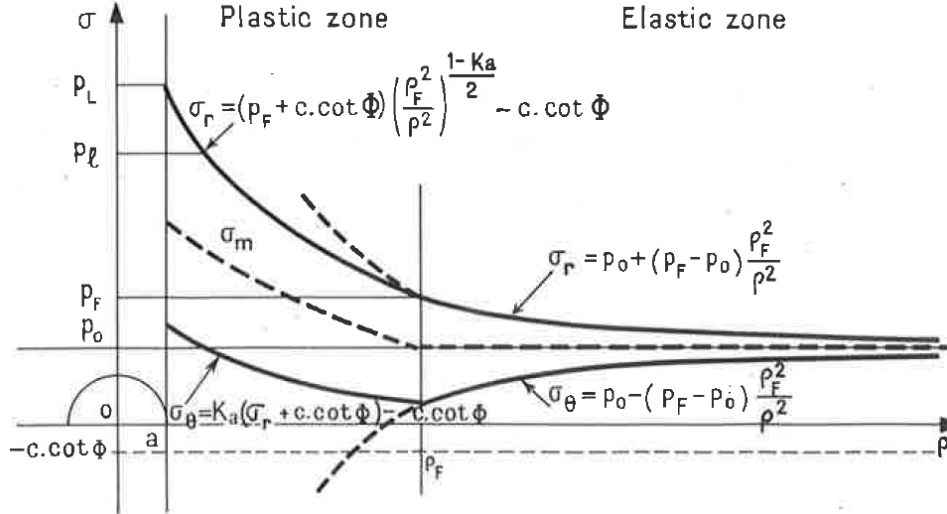


Figure 2.7: Stress field for an elastic plastic soil (Baguelin et al., 1978)

### 2.2.3.3 The Expansion Curve

In a cone pressuremeter test, the membrane is expanded against the soil and measurements are taken of the applied pressure and displacement of the membrane. The in-situ stress state, deformation and strength parameters can be derived using this curve. The interpretation of the test and the parameters derived from the test are dependent on the ground conditions, the type of instrument, method of installation, type of test and the method of interpretation. Each of the three type of pressuremeters produce three distinct types of expansion curves shown in Figure 2.8.

A pre-bored pressuremeter (PBP) test produces a S-shaped curve. The first part, OA, is the expansion of the membrane within the mud-filled borehole. The second part, AB, is the deformation of a zone softened during drilling. The third part, BC is a measure of the elastic behaviour. Point C marks the start of yielding of the ground adjacent to the membrane.

A self-boring pressuremeter (SBP) has two parts. Point B is the point where the membrane begins to move. This point is equal to the total horizontal stress. Point C is the yielding point. For a pushed-in pressuremeter (PIP), there are also two parts to the curve. Theoretically, during installation an infinite expansion occurs so that there should be very little increase in pressure needed to expand the membrane. This is not the case. As the probe is pushed into the soil the soil is unloaded as it flows past the shoulder of the cone of a full displacement pressuremeter. Thus point C, represents a yield point. A PIP that partially displaces the soil gives an expansion curve between that of a SBP and a full displacement pressuremeter (Clarke, 2014).

The pressuremeter test gives data in terms of the total radial stress and radial displacements of the cavity wall. The displacements are directly related to the hoop strain. However in order to solve the boundary problem represented by a cavity expansion the radial strain and circumferential stress must also be known. If it is assumed that the test is undrained (as is often the case for clays) then the loading takes place without generating volumetric strains. This means that radial and shear strains can be easily derived from circumferential (hoop) strains. If the expansion is drained then a more

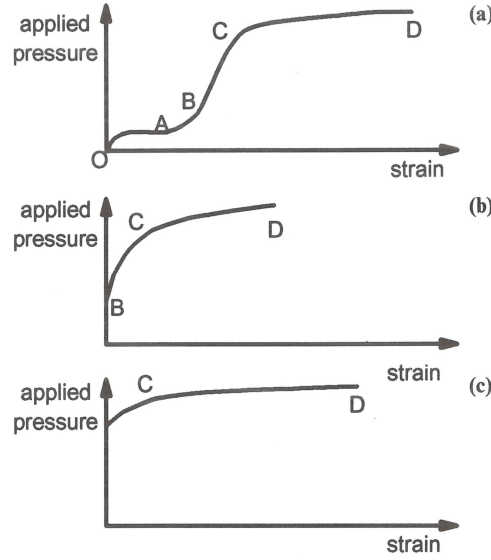


**Figure 2.8:** Different types of expansion curves. (a) PBP, (b) SBP & (c) PIP (Clarke, 2014)

complex solution is required and shear and volumetric strains are derived using assumptions about the dilatant behaviour of the material (Cambridge Insitu, 2019).

From the type of graphs shown in Figure 2.8, at least three different shear moduli can be calculated in practice: The initial tangent modulus  $G_i$ , the unload-reload modulus  $G_{ur}$  and the reload-unload modulus  $G_{ru}$ . In the interpretation of the shear modulus measured by pressuremeter tests, it is assumed that the pressuremeter is a long cylindrical cavity expanding radially under plane strain conditions in the axial direction. Using this assumption, the expansion curve can be solved directly using mathematical expression for the loading of a cylindrical cavity. If a pressuremeter is expanded in a linear isotropic elastic material the relation of the change in cavity effective stress,  $p$ , which is the same as the applied pressure and the change in cavity hoop strain  $\varepsilon_o$  is well known, so that the shear modulus  $G$  can be calculated from the slope of the pressure-expansion curve:

$$2G = \frac{dp}{d\varepsilon} \quad (20)$$

This is only justified when true strains are used (Whittle, 1995). True strains are defined as the sum of each incremental increase in radius divided by the current radius.

$$\varepsilon_t = \ln(r_i/r_o) \quad (21)$$

Where  $r_i$  is the current radius of the cavity and  $r_o$  is the original radius of the cavity. Plotting true strain rather than simple strain makes it easier to compare modulus parameters taken from rebound cycles at different cavity strains, and makes it easier to compare rebound cycles between instruments which strain the soil to different magnitudes.

In order to measure the elastic shear modulus, small unload-reload loops can be performed during the test. This approach implies that any unloading of the expanding cavity brings the stress state of the surrounding soil to a point below the currently expanded yield surface, into a zone where strains are small and to a large extent reversible. It is important that the elastic limit of the soil is not exceeded during the unloading phase. Wroth (1982) suggested that the magnitude of the change in cavity effective stress during elastic unloading should not exceed

$$\Delta p = \frac{2\sin\psi}{1 + \sin\psi} p_c \quad (22)$$

With  $p_c$  is the cavity effective stress at which unloading starts. There is, however, the problem of how to apply the measured shear modulus to engineering design, as the modulus is known to vary with both stress level and strain amplitude.

The interpretation of the test results differ for both drained and undrained test conditions. CPM tests are analysed as either drained or undrained cavity expansions. For an undrained cavity contraction there is the closed form solution of Houlsby & Withers (1988). The analysis assumes a simple elastic/perfectly plastic shear stress/shear strain response and can give realistic estimates of the undrained shear strength. If the loading phase has been carried out to a great enough expansion, the limit pressure can be determined directly. The analysis done by Withers et al. (1989) can be applied to a drained cavity contraction in a purely frictional material. For this analysis a simple elastic/perfectly plastic shear stress/shear strain response is assumed. This implies that contraction will occur at a peak friction angle, a behaviour which tends to apply over a relatively short strain range. Hence the analysis often gives implausible results. In order to apply the drained solutions, an assessment of the constant volume or critical state friction is required as well as knowing the pore water pressure. Neither parameters is measured directly by the CPM, although use of a piezo-cone at the front end can help with water pressure. It might also be possible that due to the severe stressing of the material prior to the expansion test by means of pushing in the CPM has resulted in a crushed zone in material close to the pressuremeter. This might influence the estimates of the peak friction angle. (Cambridge Insitu, 2019)

The analysis of the cavity expansion test in material that has been subjected to high levels of disturbance prior to the placing of the pressuremeter is complex. For tests where no material is removed (i.e. CPM), the ground has undergone something approximating a cavity expansion to a limit pressure condition as a consequence of the CPT push. There is a partial relaxation of the soil as it flows past the base of the cone and unloading occurs if the cone is removed from the ground prior to placing the pressuremeter. This disturbance is irrecoverable. Once the pressuremeter is in position, at no point in the test is the outer surface of the probe in contact with undisturbed material, and up until a certain distance from the pressuremeter the soil is in a purely plastic state. The primary purpose of the expansion phase of the CPM test is to ensure this is the case by taking the material to a higher level of strain and stress that is that previously experienced and thus erasing the stress history of the installation process. Ideally the limit pressure is re-established. Afterwards, as the material is unloaded and reloaded during the test, the stresses and strains determined by the pressuremeter will be a function of the undisturbed material, at some distance from the probe, acting at the elastic-plastic transition. This allows for the measurement of realistic values for the elastic properties of the undisturbed material in its in-situ state (Cambridge Insitu, 2019). It must be noted that although unload/reload cycles give consistent descriptions of stiffness degradation with strain, the stiffness modulus is also stress dependent. Given that a drained CPM test tends to be conducted at significantly higher levels of effective stress than the in-situ state, the modulus values may be magnified.

#### 2.2.4 Installation Effects

White & Bolton (2004) conducted a series of plane-strain calibration chamber tests in order to quantify the penetration mechanisms around a pile tip, as well as the response of the interface layer adjacent to the shaft during further penetration. The measured strain paths are similar to predictions made by the strain path method, and contrast sharply with assumptions implicit in cavity expansion solutions. It was found that an interface zone exists adjacent to the pile shaft. This zone is comprised of fine broken soil particles which were observed to contract while shearing along the pile-soil interface. This mechanism could explain the degradation of shaft friction with increased pile penetration as well as a recovery of capacity over time.

The compressive strains induced by the cone tip entering the soil could be partly balanced by dilation as the soil moves along the cone tip and shears around the shoulder of the tip into the interface zone, which is at a lower stress level. However, some mechanical phenomena might influence the behaviour of the soil. One example is the possibility of particle breakage. Particle breakage would change the range of attainable void ratios but this is difficult to model.

Research by Prapaharan et al. (1990) has shown that the disturbance reduces the peak strength and increases the failure strain for brittle soils. For ductile soils, the stress-strain curve for the disturbed

soil lies under that for undisturbed soils. In addition, the tangent modulus is reduced considerably for both types of soils regardless of the sensitivity.

The installation of a cone pressuremeter into the soil influences the pressure-expansion curve. Given that the determination of the stress-strain curve follows from the differentiation of the pressure-expansion curve, it makes sense that the installation effects also influence the stress-strain curves. The determination of the stress-strain curve is based on the assumption that the soil was undisturbed during the installation phase. This would mean that the initial radial pressure,  $p_0$ , needed to expand the pressuremeter membrane is equal to the in situ total horizontal pressure,  $\sigma_{h0}$ , when the radial strain,  $\varepsilon_0$  is zero. This assumption is inherently false since it is impossible not to disturb the soil when installing the pressuremeter. The fact that this initial disturbance is impossible to measure is the reason why the first loading part of the pressuremeter test is mostly disregarded by engineers as no accurate parameters can be determined from this part of the test. Silvestri (2004) describes two types of installation effects: (1) Overpushing, where the soil is pushed outwards and loading occurs. In this case the initial outward radial strain  $\varepsilon_{0,i} > 0$ . (2) Overcutting, when too much soil is removed during the installation of the PM and the soil unloads. This results in an initial inward radial strain  $\varepsilon_{0,i} < 0$ . With the installation of a cone pressuremeter, the disturbance is purely overpushing while a Ménard pressure meter is accompanied by purely overcutting disturbance. A self-boring pressuremeter aims to balance these two disturbance types ideally resulting in no soil movement underneath the pressuremeter. These disturbance types are shown in Figure 2.9.

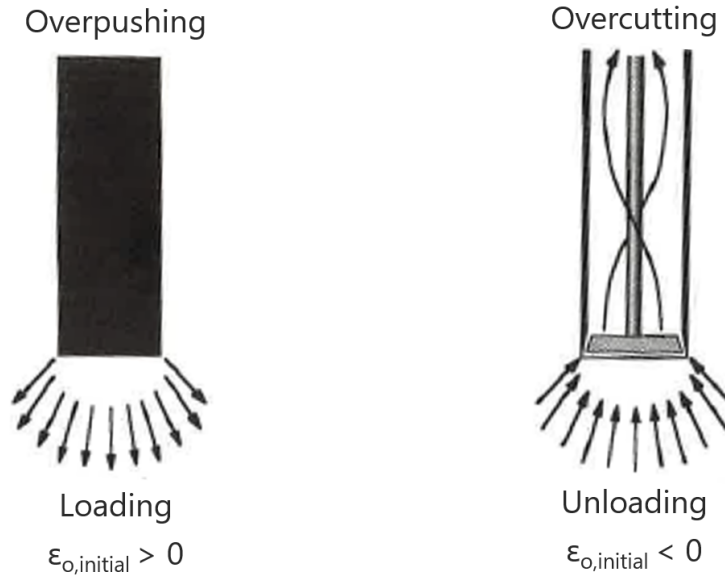


**Figure 2.9:** Different Disturbance Types

Since this research focuses on cone pressuremeters, the overpushing disturbance will be elaborated. When overpushing occurs, the soil is loaded with  $p_a > \sigma_{h0}$ , where  $p_a$  is the “lift-off” pressure and  $\sigma_{h0}$  is the in situ lateral stress. The “lift-off” pressure is the pressure needed to initiate movement of the membrane during a pressuremeter test. In Figure 2.10a the initiation of the expansion process is given by point A. The radial strain at this point is given by disturbance strain  $\varepsilon_{0a}$ . The ideal pressuremeter curve, when no disturbance is present, is given by  $p$  and  $\varepsilon_0$ . From point A, the pressuremeter gives the apparent expansion pressure and radial strain,  $p^*$  and  $\varepsilon_0^*$ . This apparent curve will follow the ideal curve for  $\varepsilon_0^* > \varepsilon_{0a}$  as  $dp^*/d\varepsilon_0^* = dp/d\varepsilon_0$ . As mentioned before in this subsection, the stress-strain curve can be determined from the expansion-strain curve. This is done using the following equation (Silvestri, 2004):

$$\tau = \varepsilon_0 \frac{dp}{d\varepsilon_0} \quad (23)$$

This equation is valid for small radial strains (i.e.  $\varepsilon_0 < 10\% - 15\%$ ). If the disturbance strain is known, it can be implemented in Equation 23 to determine the true stress-strain curve  $\tau(\varepsilon_0)$  or simply  $\tau$  as shown in Equation 24.

$$\tau = (\varepsilon_0^* + \varepsilon_{0a}) \frac{dp}{d\varepsilon_0} \quad (24)$$

If  $\varepsilon_{0a}$  is unknown, which is equivalent to assuming  $\varepsilon_{0a} = 0$ , the differentiation of the pressuremeter curve will lead to an apparent shear stress-strain curve  $\tau^*(\varepsilon_0^*)$  defined by

$$\tau^* = \varepsilon_0^* \frac{dp^*}{d\varepsilon_0^*} \quad (25)$$

Both the apparent and true shear stress-strain curves can be seen in Figure 2.10b. As mentioned before,  $\varepsilon_{0a}$  is impossible to measure in situ. However, it might be possible to estimate this initial disturbance strain using MPM simulations if the input parameters of the model match the properties of the site. This would provide a new method to correct the pressuremeter data gained from a cone pressuremeter test.

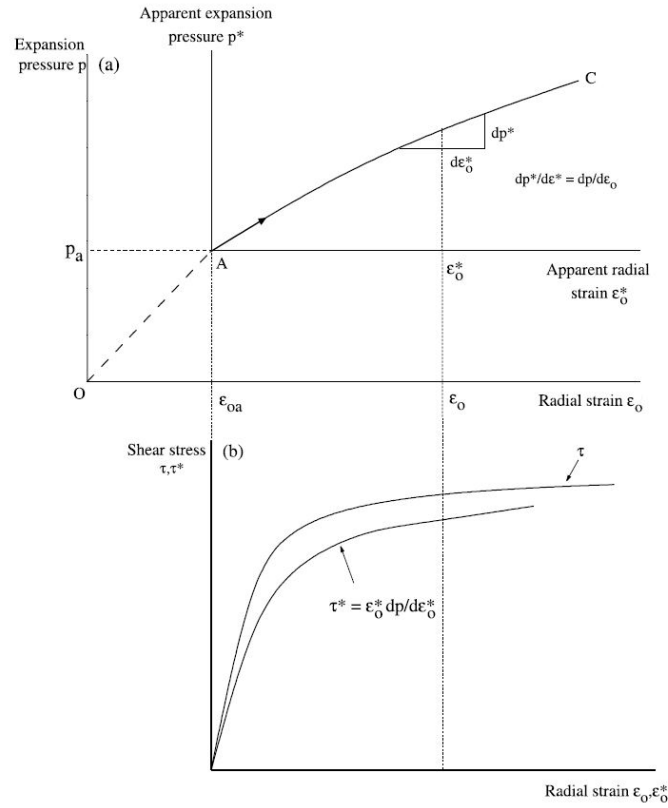


**Figure 2.10:** Overpushing disturbance: (a) pressuremeter curve; (b) apparent and true stress-strain curves (Silvestri, 2004).

Jefferies & Shuttle (1995) also investigated the disturbance effects of a SBP in sand and gave the following equation to correct for this disturbance:

$$\varepsilon_r = \frac{\Delta}{R(1 - \delta)} + \frac{\delta}{1 - \delta} \quad (26)$$

With  $\varepsilon_r$  is the true engineering radial strain,  $\Delta$  is the measured radial displacement increment,  $R$  is the outside radius of the SBP and  $\delta$  is the unknown radial displacement. The problem lies in the fact that  $\delta$  is unknown. In their research the authors aim to correct for the disturbance by using iterative forward modelling (IFM) of the SBP data. A distinction is made between overpushing and overcutting

as mentioned in the beginning of this subsection. For an overcut SBP test the estimated disturbance is (1) well constrained, (2) correcting for the disturbance improves the image match between the data and theory and lastly (3) correcting for disturbance has little effect on the derived ground parameters. For an overpushed SBP test, Jefferies & Shuttle (1995) found that (1) the estimated disturbance is poorly constrained, that (2) correcting for disturbance improves the image match between data and theory, however a wide range of possible fits are available, (3) correcting for disturbance has little effect on the derived ground parameters in terms of  $s_u$  and the rigidity,  $I_r$ , and lastly (4) a wide range of equally good disturbance values means that  $\sigma_{h0}$  is less well constrained. This means that for SBP, it is better to overcut than to overpush given that the correction for overpushing leads to more uncertainty. This further adding to value of finding a new method to correct for the overpushing disturbance.

### 2.2.5 Conclusion

The pressuremeter test has numerous advantages. Firstly, it is an in situ test, thus meeting an important requirement of modern soil investigation methods. The pressuremeter measures deformation properties of the soil in addition to a rupture or limit state, unlike other in situ tests such as vane or penetration tests. This allows the engineer to benefit from the considerable advantage of having deformation information available as a matter of routine. A further advantage is that the pressuremeter results are based on a test which involves a fairly large volume of soil which is not always the case with a CPT. A last advantage is that the pressuremeter test is applicable to most types of soils. This is not the case for other in situ tests like the vane test which cannot be performed in free draining sand or gravel (Baguelin et al., 1978).

The SBP is the least disruptive method. The CPM does, however, allow for the most repeatable amount of disturbance. This would allow for a procedure to be calibrated which incorporates the installation effects. If this can be accomplished, it could lead to a reliable and cost-effective method to better understand the subsurface. The installation effects surrounding the shaft could also be used in future numerical models.

## 2.3 Numerical Methods

### 2.3.1 Introduction

In the past decades a new field of geomechanics has emerged: computational geomechanics. In computational geomechanics, numerical methods are used to compute the most probable outcome of a given engineering problem. Using engineering judgement, a prediction can be made based on a series of choices and idealisations. In the recent years great progress has been achieved in this field but limited computational capacity and deficiencies in data and knowledge are still major issues (Fern et al., 2019). The goal of numerical modelling in geotechnical engineering is to: (1) Identify possible failure mechanisms, (2) Calculate displacements under loading conditions, (3) Calculate internal forces necessary for the structural design and (4) to understand the behaviour of geotechnical structures. In order to achieve these goals, Schweiger (2017) states that appropriate geotechnical models are needed alongside a good understanding of soil mechanics. It is also necessary to understand what the used software and in particular the constitutive model does which is applied and lastly a clear picture is needed of what is and what is not possible using the numerical model.

In conventional geotechnical engineering, when analysing an engineering problem, an analysis on the serviceability (limit state) using, for example, design charts with stiffness as an input parameter can be carried out. Afterwards, the ultimate limit state is assessed using a separate analysis. This analysis generally uses a different model (e.g. slice method for slope stability problems). In these analysis, strength parameters like cohesion, friction angle, etc. are used as an input. These two models and input parameters do not interact with each other and are two separate analysis which means that the material behaviour and geometry have to be simplified in order to make the analysis feasible. Decades of experience is present in the field of geotechnical engineering using this approach but for complex soil/structure interaction problems, this approach is not sufficient.

Using computational geomechanics, advanced constitutive models can be used to also work out deformations and displacements under load conditions for the serviceability analysis. Instead of using another model to assess the ultimate limit state, the same model can be used to find the failure load and mechanism. This is the major advantage of the computational geomechanics approach. The strength parameters will also influence the serviceability and the stiffness will to some extent, depending on the model, also influence the ultimate limit state. Another possibility of using this approach is that post failure behaviour can also be modelled. However, parameter determination and numerical difficulties can be an issue.

### 2.3.2 Spatial Discretization

Numerical models have the advantage to have low costs, high safety and efficiency in solving various kinds of challenging problems. Based on the description of deformation and motion, existing spatial discretization methods can be classified into Lagrangian, Eulerian and or a combination of both.

In Lagrangian methods, the computational grid is embedded and deformed with the material. The Lagrangian description is where the method follows an element in space and observes the state of this element as it travels through the space. It can be visualized as sitting on a boat as it travels through a river. Since there is no advection between the grid and material, no advection term that describes the mass flow across element boundaries appears in the governing equations. This significantly simplifies the solution process. The mass of each material element is kept constant during the solution process, but the element volume varies due to element deformation. Lagrangian methods have the following advantages (Zhang et al., 2017):

1. They are conceptually more simple and efficient than Eulerian methods. Because there is no advection term, the conservation equations for mass, momentum and energy are simple in form, and can be efficiently solved.
2. Element boundaries coincide with the material interfaces during the solution process so that it is easy to impose boundary conditions and to track material interfaces.

3. Since Lagrangian methods track the flow of individual masses, it is easy to implement history-dependent constitutive models.

A downside of a Lagrangian grid is that it can be subjected to severe element distortion due to large deformations. This can lead to significant errors in numerical solution, and could even lead to a negative element volume or area. This would cause the computation to be terminated. In order to obtain a stable solution with an explicit time integration scheme, the time step must be smaller than the critical time in the grid. In a Finite Element Method, the CFL condition (Courant et al., 1967) gives that the critical time step for the system is given by Equation 27.

$$\Delta t_{cr} = \min_e \frac{l^e}{c} \quad (27)$$

Where  $l^e$  is the characteristic length of element  $e$  and  $c$  is the adiabatic sound speed. Because severe element distortion would significantly decrease the characteristic element length, the time step in a Lagrangian calculation could become smaller and smaller, and finally approach zero, which makes the computation impossible to be completed. To complete a Lagrangian computation for an extreme loading case, a distorted grid must be remeshed and its results must be interpolated to the remeshed grid. The remesh or rezone technique has been successfully used in solving many 1D and 2D problems, but rezoning a complicated 3D material domain is still a challenging task. For a history-dependent material, the history variables are also required to be interpolated from the old grid to the new grid, which may further cause numerical errors in the stress calculation (Zhang et al., 2017).

For problems in which a material domain could become heavily distorted or different materials are mixed, an Eulerian method is more appropriate. In Eulerian methods, the computational grid is fixed in space such that the material flows through the grid. The solution is given at specific points in space and the state of the elements is observed as they travel through these points in space. The Eulerian description can be thought of as sitting on a bench in front of a river and looking at a fixed point while observing the river as it passed through this point. There is no element distortion in Eulerian methods, but the physical variables, such as mass, momentum, and energy, advect between adjacent elements across their interface. The volume of each element is constant during the computation, but its density varies due to the advection of mass. Eulerian methods are suited for modelling large deformations of materials. Eulerian methods only calculate the material quantities advected between elements without explicitly and accurately determining the position of material interface and free surface so that there are some difficulties in following deforming material interfaces and moving boundaries.

### 2.3.3 Small-Medium Deformation Models: Finite Element Method

The Finite Element Method (FEM) is a widely used calculation method in engineering practice. FEM utilises spatial and temporal discretisation to solve differential equations governing mechanical deformation, heat transfer, fluid flow and many other phenomena. The spacial discretisation is done by dividing the problem domain into a number of subdomains called the finite elements. All these finite elements together make up the mesh. A relationship is established between the local (element) and the global space using shape functions. The governing differential equations are then integrated over the problem domain with the application of boundary conditions. The solution is evaluated at integration points which are fixed locations in the local reference frame of each element and then translated onto the nodes via the shape functions. From there, the solution may be approximated for any point within the domain in the same way (Pantev, 2016).

Using the Updated Lagrangian Formulation, the governing equations which need to be solved for are:

- Mass conservation
- Momentum conservation
- Energy conservation
- Measurement of deformation, which relates strains with displacements
- Constitutive equation, which describes the material behaviour

The constitutive equation relates the stress (rate) to the strain (rate) and any other relevant variable. Typically, stress is thought of as being associated with a point in the material, which is the case in the Lagrangian formulation and the motivation for using this in the Finite Element Method. In contrast, a constitutive relation in Eulerian coordinates introduce convective terms in the stress formulation of a history dependent material. While FEM is perfectly suitable for problem which include small to medium deformations, one of the downsides of the FEM is the fact that it can not quite handle large deformations. When large deformations are encountered in a FEM simulation, the mesh can become heavily distorted resulting in numerical inaccuracies and even instabilities. Methods exist to counteract this phenomena by means of remeshing techniques but these introduce inaccuracies given that values need to be interpolated to form the updated mesh. Moreover, if the mesh needs to be updated for every timestep, the simulation become extremely time consuming. An alternative numerical method which is capable of dealing with large deformations is the material point method (MPM). In MPM, individual material points (MPs) are tracked throughout the simulation and the mesh can be reset after each time step. The MPM code is further elaborated in the next subsection.

### 2.3.4 Large Deformation Models: Material Point Method

The material point method (MPM) was initially developed by Harlow (1962). It is based on the so called Particle-In-Cell method (PIC) which was based on the representation of fluid flow by a set of material points moving through a background fixed mesh. Later, Sulsky et al. (1994) extended the approach for modelling problems of solid mechanics, where the equation of dynamic momentum balance is discretized.

MPM is considered as a hybrid method between the particle based methods and the Finite Element Method (FEM). This is because it discretizes the continuum in two different frames. First, the continuum is divided into a set of material points (MPs). Each material point represents a portion of the domain and the mass of this sub-domain is assumed to be constant during all calculations in order to ensure the conservation of mass. In the classical MPM, the mass is considered to be concentrated at the corresponding material point. Other quantities such as velocities, strains and stresses are also initialized at and carried by the MPs. Each material point moves with the deformations of the body and this provides the Lagrangian description of the media.

The second frame is the computational mesh. It is the same as the one used in the conventional FEM and it is built to cover the full domain of the problem. The discrete governing equations are solved at the nodes of the computational mesh. The variables required to solve the equations in the mesh at any step of the analysis are transferred from the MPs to the nodes of the mesh using mapping functions. An example of these mapping functions are the typical linear shape functions used in the FEM. Boundary conditions can be imposed at either the mesh nodes or the material points. The governing equations are solved by using an incremental scheme. After the governing equations are solved, the quantities carried by the material points are updated through the interpolation of the mesh results, using the same mapping functions. The information associated with the mesh is not required for the next step of the analysis. Therefore the mesh can be reset after each time step avoiding any mesh distortion.

The MPM procedure for each time step is shown in Figure 2.11. At the beginning of each time increment, the governing equations are defined by mapping information from the MPs to the computational nodes of the mesh using interpolation functions (a). The governing equations of motion are solved for the primary unknown variables, e.g. the nodal accelerations (b). These nodal values are used to update the acceleration, velocity and position of MPs, as well as to compute strains and stresses at the MPs (c). Since no permanent information is stored in the mesh, it can be freely reset or redefined at the end of each time step (d). The assignment of MPs to finite elements is updated after mesh adjustment.

Large deformation MPM models require defining empty spaces in which the material points are free to move in and these spaces have to be defined in the model and meshed. Deltares has provided the author with a MPM code to use in this research. It is under constant development by a group of dedicated researchers in order to model and simulate large deformation and soil-water-structure

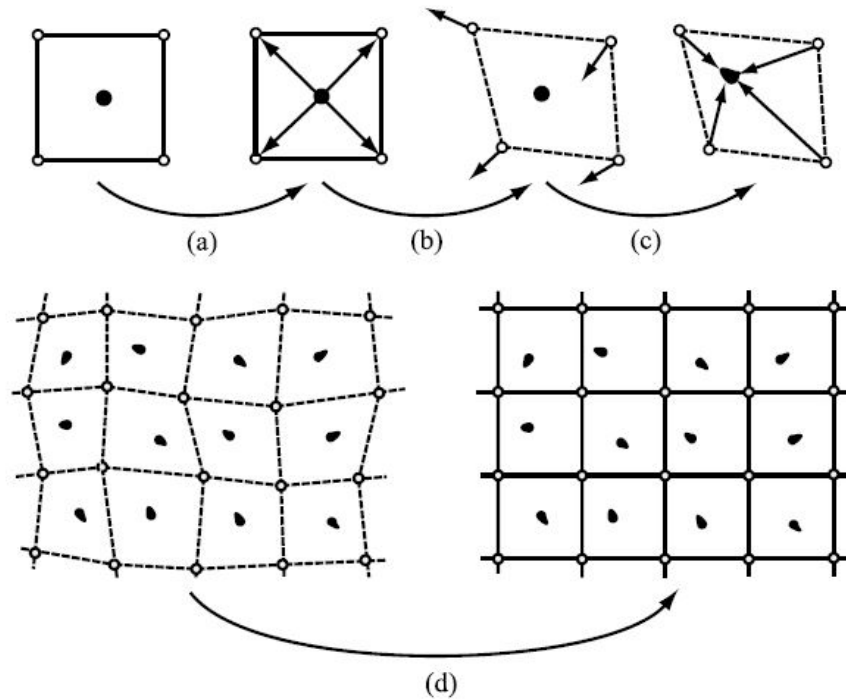


**Figure 2.11:** MPM procedure for one time step (Zhang et al., 2017)

interactions using the material point method. One of the latest additions is the implementation of the 2D-axisymmetric formulation. The following section describes in more detail how this MPM code, and some of its relevant features, works.

#### 2.3.4.1 Mathematical Formulation

The MPM code can be viewed as an extension of the FEM procedure, as it contains several identical schemes like the weak form of the governing equations and the final system of equations posed at the nodes of the computational mesh. The largest difference between the two methods is the calculation of the numerical integration over the volume of a finite element. In FEM, the integration is carried out by using Gaussian quadrature while in MPM they are calculated based on the material points.

From a mathematical point of view, the continuum can be described by a set of differential governing equations. These include the conservation of mass, conservation of momentum, balance of energy and the corresponding boundary conditions. Furthermore, constitutive equations such as the stress-strain relationship, which is characteristic of the material forming the continuum, are needed. Thermal effects are very small and therefore neglected.

#### 2.3.4.2 Impact/Contact Formulation

Soil-structure interaction problems are common in the field of geotechnical engineering. The MPM code is naturally capable of handling non-slip contact between different bodies, since the velocity of both bodies belong to the same vector field, inter-penetration cannot occur. However, when continuum bodies come into contact, mostly frictional sliding occurs at the contact surface. To simulate such a sliding interaction a specific contact algorithm that allows relative motion at the interface between contacting bodies is required. Ceccato et al. (2019) describes the contact algorithm used in the program Anura3D, which is very similar to the code used in this research.

The contact algorithm used in the MPM code has the advantage that it does not require any special interface element between the bodies in contact. It can model interaction between solid bodies as well as shearing in granular materials and has been proven to be an efficient algorithm. The contact

algorithm can be considered as a predictor-corrector scheme. In each timestep, the velocity is predicted for each body separately and then corrected using the velocity of the coupled bodies following the contact law (Ceccato et al., 2019). The contact surface is predefined by the user in the pre-processing phase. For each contact node, the algorithm proceeds with checking if the bodies are approaching or separating. This is done by comparing the normal component of the single body velocity with the normal component of the combined bodies velocities. Apart from the cohesive contact, the adhesive type of contact is well suited to simulate soil-structure interaction in case of cohesive soil in undrained conditions.

#### 2.3.4.3 Moving Mesh

As mentioned in the beginning of Subsection 2.3.4, the background mesh in MPM does not store any permanent information. Thus the mesh can be redefined freely at the end of each time step. This enables the implementation of the so-called moving mesh feature, where the mesh is divided in two parts: One part is defined as the moving mesh which is adjusted to the movement of a reference body after each time step. This body is usually a structure which ensures that the contact surface of the structure coincides with the element boundaries during the entire simulation. The other part of the mesh is defined as the compressing/expanding mesh. This part of the domain compresses (or expands) as the other mesh moves in order to comply with the boundary conditions. For example in a foundation analysis, using this method the mesh area adjacent to the foundation moves with the same average displacement as the structure. The elements in the moving mesh keep the same shape while the elements in the compressing mesh reduce in vertical length. It should be noted that the initial elements sizes in the compression mesh should be defined in such a way that the aspect ratio of the elements stay reasonable throughout the simulation.

The moving mesh feature is especially useful in combination with the contact algorithm and when reaction forces need to be computed. If a body or structure is expected to move during the simulation, it is necessary to keep the element boundaries aligned with the structure. In general, the structure is rigid in contrast to the soil. Using the moving mesh prevents the MPs from the impacting body and the soil to share elements. The moving mesh also preserves the shape of the impacting body. If the reaction forces on a predefined surface, for example the soil-structure interface, are computed, it is necessary that this interface follows the movement of the structure. The reaction forces on a surface are computed as the sum of the nodal reaction forces over the nodes belonging to the selected surface (Ceccato et al., 2019). As a last advantage, fine meshing can be focused along the impacting body, avoiding unnecessary refinement.

#### 2.3.4.4 2D-Axisymmetric Formulation

Several geotechnical problems are axisymmetric. Examples are pile installations, circular shallow foundations or cone penetration tests. These problems were initially modelled as 2D plane strain, as an approximation, or 3D problems. The 3D models are very expensive in terms of computational power. By introducing a 2D axisymmetric formulation, originally developed by Sulsky & Schreyer (1996), in the MPM code, Galavi et al. (2019) enabled a significant reduction in the number of elements and MPs and therefore reducing the required computational effort to simulate these problems. This formulation was validated by successfully simulating a cone penetration test and comparing the results with empirical predictions. This, among other validations, showed that the 2D-axisymmetric formulation can model these types of problems computationally more efficient than a 3D simulation.

#### 2.3.5 Comparison Between FEM and MPM

As mentioned in the previous subsection, the MPM and FEM are similar in terms of mathematical formulation for each time step. There are, however, several differences in both accuracy and efficiency of both methods. Zhang et al. (2017) made a comparison between the two methods based on these aspects. In order to determine which method is most suitable for the problem at hand, these aspects have to be taken into account.

## Basic Formulation

Despite showing a lot of similarities in mathematical formulation, the formulations of both MPM and FEM differs on the following points:

- The FEM employs Gauss quadrature to evaluate the integrals in the weak formulation, while the MPM employs particle quadrature. This results in the constitutive equations being evaluated at Gauss quadrature points in the FEM but at particles in the MPM.
- The computational mesh of a Lagrangian FEM is attached to the material throughout the entire simulation. In contrast, the background grid of the MPM is only attached to the material while solving the governing equations of motion during each time step. At the end of each time step, the position, velocity and acceleration of the MPs is updated and the deformed grid can be discarded to employ a new regular grid in the next time step. As a result, no fixed mesh connectivity is required in the MPM. Because all the material properties are carried by the MPs, the nodal variables must be recalculated in the next time step from the updated MP variables. This means that the mass matrix in the MPM is no longer a constant matrix as that in the FEM meaning that the MPM needs an additional computational step.

## Computational Accuracy and Efficiency

If the element size is similar for both the MPM and the FEM, the difference in terms of accuracy mainly depends on the quadrature scheme and on the technique to deal with large deformations. The Gauss quadrature used by the FEM for the weak form integration is more accurate than the particle quadrature used in the MPM. Furthermore, inaccuracies can arise if MPs cross element boundaries. This can cause numerical instability and the user must try to avoid this from happening. On the other hand, mesh distortion introduce numerical inaccuracies for FEM models. This can be coped with to some extent using remeshing techniques but for large deformation problems it still remains a challenge.

The computational efficiency of a numerical method depends on the computational cost per time step and the time step size. The FEM has only one Gauss point in each element, while the MPM usually employs 1, 4 and 8 particles in each grid cell for 1-, 2- and 3D problems respectively. Stress update and nodal internal force calculation will loop over the Gauss points (FEM) and particles (MPM). It follows that the computational cost of the MPM is much higher than that in the FEM in this regard. Both the explicit MPM and explicit FEM employ the central difference method, whose critical time step size depends on the characteristic element length. In the MPM, the characteristic element length size is constant during the whole solution process due to the fact that the mesh is reset after each time step. In contrast, the characteristic element length in FEM decreases with the element deformation. Because the adiabatic speed of sound in both MPM and FEM are almost the same (Zhang et al., 2017), the time step of the FEM is will become smaller than that of the MPM and subsequently the total number of steps required in the FEM is larger than that in the MPM. For small deformation problems, the characteristic element length in the FEM will not decrease significantly so that the computational efficiency of the FEM is higher than that of the MPM. For large deformation problems, however, the characteristic element length in the FEM decreases rapidly, which results in a significant decrease in the time step size and significant increase in the total number of required time steps.

Concluding the comparison between the FEM and the MPM for geotechnical applications the magnitude of the expected deformation will be the deciding factor. In terms of computational accuracy and efficiency, small deformation problems are best suited for a FEM model while large deformation problems can best be solved using the a MPM model. Since this reseach aim to model the installation of a CPM which is in fact a large deformation problem, using a MPM model is deemed to best method. Like in FEM, a finer grid will be necessary where high gradients of stress and strain are expected.

### 2.3.6 Constitutive Models

In the past years, many constitutive models have been developed, each for specific conditions and making its own assumptions. Therefore, the choice of the constitutive model relies on the engineering

judgment of the modeller as it depends on the type of soil and the problem at hand. It is important to ensure that the chosen model is able to capture the mechanisms of interest given that the choice will have a significant influence on the computational time and the results. A constitutive model plays two fundamental roles in MPM simulations (Ceccato et al., 2019):

- Controls failure at small deformations (Similar to Finite Element simulations)
- Controls the dissipation of energy and therefore dictates the post-failure behaviour

The development of constitutive models, or stress-strain relationships, have been in the light of research ever since the early days of soil mechanics, and there has been many significant changes through time. These constitutive models describe the behaviour of the soil. Some models can describe the different aspects of the soil deformation behaviour better than others and it is important to understand what every model is capable of. The important aspects, as described by Brinkgreve (2018), are:

- Elasticity (reversible deformation)
  - After the removal of the load, no residual deformation is present.
- Plasticity (irreversible deformation)
  - After the removal of the load, residual deformation is present.
- Soil failure (Limit state)
  - Soil cannot take anymore load
  - Failure mechanism
- Groundwater
  - Porewater pressure reduces the effective stress
  - Groundwater flow
  - Undrained behaviour
  - Consolidation
- Stress dependent Stiffness
  - Stiffness increases with increasing isotropic stress
  - Stiffness increases with increasing shear stress or deviatoric stress
- Stress path dependent Stiffness
  - Stiffness in compression is generally higher than in shear
  - Stiffness in unloading is higher than with primary loading
- Strain dependent Stiffness
  - High stiffness with low strains, Low stiffness with large strains
- Compaction and Dilatancy (Irreversible volume decrease/increase)
  - Change in porosity due to shear strain
- Stress state history
  - Limit stress or pre-consolidation stress
  - Stiff behaviour with reloading until limit state
- Anisotropic behaviour
  - Stiffness and strength of peat parallel and perpendicular to the fibres is very different
- Softening (Decrease of strength after irreversible deformation)
  - Breaking of cohesive bonds, decrease in friction after dilatancy

In general, the constitutive models can be categorised in two types: (1) Those developed from failure criteria and (2) those developed from energy consideration. The first type of models to be developed were from the failure criteria. These are empirical formulae which predict the stress state at failure without considering the strain state. Examples of these early models are the Mohr-Coulomb, Von Mises & Tresca models. They were combined with elasticity in order to get a first estimate of the strain state and later further developed to include plastic deformation. These models are often referred to as elastic plastic models. Elastic-plastic models assume that the soil hardens with elastic deformation until a threshold is reached ( $F=0$ ).

The second type of models emerged from the work of Roscoe et al. (1958), who developed a stress-strain framework based on energy dissipation, also known as the Critical State Soil Mechanics framework. These models are often referred to as elasto-plastic models as the hardening phase includes plasticity.

The coupling between the development of stresses and strains is a central tenant of the critical state soil mechanics framework. The Cam-Clay model is a simple elasto-plastic model initially developed for normally consolidated and lightly over consolidated clays. It was the first model to capture the different mechanical behaviours from various stress and strain state conditions. Two versions of the Cam-Clay model exist: Original Cam-Clay (OCC) and Modified Cam-Clay (MCC). Both follow the same modelling principles but are formulated in a different way. The numerical implementation of the MCC model, recently introduced in the Anura3D code, uses an explicit integration scheme known Dorman-Prince method (Ceccato et al., 2019). In this section, the basic principles of soil modelling are first adressed. Followed by a more detailed description of the elastic-plastic models and elasto-plastic models. Lastly some limitations of the different soil models are discussed.

### 2.3.6.1 Basic Principles Soil Modelling

Soil models give the relationship between stresses and strains. Most models are based on grain stresses (Effective stress). If the behaviour of the groundwater is included, it is mostly described separately. Generally the stress-strain relationship is written as:

$$\dot{\sigma}' = \underline{\underline{M}} \dot{\epsilon} \quad (28)$$

The material stiffness matrix  $\underline{\underline{M}}$  contains model parameters and can be a function of stresses, strains or other so called state parameters. One of the simpler stress-strain relationships for isotropic linear elastic behaviour is Hooke's Law. Hooke's Law only uses two model parameter: Young's modulus,  $E$ , which gives the stiffness in axial compression with a constant lateral stress and Poisson's ratio,  $\nu$ , which determines how much the material will laterally deform with respect to the axial compression. In reality the soil will not behave linear elastic. Nevertheless Hooke's Law does form the basis of many soil models.

Many soil models use the principle that strain of strain increments consist of an elastic and a plastic component. The elastic component is described by Hooke's Law and the plastic component is generally described by:

$$\dot{\epsilon}^p = \dot{\lambda} \frac{\partial g}{\partial \sigma'} \quad (29)$$

Where  $\lambda$  is the plastic multiplier which determines the magnitude of the plastic strains and  $g$  is the plastic potential. The plastic potential determines the direction of the plastic strains. The flowrule,  $f$ , is used to determine if plastic strains increments occur. If  $g = f$ , it is called associated plasticity and if  $g \neq f$  it is called non-associated plasticity.

### 2.3.6.2 Elastic-Plastic Models

#### Linear Elastic-Perfectly Plastic: Mohr-Coulomb

The Mohr-Coulomb model is one of the more frequently used soil models. One of the flow rules and its corresponding plastic potential function are given by:

$$f = \frac{1}{2}(\sigma'_3 - \sigma'_1) + \frac{1}{2}(\sigma'_3 + \sigma'_1)\sin\varphi - c \cos\varphi \quad (30)$$

$$g = \frac{1}{2}(\sigma'_3 - \sigma'_1) + \frac{1}{2}(\sigma'_3 + \sigma'_1)\sin\psi - c \cos\psi \quad (31)$$

Where  $\varphi$  is the friction angle,  $c$  is the cohesion and  $\psi$  is the dilatancy angle.  $\psi$  gives the volume change due to the deviatoric strain and is for all soil type smaller than  $\varphi$ . The total Mohr-Coulomb criteria consists of six flowrules and corresponding plastic potentials for all combinations of the two principal stresses. Since the Mohr-Coulomb flowrules, for a given  $\varphi$  and  $c$ , are only dependent on the stress state and not on the plastic strain, the flow contour has a fixed position in the principal stress space meaning that this model uses perfect plasticity.

### 2.3.6.3 Hardening and Softening

When using a hardening or softening model, the flow contour is dependent on the stress history and is therefore a function of the plastic strains. This is achieved by including a state parameter which is coupled to the plastic strains using a hardening (or softening) rule. A change of plastic strain will result in a change of position or size of the flow contour. This state parameter can be a physical quantity which can be changed. Hardening is often used to model non-linear and irreversible ground behaviour in the primary loading phase. There are three different types of hardening: Compaction hardening, friction hardening and kinematic hardening.

Compaction hardening is used to model irreversible volume strains in compaction. The elastic area, which is unbounded in a Mohr-Coulomb model, is limited with a hardening flow contour. This hardening flow contour is called a cap. The position of this cap is determined by the pre-consolidation stress. Compression within this cap is treated as elastic behaviour. When the stress path reached the cap and is loaded even further, plastic strains occur. These plastic strains increase the pre-consolidation stress and thus the location of the cap. This allows for more compression. The cap is moving with the stress path. When the soil is unloaded, the cap stays on its new position and the soil behaviour is elastic again.

Friction hardening is used to model a reduction in stiffness and irreversible deviatoric strains due to a deviatoric load. The mobilised friction angle can be used as a state parameter. This mobilised friction angle increases with plastic deviatoric strains widening the flow contour. When reaching the maximum friction angle according to failure criterion, the deviatoric strain become infinite.

The downside of compaction and friction hardening is that both model isotropic hardening, meaning that the elastic area keeps on growing. When the soil is continuously unloaded and reloaded (cyclic behaviour) without reaching the hardening contour, no plastic strains are developed. In reality cyclic loading will result in irreversible strains. This can be modelled using kinematic hardening. With this type of hardening the complete flow contour moves, resulting in plastic strain. When unloading the soil, the flow contour stays and its place allowing for elastic behaviour. When the other end of the flow contour is reached, it moves in that direction resulting again in plastic strains. When the flow contour is small, cyclic loading will continuously produce plastic strains (hysteresis). Within a small elastic area, the strain are very small resulting in a high stiffness.

Softening is a decrease in strength due to plastic strains. Examples of this is the breaking of cohesive bonds in stiff clays due to shear or the decrease in friction angle when tightly packed sand is sheared and shows dilatant behaviour. Softening lead to a concentration of plasticity in a small area (shear band). Furthermore, softening results to progressive failure due to the fact that the stress state which resulted in softening can be upheld.

### 2.3.6.4 Limitations of Soil Models

Ultimately, soil models will always be an approximation of real soil behaviour. The Mohr-Coulomb model is a first order approximation of the soil behaviour where only one constant value of  $E$  determines the stiffness response of the soil. When the Mohr-Coulomb model is used to model soil layers with a large thickness, the layers should be divided into sub layers with different values for  $E$  or incrementally increase the Young's modulus with depth. The limitations of using elastic-plastic behaviour can be summed up as follows (Baguelin et al., 1978):

- Only compressive volumetric strains can be handled with linear elasticity.
- The soil is considered incompressible during the plastic phase.
- The shear strength characteristics  $c_u$  or  $c$  and  $\Phi$  are assumed to be constant from the start of failure to infinite shear strain, in other words the soil is insensitive.

### 2.3.7 Conclusion

The MPM is a numerical method which utilizes the advantages of both Lagrangian and Eulerian methods. Element entanglement and mesh distortion, which often occur with Lagrangian methods, are not present in MPM. On the other hand, the numerical dissipation generally encountered with Eulerian methods is eliminated but the history of the MP's is tracked throughout the simulation. This makes MPM a suitable method for the simulation of large deformation problems like penetration, impact or blast.

The accuracy of a model increases when more aspects of the soil behaviour is taken into account. However, some aspects are specific for weaker soils and others for stronger soil. This makes certain constitutive models better suited for certain soil types. Knowing which aspects are applicable to the problem and which models suits the best is crucial (Zhang et al., 2017).

Geotechnical engineering is a complex field of work and using advanced numerical methods do not make it any simpler. The quality of the tool is important, but the quality of the results mainly depends on the user's understanding of both the problem and the tool (Rubbish in = Rubbish out). However, if properly used numerical methods are a powerful tool with significant advantages compared to conventional analysis.

## 2.4 Modelling of a Pressuremeter Test

The entire process of a pressuremeter test consists of two phases: (1) The installation of the pressuremeter module into the soil. And (2) the cavity expansion. If one wants to model both phases in the same model, boundary conditions on certain nodes (at the pressuremeter module) have to be changed mid simulation. This is a challenging task which is not available with the current MPM code. The two phases should therefore be modelled separately. This thesis focuses only on the first phase of the pressuremeter test.

### 2.4.1 Modelling of the Installation

The analysis by Moug et al. (2019) begins with a wished-in-place cone, followed by sufficient cone penetration to produce a steady distribution stresses and pore pressures throughout the mesh. However, instead of simulating the cone moving downwards into the soil, the soil body is moving upwards. Soil enters the model from the bottom and exits on the top. This is shown in figure 2.12

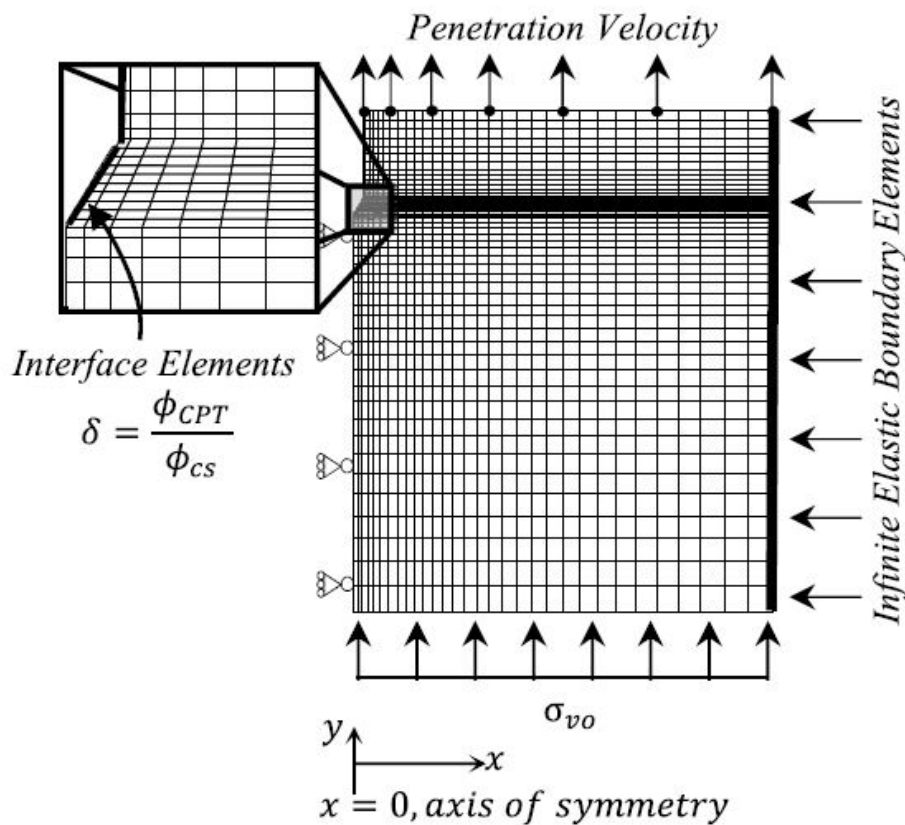


**Figure 2.12:** Model used by Moug et al. (2019)

Ceccato et al. (2016) used a two-phase material point method including a contact algorithm to simulate piezocone tests in a wide range of drainage conditions. The constitutive model which was used was the Modified Cam Clay model. The simulations agree with experimental data which was obtained from laboratory piezocone penetration tests in artificially reconstructed kaolin clay. These models did however not utilize a 2D axi-symmetric formulation given that it was not available at the time of the research. Instead, the authors of the paper modelled the piezocone penetration in a 3D mesh. In order to reduce the computational cost and by taking advantage of the rotational symmetry, only a 20° slice was modelled. This model used the moving mesh feature similar to the one described in Chapter 2

Subsection 2.3.4.3. The CPT device possesses a discontinuous edge at the base of the cone. At this location, boundary conditions are not uniquely defined. In order to circumvent numerical problems, the cone is therefore slightly rounded. The mesh size and refinement was determined through preliminary calculations. This study varied the penetration rate in order to simulate different drainage conditions and showed that the effect of partial drainage can lead to significant errors in the estimated material parameters for transitional soils. Figure 2.13 shows the model used by Ceccato et al. (2016).

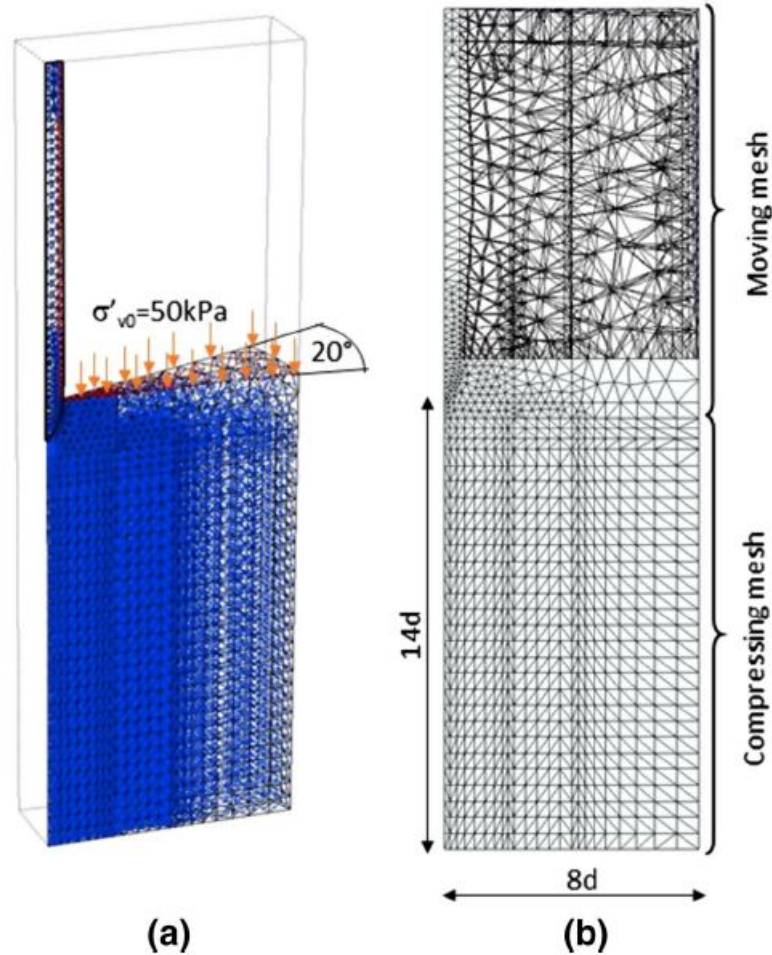


**Figure 2.13:** Geometry and discretization of the model used by Ceccato et al. (2016)

Tehrani & Galavi (2018) studied the effectiveness of the numerical cavity expansion method and the simulating the cone penetration test in dry sand using MPM. The results were validated using the an estimation of the cone resistance,  $q_c$ , by Salgado & Prezzi (2007).

$$q_c = 1.64p_A \exp(0.1041\varphi'_c + (2.64 - 0.02\varphi'_c)I_D) \left(\frac{\sigma'_h}{p_A}\right)^{(0.841-0.47I_D)} \quad (32)$$

In this paper three different relative density's (30%, 50% and 90%) have been modelled under a 25 kPa surface surcharge. All soil is assumed to be dry and the soil behaviour is modelled elastic-perfectly plastic using the Mohr-Coulomb failure criteria. The models were in very good agreement with the solution of Salgado & Prezzi (2007) as shown in Figure 2.14.

Phuong et al. (2014) researched the installation effects for piles in granular soils (Loose and medium dense sand) using MPM and found that the soil around the pile is heavily disturbed leading to (1) large shear deformations especially along the pile shaft and (2) compression especially near the pile

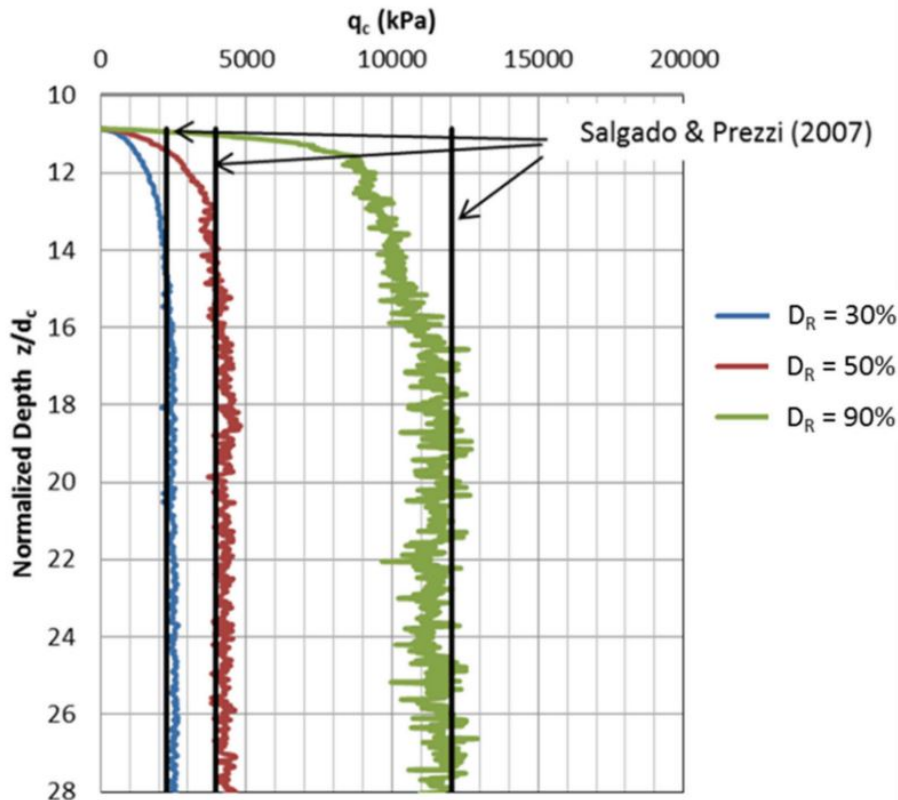


**Figure 2.14:** Cone resistance profile from MPM analysis (Tehrani & Galavi, 2018)

tip. These phenomena lead to a change in both stress state and density and therefore the behaviour of the soil around the pile. While the piles used in this research are much larger than the CPM device, the soil response due to the installation should be the same albeit to a smaller extent. This problem domain for this research was a  $20^\circ$  3D wedge which was based on the assumption of axisymmetric conditions. The constitutive model was Mohr-Coulomb.

It was found that after an installation of  $10D$  the radial stresses around the pile tip for both cases reached a peak value of 8 times the initial stress state. Below the pile tip the horizontal stress dropped below the  $k_0$  value. Although for the Mohr-Coulomb model, a change in density will not lead to a change in the resulting stresses, using a change of volumetric strains was used to identify zones of dilation or compaction.

#### 2.4.2 Conclusion

This section showed some of the work that previous researchers have conducted. Tehrani & Galavi (2018) modelled the penetration of a cone in dry sand using a 2D-axisymmetric model but only using a simple Mohr-Coulomb constitutive model. While Ceccato et al. (2016) used a more complex constitutive model, Modified Cam-Clay, to simulate a piezocone penetrating under different drainage conditions using a two-phase MPM code, the model did not implement a 2D-axisymmetric model and instead used a 3D model with a  $20^\circ$  slice of the problem. Phuong et al. (2014) looked into the installation effects for piles and found both a change in stress state and density can be expected which can also be expected to be present for the installation of a CPM. These researches show clear paths for further improvements into the simulation of a cone penetration using the material point method.

# Chapter 3

## Model Verification

### 3.1 Introduction

The verification of a models consists of ensuring that all conditions and parameters of the model are correctly chosen for the model, that the simulation is resulting in the expected result and that, for a phased analysis, the sequence of events is correct. In essence, a verification of a model is done to ensure that the computer model reflects the mathematical idealisation.

When setting up a model, the mesh is an important aspect when considering the accuracy of the results. Generally, a finer mesh will result in a accurate result. This does however come at the cost of more computational effort. It is therefore important to find the balance between numerical accuracy and computational efficiency. When setting up the model, it is advisable to increase the number of elements or material point density in areas where a high gradient in stresses and strains are expected. In this case that would be around the cone and shaft. When speaking of element density or material point density regarding the mesh it is meant as the number of elements or material points per area. The aim of this chapter is to find the optimal balance between numerical accuracy and computational efficiency. This will be done by exploring different mesh setups or material point densities and compare the outcomes. First the mesh size is elaborated, followed by the material points.

### 3.2 Mesh Description

This section will give a description of the problem domain. First, 2D-axisymmetric formulation is elaborated. Then, the size of the problem domain is discussed in terms of height and radius. Following that the refinement of the mesh is determined. Lastly, the moving mesh application is elaborated.

#### 3.2.1 2D-Axisymmetric Formulation and Conversion to 3D

As mentioned in Chapter 1, a 2D-axisymmetric model will be used to simulate the installation of the cone. The model will simulate a slice of 1 radian. One set of the outputs of the model will be the sum of the reaction forces in X- and Y- direction for both the cone tip and the cone shaft. To convert these force back to a 3D situation, these forces have to be multiplied by a factor  $2\pi$ . With the 3D forces on the cone and shaft, the stresses can be calculated. For example, the cone resistance can be calculated by dividing the total force in the Y-direction on the cone tip by the equivalent area of the cone  $A_{eq} = \pi \cdot r^2$ . A schematic of the conversion of the cone tip is shown in Figure 3.1.

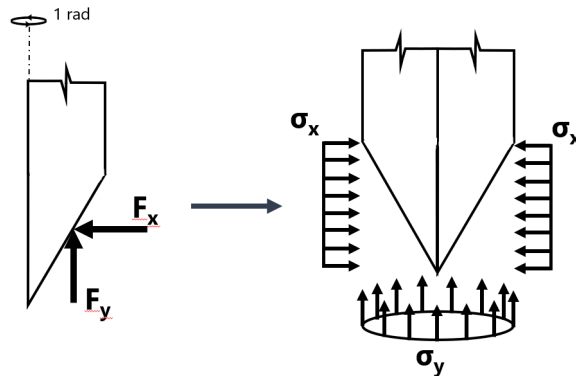


**Figure 3.1:** Conversion of forces in 2D to stresses in 3D for the cone tip

### 3.2.2 Mesh Size

In order to determine the mesh size, two aspects are considered. First the desired penetration depth and secondly the mesh has to be sufficiently large that the simulation is not subjected to boundary effects. Both are discussed in this subsection.

One essential part in determining the mesh size, is the required penetration depth. Since the aim of this research is to find the disturbance at the top of the pressuremeter module it is necessary that this disturbance has reached a steady state. Initially, the cone needs to be pushed in several diameters before the stress state in the soil will go from a K0 condition to the point where a steady state pressure is reached. This steady state has to be reached first before we can look at the disturbance of the soil next to the shaft. During penetration the soil will be pushed away by the cone and enters a compressed state. When the soil passes past the shoulder of the cone it will relax and a residual disturbance will remain. After the soil has passed the shoulder, the shaft will continue to shear the soil as it passes through the soil. From here the soil which has just past the shoulder has to reach the pressuremeter module. The required penetration depth then becomes the depth needed to reach a steady state of soil failure plus the distance from the cone tip to the top of the pressuremeter module. The top of pressuremeter module is located at 575mm distance from the pile tip which is equal to approximately 13D considering a standard 15 cm<sup>2</sup> cone (Cambridge Insitu, 2019).

As mentioned before, the mesh size has to be sufficiently large that the simulation is not subjected to boundary effects. In order to assess the effects of the boundaries, several different mesh sizes have been simulated. For the assessment of the bottom boundary effects, three different soil heights were investigated: 1m, 1.5m and 2m. These three models had a radius of 2.0m. For the radial boundary, three different radii were chosen: 0.7m, 1.0m and 2.0m. These models all had a height of 2.0m. Additionally, an extra large mesh with a soil height of 3.0m and a radius of 3.0m was created to ensure that this model contained no boundary effects. By having a model with no boundary effects, it was possible to confirm that the stress states encountered at the boundaries of the models were indeed not subjected to boundary effect. In total six different mesh size were chosen. These are summarized in Table 3.1. Initially, the penetration depth was set to 1.0m with the exception of the 1m soil height model since soil is simply not deep enough. For this model a penetration depth of 0.8m was chosen.

**Table 3.1:** Different mesh sizes used for boundary effects analysis

Mesh Type	Radius [m]	Soil height [m]	Penetration depth [m]
r20h10	2.0	1.0	0.8
r20h15	2.0	1.5	1.0
r20h20	2.0	2.0	1.0
r10h20	1.0	2.0	1.0
r07h20	0.7	2.0	1.0
r30h30	3.0	3.0	1.0

Looking at the cone resistance profile, shown in Figure 3.2, we can see a clear convergence for an increasing mesh radius. In general, the mesh height does not show any difference in the reaction forces with the exception of the r20h10 model where it can clearly be observed that the bottom boundary is affecting the cone resistance profile. In order to get a more detailed view of the changes in the stress state at the boundaries for the different models, several cross-sections have been compared. These cross-sections are located 0.05m from the boundary. The different locations of the cross-sections can be seen in Figure 3.3. This figure also shows the final location of the cone after 1.0m penetration. The cone itself is not drawn to scale.

Figures 3.4 and 3.5 show the horizontal and vertical (resp.) stress state at vertical cross-sections A' - A' to D' - D' after 1.0m of penetration. In the graphs, each individual cross-section is visualized with

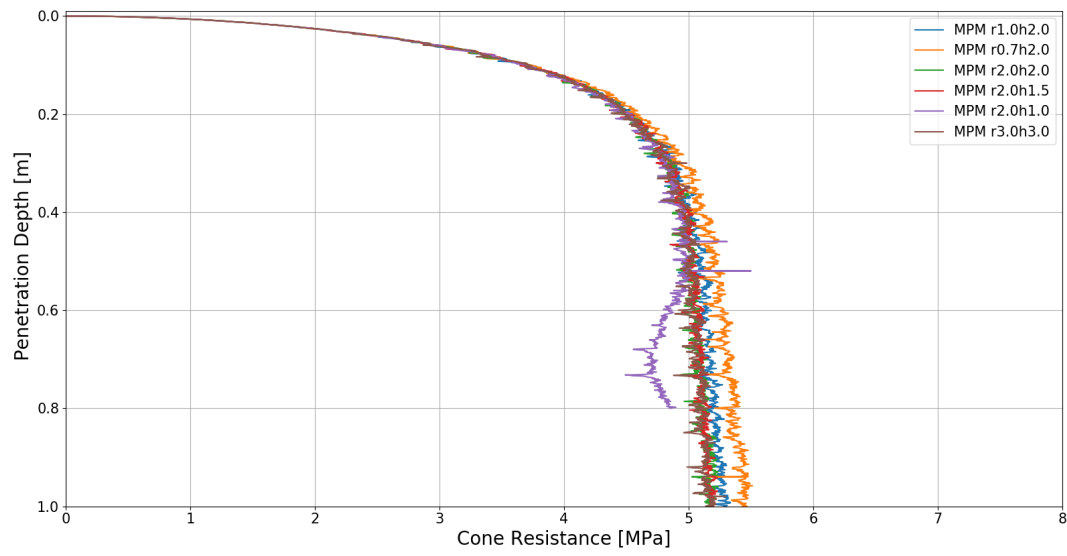


**Figure 3.2:** Cone resistance profile for different mesh sizes

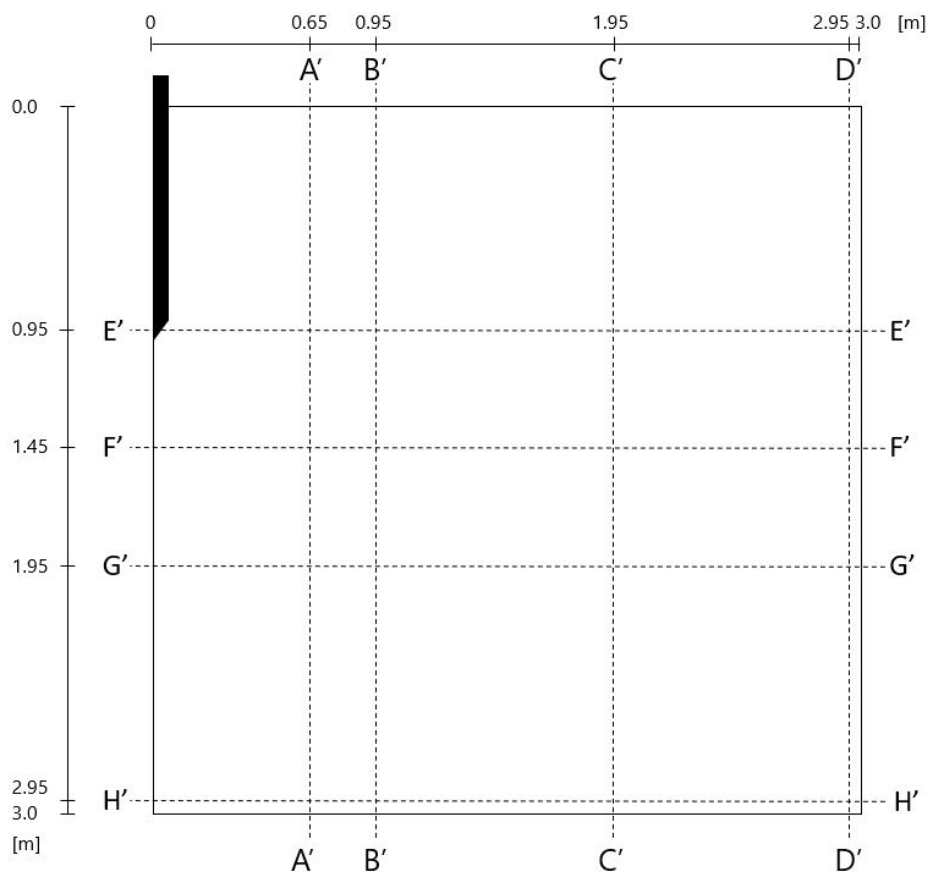


**Figure 3.3:** Location of the stress state cross-sections

the same color. The different shades of the colors indicate different mesh sizes with lighter shades for a smaller mesh and a darker shade for a larger mesh. For the horizontal stresses, a clear convergence is observed at both cross-sections A' - A' and B' - B' as a radius of 2.0m or 3.0m result in a very similar stress state curve. At cross-sections C' - C' and D' - D' we can observe that stress increases virtually linear over the depth but with a small overall increase of the stress compared to the K0 stress.

When looking at the vertical stresses it can be observed that the differences between the several mesh sizes are much smaller but that the same conclusion can be drawn: The mesh types with a radius of 2.0m and 3.0m result in the same stress state while the effect of the boundary is clear for the mesh types with a radius of 0.7m and 1.0m. For the vertical stress no overall increase in the stress state is observed compared to the K0 stress as was seen for the horizontal stresses.

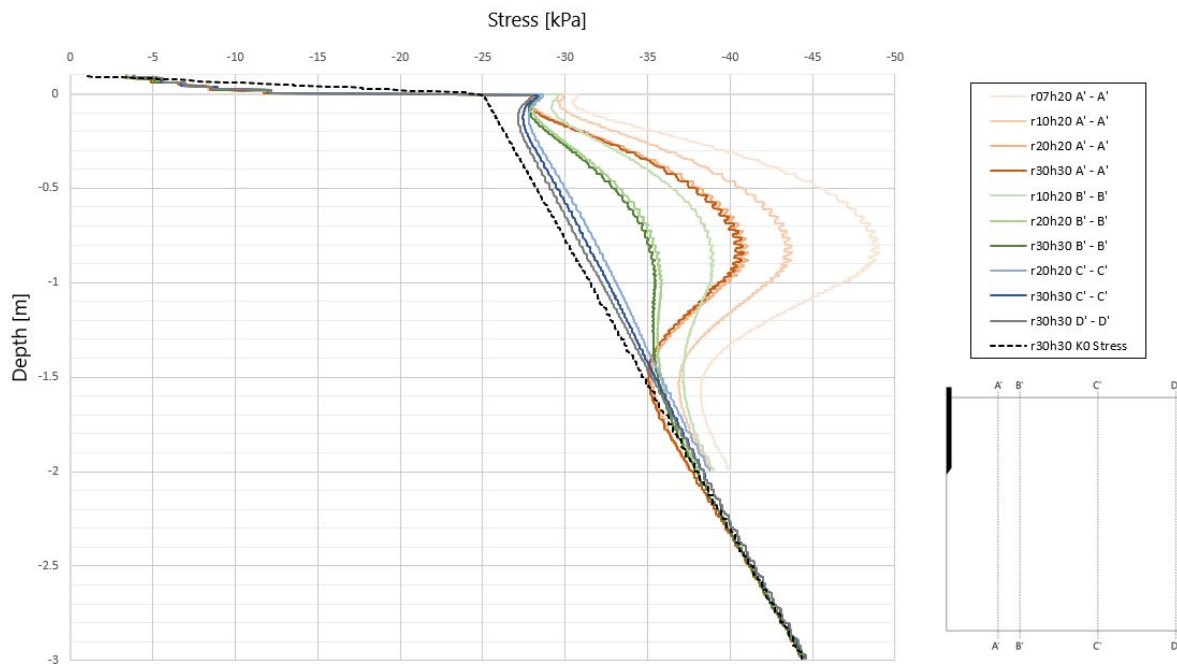


**Figure 3.4:** Horizontal stresses at different cross-sections in radial direction

For the comparison of the stress states at different heights a similar trend of convergence can be observed. Namely, that the amount of effect of the boundary decreasing with an increase in the model height. This is according to the expectations. Figures 3.6 and 3.7 show the horizontal and vertical (resp.) stress state at horizontal cross-sections F' - F' to H' - H' after 1.0m of penetration. Again, each individual cross-section is visualized with the same color. The different shades of the colors indicate different mesh sizes with lighter shades for a smaller mesh and a darker shade for a larger mesh. Both the horizontal as well as the vertical stresses show similar results, the models r20h20 and r30h30 give the same results and model r20h15 gives a different results which can be attributed to the bottom boundary effect. For the vertical stresses the models with a height of 2.0m and 3.0m at cross-section G' - G' also differ which suggests that for the r20h20 model the bottom boundary still effects the stress state throughout the model. Only the vertical stress near the bottom for the 3.0m model (cross-section H' - H') is constant in the radial direction. Similar to the vertical cross-sections in the radial direction, an overall vertical stress increase is observed of approximately 0.6 kPa.

Cross-section E' - E' has been omitted from these two figures given the fact that after 1.0m penetration the cone has passed this cross-section resulting in a high stress increase. This makes it more difficult to compare the other cross-sections because of scaling of the graph. Instead, Figure 3.8 and 3.9 show the horizontal and vertical stress state at cross-section E' - E' respectively. The change in both horizontal

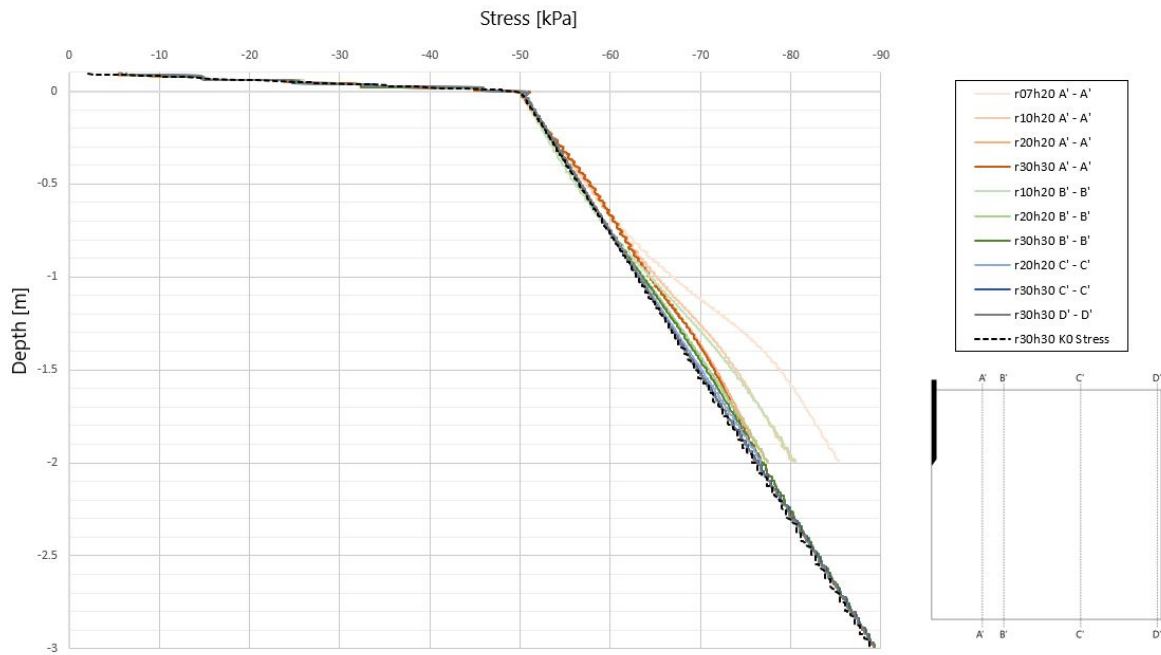


**Figure 3.5:** Vertical stresses at different cross-sections in radial direction

and vertical stress state resulting from the cone penetration is very similar for the three models with a height of 1.5m, 2.0m and 3.0m. This is in agreement with the observations made with the comparison of the reaction forces on the cone tip where the three different model heights resulted in similar reaction forces.

From this information it is concluded that a model with at least a radius of 2.0m and height of 3.0m is necessary to omit the boundary effects. This model size is still acceptable in terms of computational effort. The smallest model, r20h10, took a little under 5 hours to complete while the largest model, r30h30 took almost 13 hours to complete.

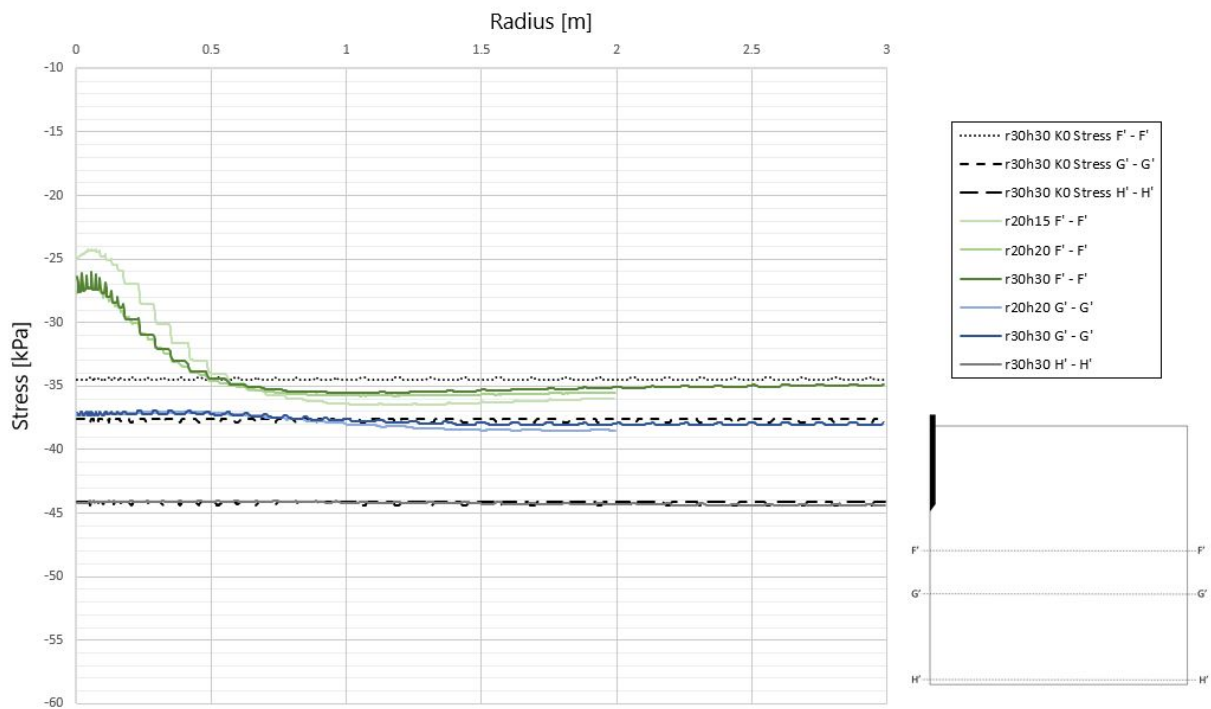


Figure 3.6: Horizontal stresses at different cross-sections in vertical direction

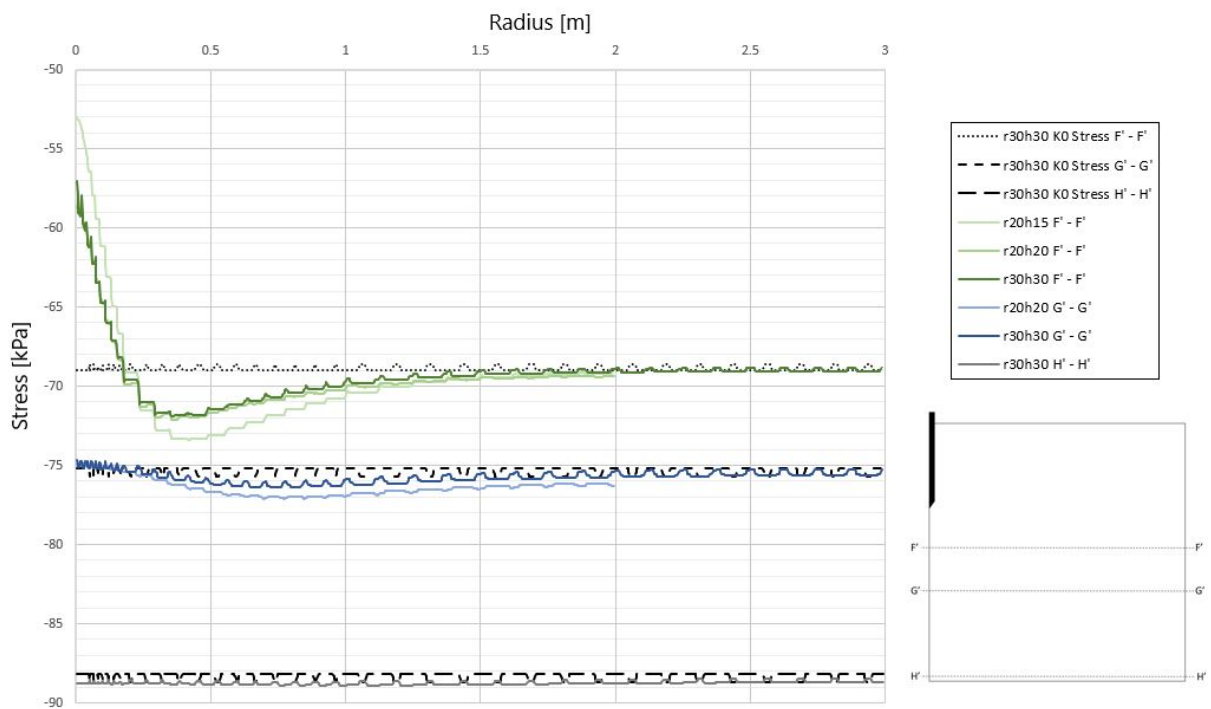
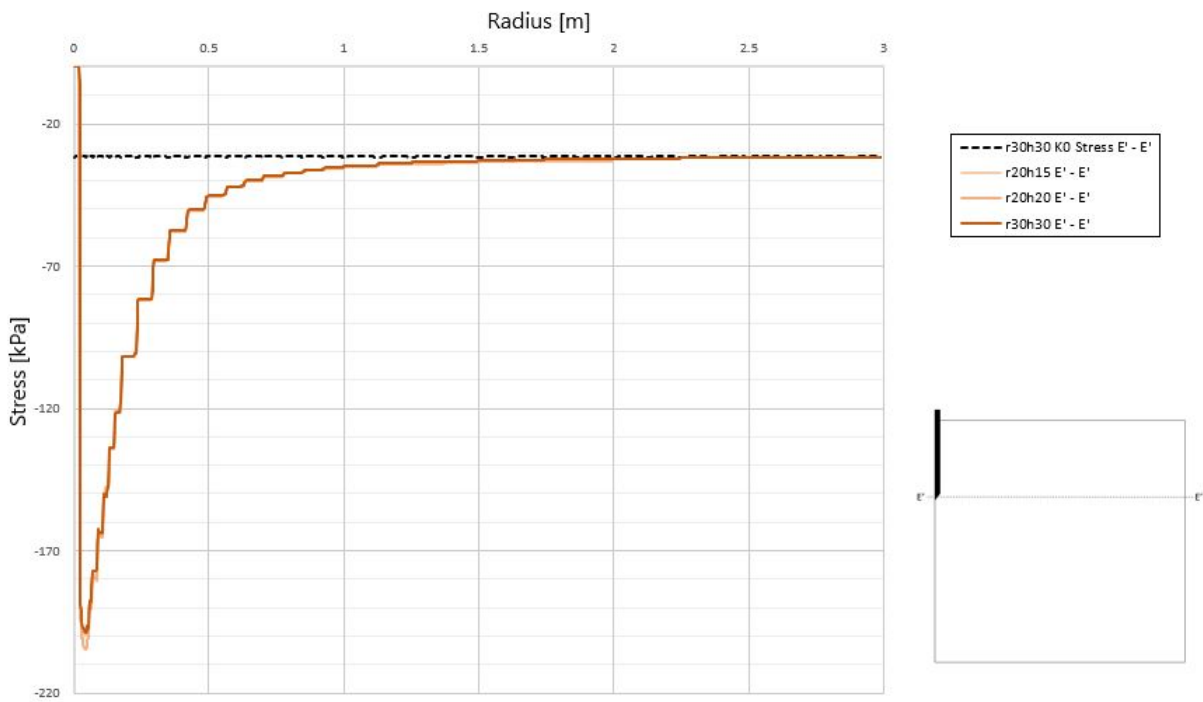
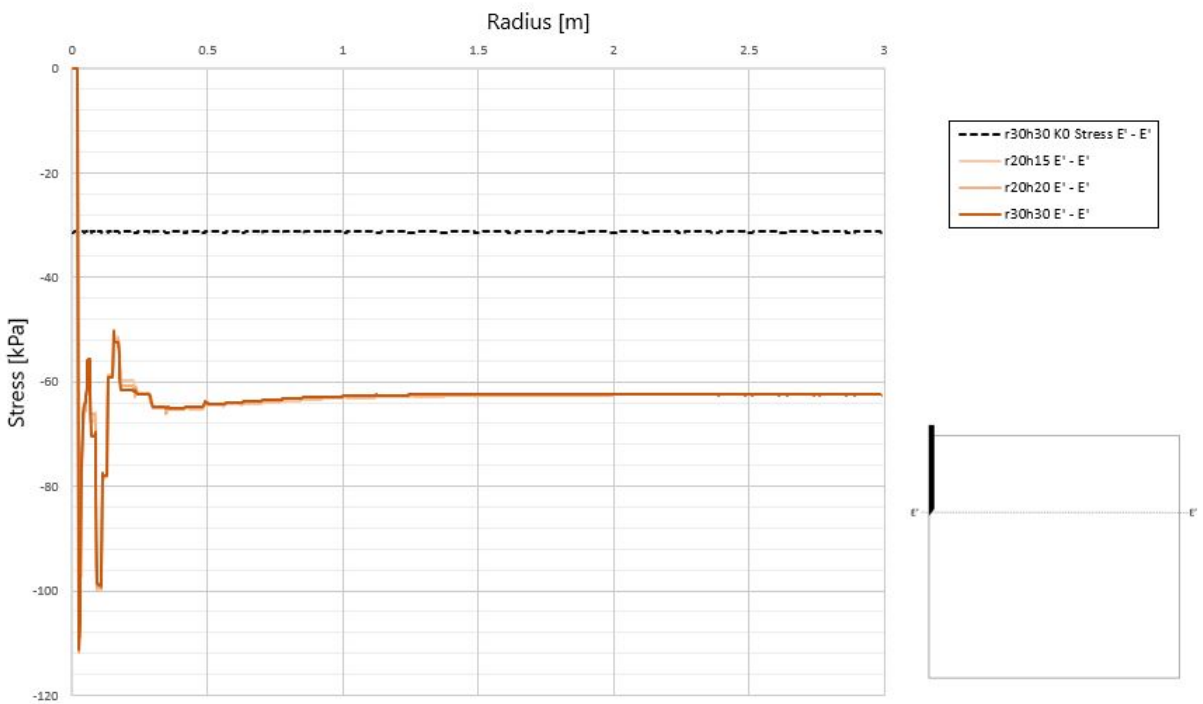


Figure 3.7: Vertical stresses at different cross-sections in vertical direction



**Figure 3.8:** Horizontal stresses at cross-section E' - E'



**Figure 3.9:** Vertical stresses at cross-section E' - E'

### 3.2.3 Mesh Refinement

When assessing the optimal mesh size for the problem, it is important to find a balance between computational efficiency and numerical accuracy. Typically, by refining the mesh the solution tends to converge. If this is the case, a further refinement does not yield any significant increase in numerical accuracy and only results in more computational effort. For this research, the reaction forces on the cone tip and on the cone shaft are used to assess the convergence of the simulation.

The element type chosen for the soil surrounding the cone is unstructured triangle elements. For the rest of the model, symmetric triangle elements are chosen. This is done to mitigate any preferential paths along the element for stresses and strains.

In order to find the suitable mesh refinement, a set of six meshes ranging from coarse to fine were created. These meshes were named MR1 to MR6 with MR1 being the coarsest and MR6 the finest mesh. The focus on the refinement is near the cone since here the gradients are largest. The different mesh refinements are given in Appendix A. In this analysis the constitutive model used was Mohr-Coulomb and the chosen model parameters are given in Table 3.2. The Young's modulus was chosen low in order to speed up calculations. Figure 3.10 shows the resulting cone resistance in which it becomes clear that convergence of the solution occurs for refinements MR4, MR5 and MR6. Therefore MR4 is chosen as the optimal refinement as it has been shown that further refinement does not yield in a significant increase in accuracy.

**Table 3.2:** Model parameters for mesh refinement analysis

Parameter	Value
$E$ [MPa]	1
$\nu$ [mm]	0.2
$\phi'$ [°]	30
$c$ [MPa]	0

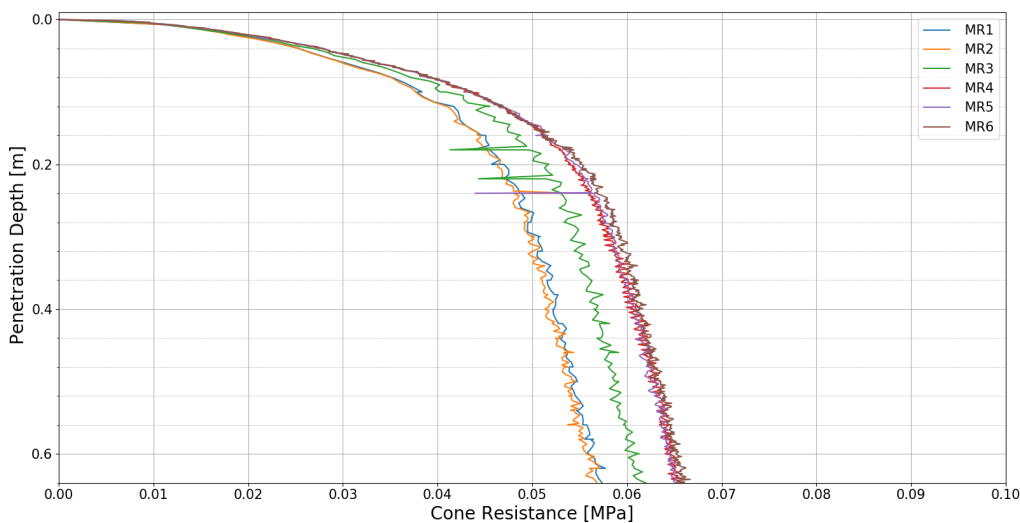


**Figure 3.10:** Cone resistance profiles for mesh refinement analysis

During the modelling, it was found that the model showed signs of mesh dependency as shown in Figure 3.11 which shows the radial strain after 1.0m penetration. It can be observed that this mesh dependency is the result of having straight lines in the mesh which lead to preferential paths in the model. In order to counteract this feature of the mesh, it was chosen to add a section of unstructured elements in the area of interest, which is the area next to the cone shaft where the CPM module is located. The rest of the model is still using the symmetric mesh which gets increasingly coarser further away from the model in order to save computational effort. Figure 3.12 shows the mesh with the unstructured area. This area is initially located on top of the soil surface but will move into the soil due to the moving mesh feature, which will be discussed later in this section. The final mesh can be found in Appendix B.

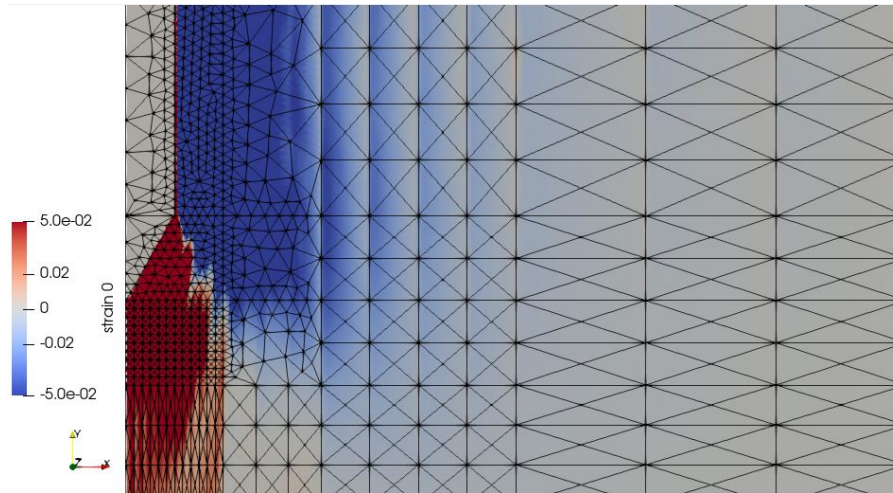


**Figure 3.11:** Mesh dependency of model

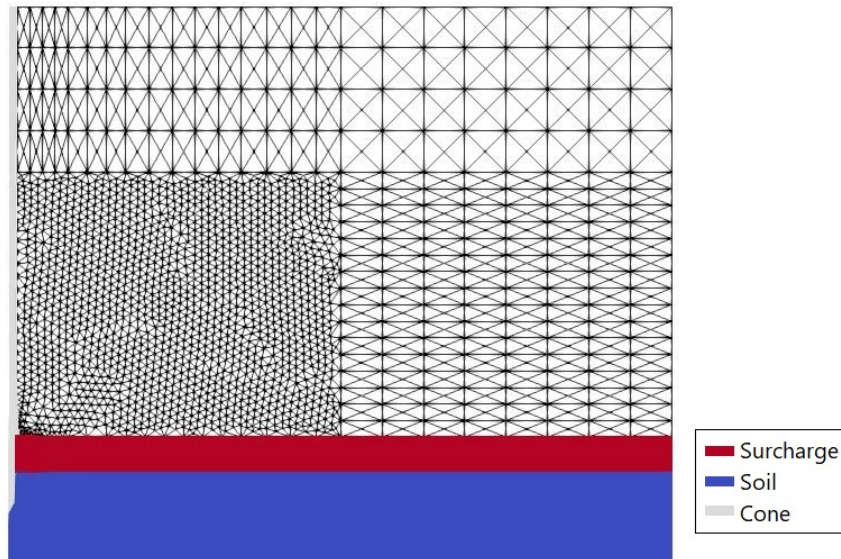


**Figure 3.12:** Unstructured mesh along the shaft

### 3.3 Material Points

In MPM, the material points (MPs) contain all the physical properties of the continuum like mass, momentum, location, stresses, strain and external loads. In contrast, the background mesh and Gauss

point carry no permanent information. The state variables are traced automatically and are carried independently of the computational mesh. This is one of the advantages of using MPM. One point of attention is that it is necessary that all elements of the computational mesh contain at least one MP throughout each simulation step. Therefore, the MP density has to be chosen such that this condition is met. If this condition is not met, information is lost and the simulation loses its usefulness. In addition, at locations with a high gradient in stresses and strains, a higher MP density is needed. For the created models, the MP density has been chosen with these two conditions in mind and while the exact MP density differs between the different models, the general MP density scheme is illustrated in Figure 3.13.

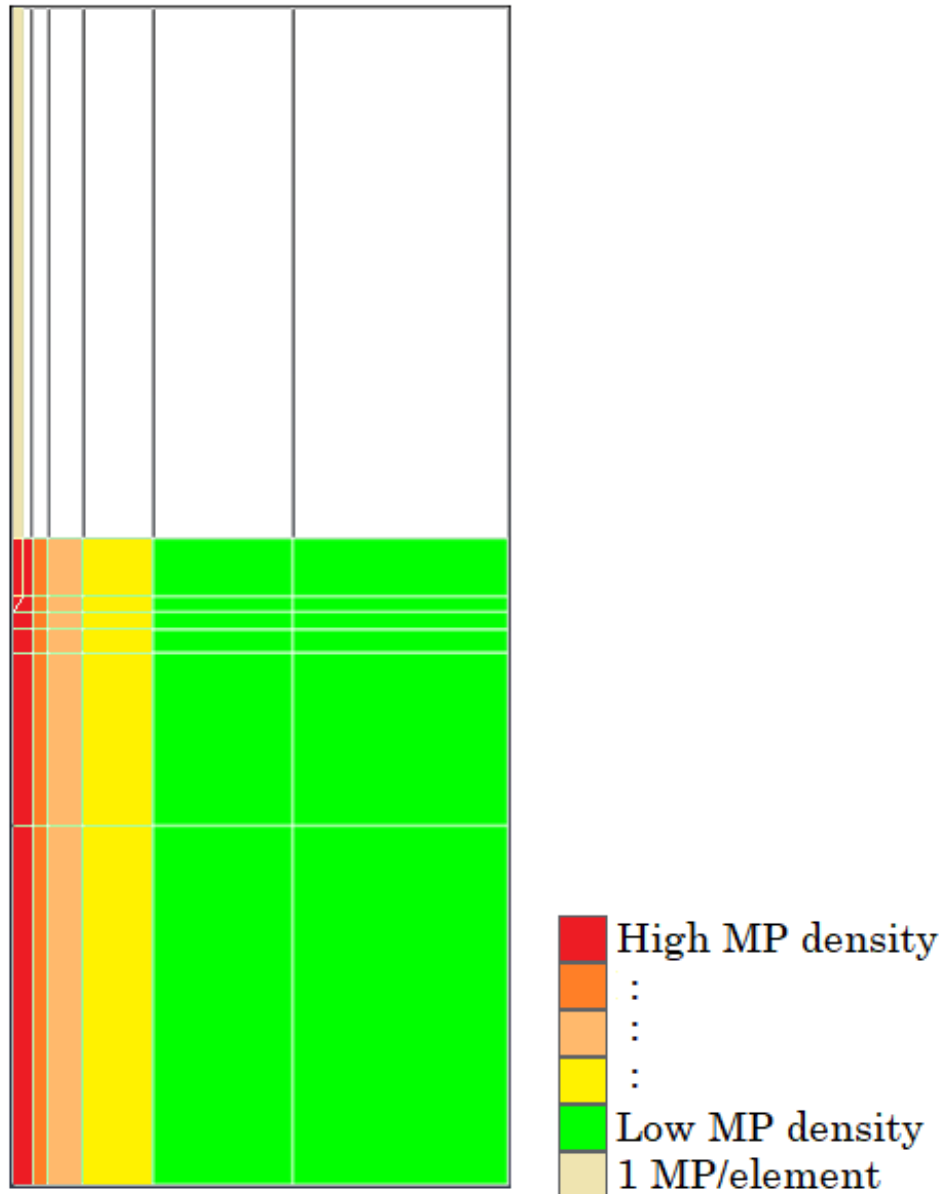


**Figure 3.13:** General MP density distribution

### 3.4 Model Features

This section will explain several of the model features selected for this research. These include features of the mesh like the moving mesh feature or chosen calculation options like the constitutive model.

#### 3.4.1 Surcharge

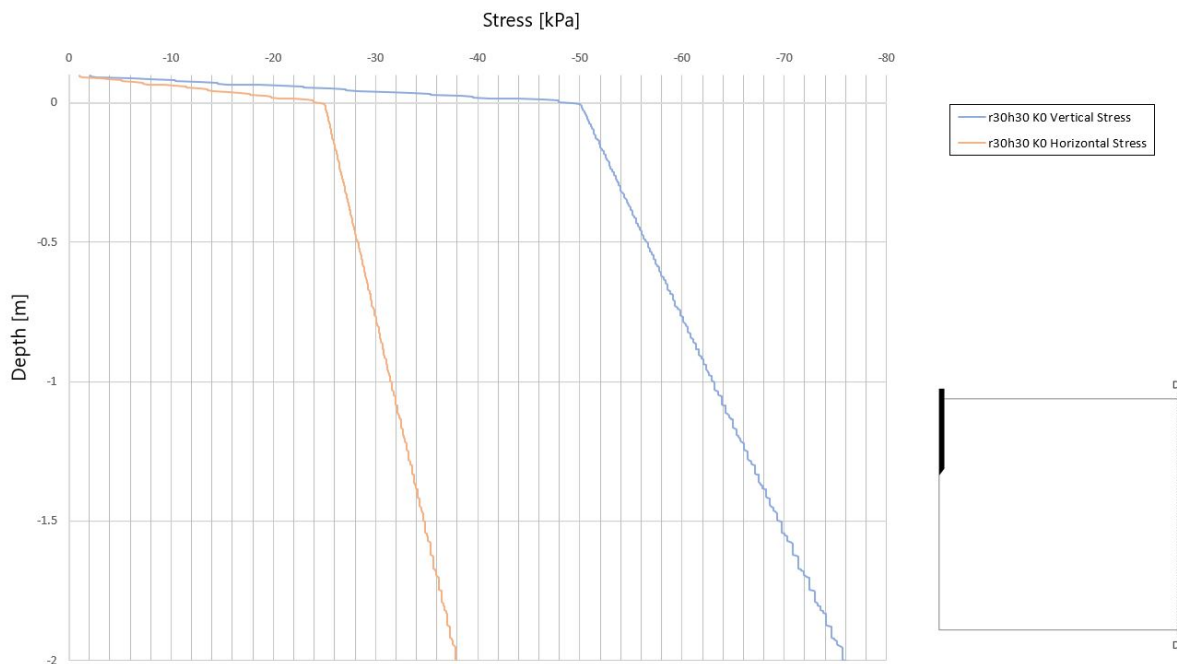
In this work the surcharge is simulated by changing the density of the first 0.1m of soil. The vertical stress in the K0 procedure is calculated using the following equation:

$$\sigma_v = (1 - n) \cdot \rho_s \cdot g \cdot d \quad (33)$$

Where  $n$  is the initial porosity,  $\rho_s$  is the density of the solids,  $g$  is the gravitational acceleration and  $d$  is the depth. For example, a surcharge of 50 kPa is achieved using the following values:

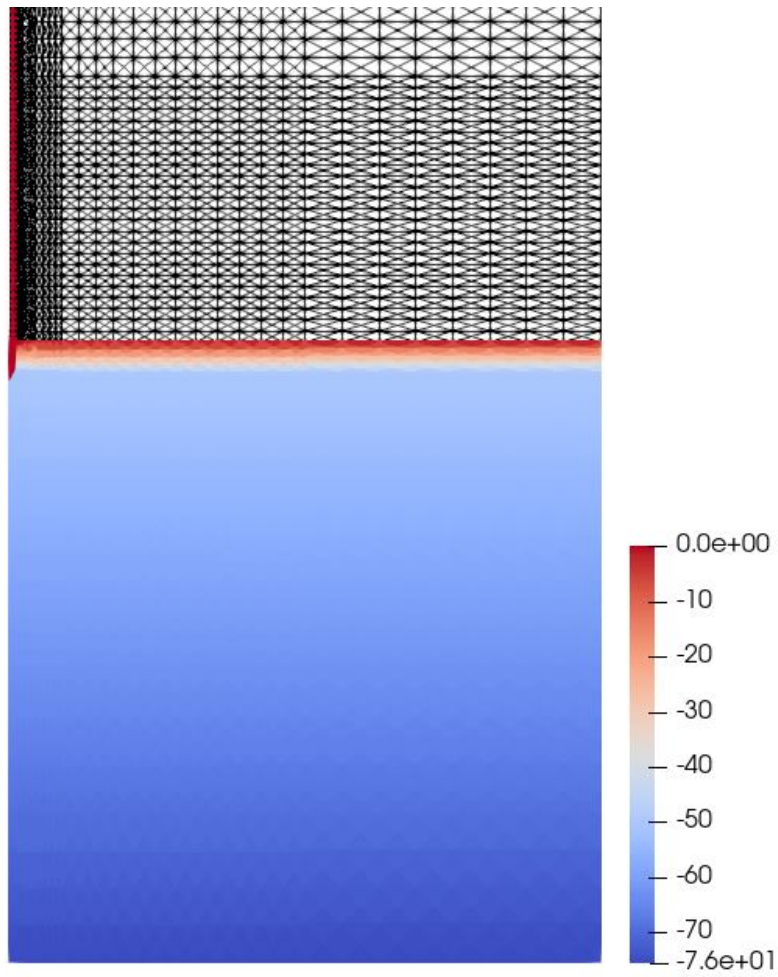
- $n = 0.5$
- $\rho_s = 101,936.8 \text{ kg/m}^3$
- $g = 9.81 \text{ m/s}^2$
- $d = 0.1 \text{ m}$

Figure 3.14 shows the vertical and horizontal stress after the K0 procedure. The K0 value was set to 0.5, this can be seen in the figure as the horizontal effective stress is half of the vertical effective stress. Figure 3.15 shows the contour plot of the vertical stress in K0 conditions.



**Figure 3.14:** K0 stresses with 50 kPa surcharge

A surcharge can be used to achieve several goals: Firstly, it can limit the free surface movement. If no surcharge is used, it could occur that material points on the surface fly off and leave the mesh leading to the unintended abortion of the simulation. Secondly, it can be used to simulate the cone penetration at a deeper location. While the use of a MPM code can simulate larger displacement compared to a FEM simulation, simulating a full CPT test of e.g. 30m is unfeasible due to the required computation time. A simulation of 1m penetration takes approximately 10 hours in a 3.0m model let alone a 30m penetration is a model larger than 30m. Therefore adding a surcharge to the soil to simulate a deeper soil state is a reasonable option.



**Figure 3.15:** Vertical stress contour plot

### 3.4.2 Moving Mesh

When the cone penetrates into the soil and the shaft moves down through the problem domain, parts of the mesh become redundant. In order to increase computational efficiency, the model uses a moving mesh feature. The moving mesh concept is explained in Section 2.3.4.3. With this feature the mesh can be divided in two parts: The first is the moving mesh and the second is the compressing mesh. The moving mesh is defined from the top of the model to 0.0756m underneath the cone shoulder ( $y = -0.0756\text{m}$ ). This is twice the cone height to ensure that the computational mesh around the cone remains the same throughout the simulation. The compressing mesh is defined from  $y = -0.0756\text{m}$  to the bottom of the model. Figure 3.16 gives a visualization of this feature. When generating the mesh, attention has been paid to the width to height ratio of the compressing elements in term of mesh quality which have to stay reasonable during the simulation.

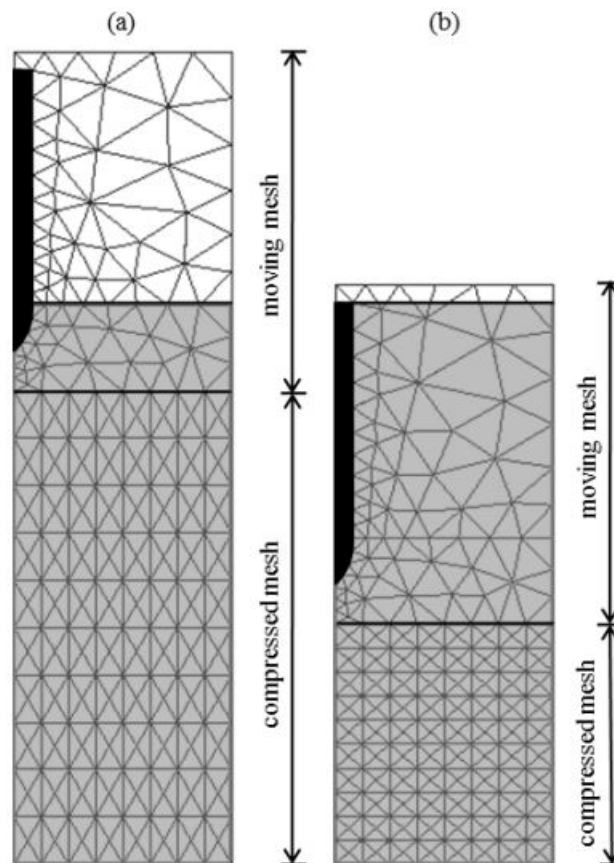


**Figure 3.16:** Moving mesh concept: (a) Initial state, (b) End of simulation (Phuong, 2019)

### 3.4.3 Strain Smoothing

The MPM formulation has been built using the FEM formulation as a basis. This results in the fact that most of the existing knowledge of FEM can be used for MPM. While MPM does mitigate many of FEM shortcomings, some issues have been transferred to MPM. One of these limitations is the kinematic locking that can occur in low order elements (Ceccato et al., 2019).

One example of this problem is given in Figure 3.17. Element e1, in Figure 3.17a, consist of the fixed nodes 1 and 2, and node 3 which is free. If the element is incompressible, the area of the triangular element must remain constant and  $u_y^3 = 0$ . The only remaining degree of freedom is the horizontal displacement  $u_x^3$ . Likewise, for element e2, in Figure 3.17b, the only degree of freedom of node 5 is  $u_y^5$  and  $u_x^5 = 0$ . Now, if we combine the two elements as can be seen in Figure 3.17c, element e1 requires

$u_y^3 = 0$  and element e2 requires  $u_x^3 = 0$  resulting in node 3 to be locked up. This locking will usually propagate throughout the entire mesh resulting in an unrealistic stiff response and numerical errors.

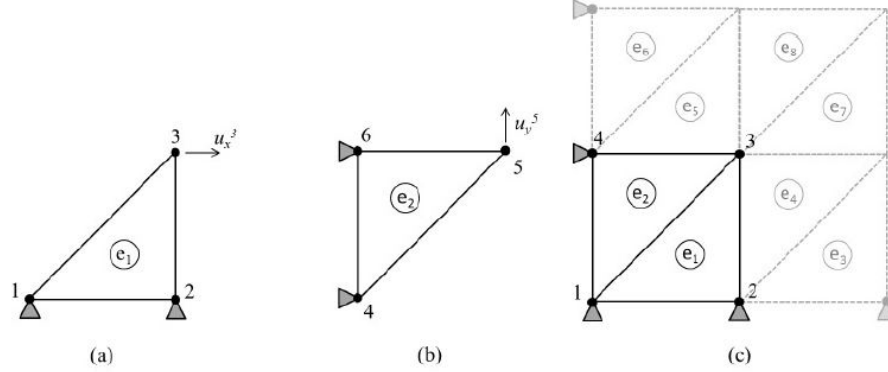


**Figure 3.17:** Example of kinematic locking in MPM/FEM modelling (Ceccato et al., 2019)

In the MPM codes used in this work, the Nodal Mixed Discretization technique for linear tetrahedral elements is used. In this technique the volumetric behaviour of an element is averaged over the elements sharing its nodes via a least squares smoothing process which are then assigned back to the material points (Detournay & Dzik, 2006). Ultimately, using the NMD scheme increases the number of degrees of freedom per element.

### 3.5 Constitutive Model

This research limits itself to the available elastic-plastic constitutive models. These are Mohr-Coulomb (MC), Hardening Soil (HS) and Mohr-Coulomb Strain Softening (MCSS). The constitutive model should be able to capture most of the soil behaviour aspects encountered in the simulation. In a large deformation problem, parts of the soils are expected to, at some point, experience both small and large deformations. Small deformations are accompanied with a peak state soil response and large deformations are accompanied by a critical state soil response. The constitutive model should therefore be able to model both peak and critical states. For a constitutive model to be able to capture both soil states, some sort of softening is required. Neither the MC model or the HS model can capture softening while the MCSS model can simulate soil softening.

Up until this point, dilatancy was omitted due to the fact that the standard Mohr-Coulomb model does not allow for the modelling of both the peak and residual parameters. This in combination of the large displacements resulted in an unrealistic amount of volumetric strains. However, the use of a Mohr-Coulomb Strain Softening model could solve this problem. In this model, the softening behaviour is accounted for by reducing any or all of the following Mohr-Coulomb parameters  $\phi'$ ,  $c'$  and  $\psi$  with the accumulated plastic deviatoric strain,  $E_d^p$ . In this model an exponential function is used with a shape factor  $\eta$  as shown in Equation 34 (Ceccato et al., 2019). A higher shape factor results in a higher rate of softening. This is illustrated in Figure 3.18.

$$\begin{aligned}
 c' &= c'_{res} + (c'_{max} - c'_{res}) \exp(-\eta E_d^p) \\
 \phi' &= \phi'_{res} + (\phi'_{max} - \phi'_{res}) \exp(-\eta E_d^p) \\
 \psi &= \psi_{res} + (\psi_{max} - \psi_{res}) \exp(-\eta E_d^p)
 \end{aligned} \tag{34}$$

Where the subscripts res and max refer to the critical and peak states respectively.

In this section the possibility of using the Mohr-Coulomb Strain Softening model is investigated. The Mohr-Coulomb Strain Softening model will soften the dilatancy angle based on the accumulated

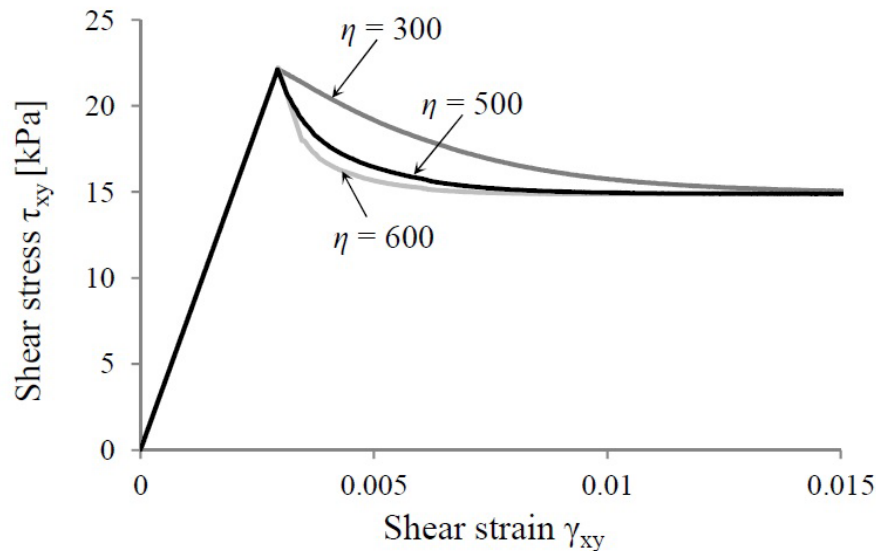


**Figure 3.18:** Effect of shape factor on strain softening rate (Ceccato et al., 2019)

strains. This is a much more realistic soil behaviour. Three model will be simulated and discussed with: (1) No dilatancy, (2) Dilatancy, no softening and (3) Dilatancy with softening.

For the investigation of the MC Strain Softening model a  $\psi_{max}$  of  $5^\circ$  was chosen.  $\psi_{res}$  was set to  $0^\circ$ .  $c'$  and  $\phi'$  were constant during the simulation. The shape factor  $\eta$  was set to 50. This results in the dilatancy angle being reduced to  $0^\circ$  after the strains reached 6%. Figure 3.19 shows the cone resistance profiles for the three simulations. From these graph, the following observations can be made:

- Dilatancy increases the cone resistance
- Dilatancy increases the initial gradient of the cone resistance profile
- The difference between strain softening and no strain softening is significant in terms of steady state cone resistance. 4.4 MPa versus 7.3 MPa.
- Strain softening introduces a secondary increase in the cone resistance after  $\sim 0.5$ m penetration which returns to original steady state penetration near the end of the simulation.
- Using a constant dilatancy introduces numerical instabilities.

### 3.6 Calculation Method

In the available MPM code, two calculation methods are available: (1) MPM-MP, where the state variables are calculated for every individual material point and (2) MPM-Mixed, where the state variables are averaged for each element and subsequently interpolated to the present material points in each element. MPM-MP is logically the more accurate calculation method but given the extreme high number of material points, up to 450.000 individual material points, using this calculation taken a lot of computational effort. Therefore, it is interesting to compare both calculation methods and see whether the MPM-Mixed can get similar results. Figure 3.20 shows the cone resistance profile for both calculation methods. Both model were exactly the same save the calculation method and used the Mohr-Coulomb Strain Softening constitutive model to also include the strain softening. What can be observed from the cone resistance profiles is that the intial parts of the profiles are very similar. Only after a certain amount of penetration, difference begin to show. The model with the MPM-Mixed calculation methods experiences a secondary increase of the cone resistance but comes back to the same cone resistance found using the MPM-MP calculation method. The difference of the final cone resistance is 2% and the maximum difference which is observed at a penetration depth of 0.75m is 7.5%.

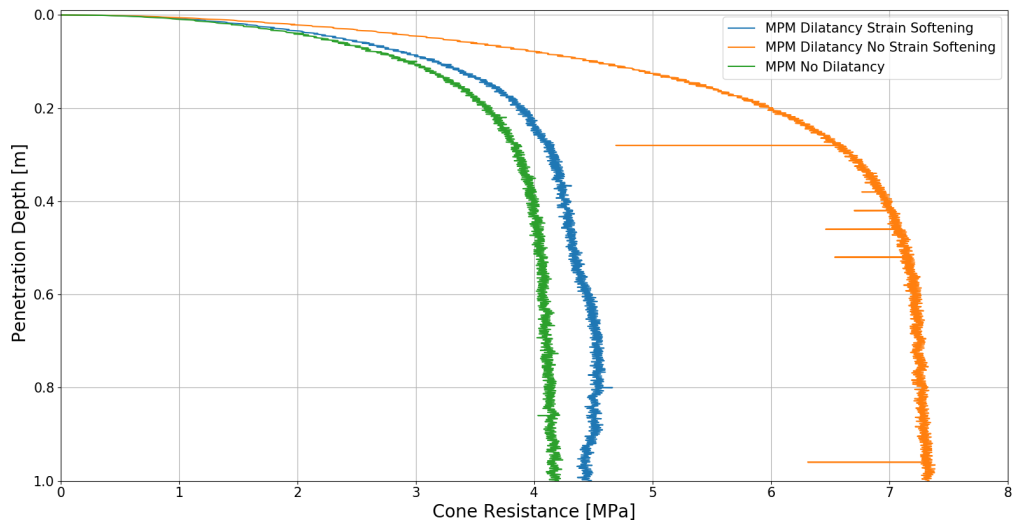


**Figure 3.19:** Cone resistance profiles to investigate strain softening behaviour

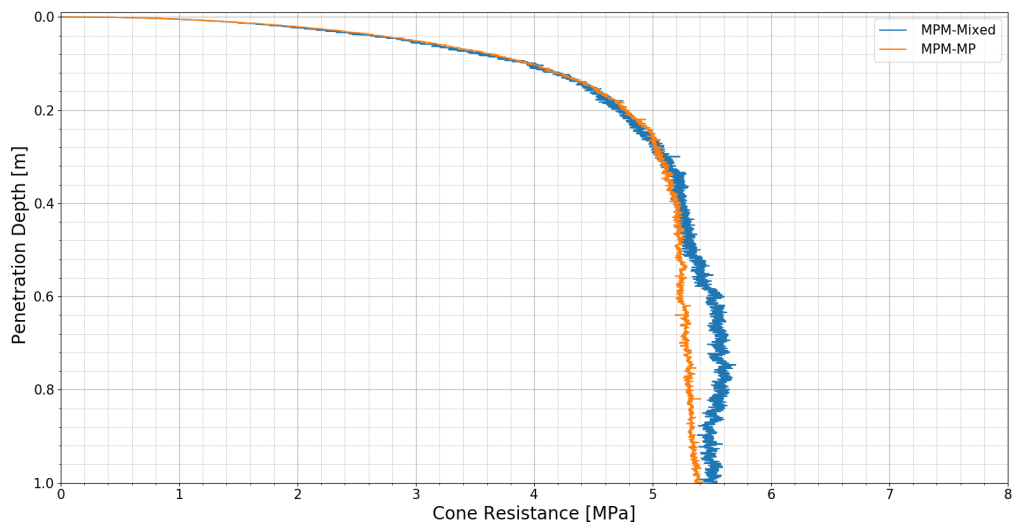


**Figure 3.20:** Cone resistance profile for both calculation methods

In terms of computational effort required by both calculation methods we see a clear difference. The more accurate MPM-MP calculation method took roughly 98 hours to complete while the MPM-Mixed method only took 12 hours to fully simulate the problem. This means that the MPM-MP takes a factor  $\sim 8$  longer than the MPM-Mixed method to conduct the simulation. This increase in required computation time is significant given the sensitivity analysis that is conducted which requires numerous different models.

We can state that both calculation methods provide similar results except for the bulge at a certain amount of penetration and given the sheer computational effort saved by using the MPM-Mixed calculation method, this method is chosen to be used for the rest of the models.

### 3.7 Determination of the Plastic Radius

In a Mohr-Coulomb constitutive model plastic strains occurs if and only if the Mohr circle touches the failure criterion line ( $f = 0$ ). In the used Mohr-Coulomb Strain Softening model, these build-up plastic strains results in softening of the strength parameters of the soil as shown in Subsection 3.5. By investigating the stress state at a certain depth in the Mohr-space, we can determine up to which radial distance from the cone the MPs have experienced plasticity. Thus we can determine the plastic radius. In this example the plastic radius is determined after a 1.0m penetration and at a depth of 0.5m. It is easiest to approach the determination of the plastic radius from a large radial distance towards the cone. Far away from the cone, we have a  $K_0$  situation, the soil is in an elastic state and thus the Mohr circle stays below the failure line. If we get closer to the cone, the Mohr circle increases due to an increase in the largest deviatoric stresses which are the result from the cone penetration process. This increase continues up until the radial distance at which the Mohr circle touches the failure line. This moment is shown in Figure 3.21 and occurs at a radial distance of 0.43m. In this figure, the bar above the graph indicates the radius at which the Mohr circle is drawn. From this figure we can observe that the deviatoric stress between the vertical and the tangential stress drives the failure. Analytical solutions for cavity expansion, like the one from Baguelin et al. (1978), do not take the vertical stress into account when determining the plastic radius. Admittedly, the solution by Baguelin is an 1D solution but this shows that in a 3D case the vertical stress plays a major role in the development of plasticity in the soil.

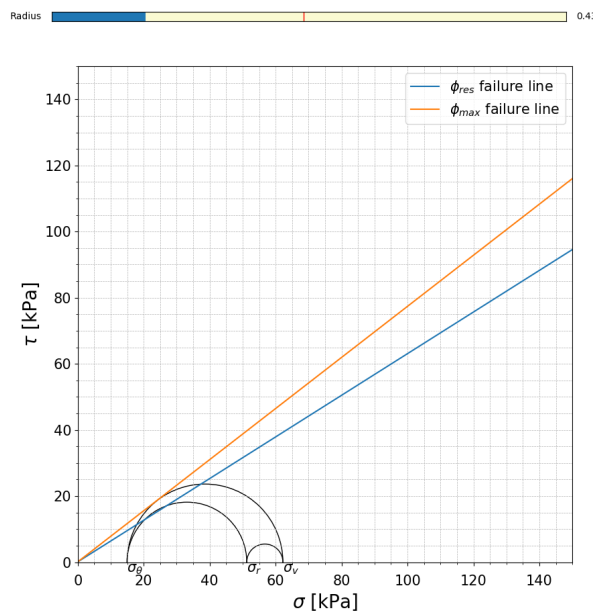


**Figure 3.21:** Plastic Radius at 0.5m depth

If we go closer from the plastic limit towards the cone we enter a softening zone in which the friction angle reduces due to the accumulated plastic deviatoric strains. This results in a decreased failure criterion until the residual failure line is reached. At this particular radius, the Mohr circle touches the  $\psi_{res}$  failure line and only the residual friction and dilatancy angle remain. In this case that radius is 0.17m and the corresponding Mohr circle is shown in Figure 3.22. In this figure we can see that in fact the radial stress is the largest stress in contrast to what was observed at a larger radius where the vertical stress was largest. From this radius inwards the Mohr circle does not cross the residual failure line indicating that the strain softening component of this constitutive model works as intended.

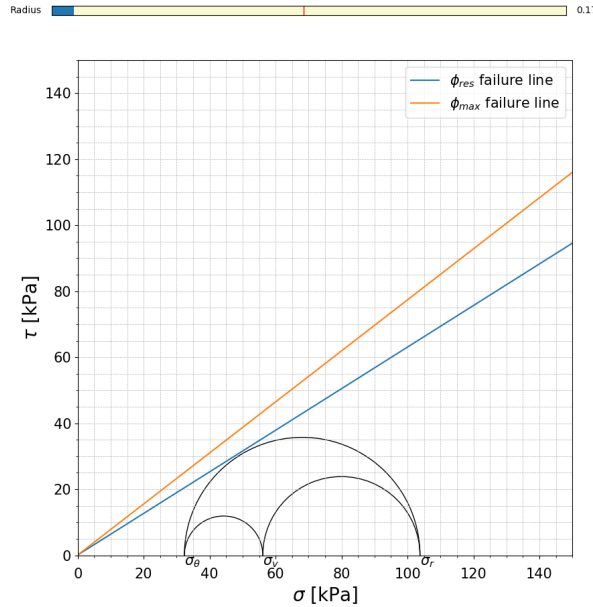


**Figure 3.22:** Radius at 0.5m depth where the soil has fully softened

Even closer still we find that the Mohr circle averts from the failure criterion as indicated in Figure 3.23 as the mean stress becomes much larger compared to the deviatoric stress. It is at this point in the model that some numerical issues arise due to the immense gradient in the stresses. This can be seen in Figure 3.24 where the stresses over the radial distance are shown. This graph also includes the theoretical plastic radius according to Baguelin et al. (1978) which was explained in Subsection 2.2.3.2. The analytical value for the plastic radius was 0.509m while the MPM model resulted in a plastic radius of 0.43m. The difference between the analytical value and the value obtained from the given MPM analysis is 15.5%. It can also be observed that the analytical value of  $\sigma_\theta$  and the  $\sigma_\theta$  obtained from the MPM model are mostly in agreement. However, the difference between in close vicinity to the cone is significant. This is most likely due to the 3D effects which are omitted in the analytical solution.

With this method, it is possible to determine the plastic radius at any stage of the simulation. One could argue that the stress state prior to the stress state observed after 1.0m penetration was such that the plastic radius was in fact larger than the obtained plastic radius of 0.43m. However, if that would be the case, the mobilized friction angle could not have been the same as the peak friction angle as shown in Figure 3.21 since any plastic strains would have softened the friction angle.

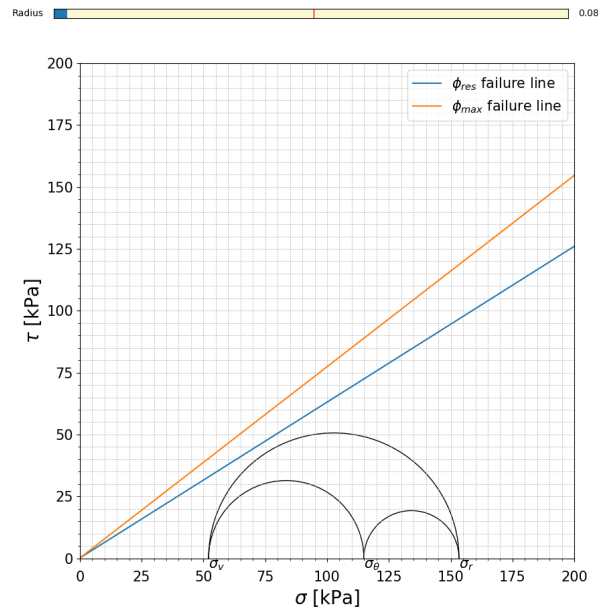


**Figure 3.23:** Mohr circle close to the cone

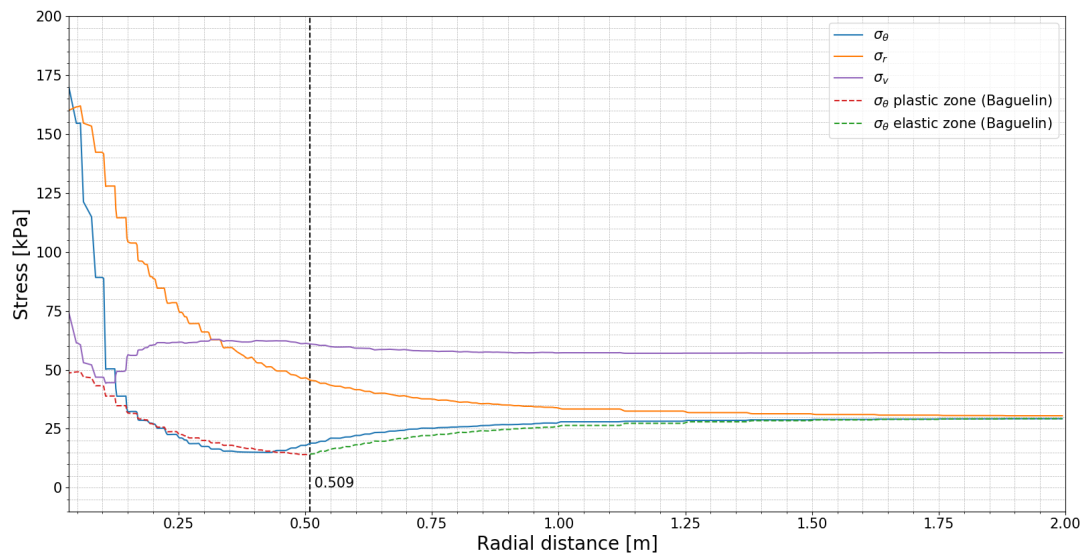


**Figure 3.24:** Stress state as function of radial distance

### 3.8 Conclusion

This chapter gives the description of the model which is used in this research. It was found, by investigating the boundary effects, that a model height of 3.0m and a radius of 2.0m is best suited for this research. The penetration depth is set to 1.0m. In terms of refinement, near the cone a finer mesh with unstructured elements is necessary given the high gradient in stresses and strains in this area. Further away from the cone, a coarser mesh with symmetric elements is sufficient. A 50 kPa surcharge is applied to the soil, this is achieved by increasing the density of the first 0.1m soil. The chosen constitutive model is the Mohr-Coulomb Strain Softening model which will model softening behaviour of the soil based on the accumulated plastic strains. Using the MPM-Mixed calculation method, significant computation time will be saved by averaging state parameters over each element and subsequently interpolating them the material points. A model with these parameters takes approximately 10 hours to complete.

With the model verification complete, the validation of the model can be carried out. This is done in the next chapter where a combination of various methods are utilized to validate the results. Both the cone resistance profile and the given plastic radius determination method will be used to find the sensitivity of the results to the various parameters in the sensitivity analysis conducted in Chapter 5

# Chapter 4

## Model Validation

### 4.1 Introduction

The validation of a model is done to ensure that the numerical predictions are representative to a real problem. This is often done by comparing the numerical prediction to experimental data, simplified models or past experiences. It is important to understand the limitations and assumptions of a given simulation.

The installation of CPM is identical to the cone penetration processes. In geomechanics, the CPT is praised for its simplicity in practice. The apparent simplicity of the cone penetration process does however hide considerably complex mechanics (Salgado et al., 2013). This mechanics include possible partial drainage during penetration; particle size effects; large deformations, rotations, shear deformations and mean stresses that develop around the cone; and the particle crushing that takes place near the cone. This complexity leads to significant challenges in theoretical modelling of cone penetration. The most applicable analyses for sand have been based on cavity expansion analysis. When the problem of interest, the installation of a CPM in this case, is difficult to solve theoretically, the value of numerical modelling increases.

In order to enable the results of the numerical model to be used, validation of the model is essential. By validating the model, we can confirm that the model gives us reasonable results which can be used to better understand the mechanisms encountered with the cone penetration process. The most compelling method of validating a model is to use experimental data where the conditions can be controlled to be equivalent to the model. However, given that the goal of this research is to find the disturbance around the shaft together with the fact that this disturbance is impossible to measure, using direct experimental measurements to validate the model is not possible. Most research is focused on the mechanisms which take place around the cone. Investigations into these mechanisms consist of calibration chamber experiments and image-based analysis. The cone resistance,  $q_c$ , is the main parameter in these investigations. First, the validation strategy is elaborated followed by the actual validation results.

### 4.2 Validation Strategy

In this section the validation strategy is discussed. The validation consists of a combination of both experimental data and image based data from Arshad et al. (2014) and a correlation for  $q_c$  developed by Salgado & Prezzi (2007). These three methods will form the validation strategy and are elaborated in this section respectively.

#### 4.2.1 Experimental Data

Arshad et al. (2014) performed a series of 8 half cylindrical calibration chamber tests on a coarse-grained, unground silica sand (#2Q-ROK). In this series of laboratory tests, the CPTs were conducted in the sand under a surcharge of 50 kPa with different relative densities ranging from 42% to 85% The test series and resulting cone resistance profiles can be found in Appendix C. The #2Q-ROK sand is mined from the Oriskany sandstone deposits at Berkely Springs, West Virginia. Arshad et al. (2014) also performed a serie of laboratory tests to determine some of the properties of the #2Q-ROK sand. The experimental data is used to obtain the model parameters for this sand. The properties of this sand are given in Table 4.1. The index properties of the sand were determined according to ASTM standards (D2487, D4254 & D4253). The peak and critical state friction angles were estimated from direct shear tests conducted in a 60mm square shear box in two series of tests. One in loose sand

( $D_R = 32 \pm 3\%$ ) and the other in dense sand ( $D_R = 78 \pm 3\%$ ). The direct shear tests were conducted with normal stresses ranging from 60 to 442 kPa.

**Table 4.1:** Properties of #2Q-ROK sand (Arshad et al., 2014)

Parameter	Value
$G_s$ [-]	2.65
$D_{50}$ [mm]	0.78
$Cu$ [-]	1.43
$e_{max}$ [-]	0.998
$e_{min}$ [-]	0.668
$\phi'_{peak}$	40.3°
$\phi'_{critical}$	32.2°
$c$ [kPa]	0

#### 4.2.2 Image-Based Analysis

Image-based analysis methods are used in laboratory investigations of the cone penetration process in particulate media. An image-based analysis can provide insight in the displacement paths and strains of the soil. It can also be used to create contour plots which provide valuable insight in the soil behaviour. These methods include X-ray film photogrammetry, X-ray television and X-ray CT techniques; Laser speckle interferometry; Transparent soil particles and, more recently, image correlation techniques such as particle image velocimetry (PIV) and digital image correlation (DIC). DIC enables the observer to study the response of the soil during the penetration, by using a transparent observation window located exactly on a symmetry plane of the penetrating probe. Arshad et al. (2014) described CPTs performed in a half-circular DIC chamber in order to study the cone penetration process in silica sand. In this research it was found that for shallow penetration, the displacement vectors near the cone tip are essentially vertical for crushable sand, transitioning to subvertical for less crushable sands. However, for deep penetration, the displacement vectors near the cone tip are mostly vertical below the cone tip. For deep penetration, the horizontal stresses are greater, confining the soil which reduces the horizontal displacements.

Crushing was observed immediately below and around the cone tip for all sands tested. After passage of the cone, the crushed particles form a thin, crushed particle band of thickness equal to about  $2.5D_{50}$  along the shaft, with a smaller percentage of crushed particles observed within an outer band with thickness equal to  $4D_{50}$ . It must be noted that the modelling of the crushing is difficult to achieve, as a specialized constitutive model is necessary. Phuong et al. (2014) has developed a modified hypoplasticity model to account for grain crushing. In this modified hypoplasticity model it is proposed to modify the reference void ratios, exponent  $\alpha$  and exponent  $\beta$  based on the stress level. It was not possible to implement this constitutive model in the simulations at this time. However, it is possible to identify the areas where grain crushing will occur.

From the DIC results, Arshad et al. (2014) determined the volumetric strains for several elements located at different radial distances during the penetration process and found that for a relative density of 45% the maximum change in volumetric strain for uncrushed sand was -6% and the maximum shear strain was -5%. For the test with a relative density of 82% the maximum change in volumetric strain was -15% and the maximum shear strain was -9%. This is shown in Figure 4.1, which also shows the location of the elements. These values are determined from Element D in both graphs. Arshad et al. (2014) noted that elements B and C must have undergone the critical state due to high shear strain with have been encountered in the experiments and a volume change is not expected after reaching critical state. Figures 4.2 and 4.3 show contour plots for all strains for the tests with a relative density

of 45% and 82% respectively. These contour plots were drawn after a penetration of  $20 \cdot r_c$ , where  $r_c = 0.0159\text{m}$  in the experiments.

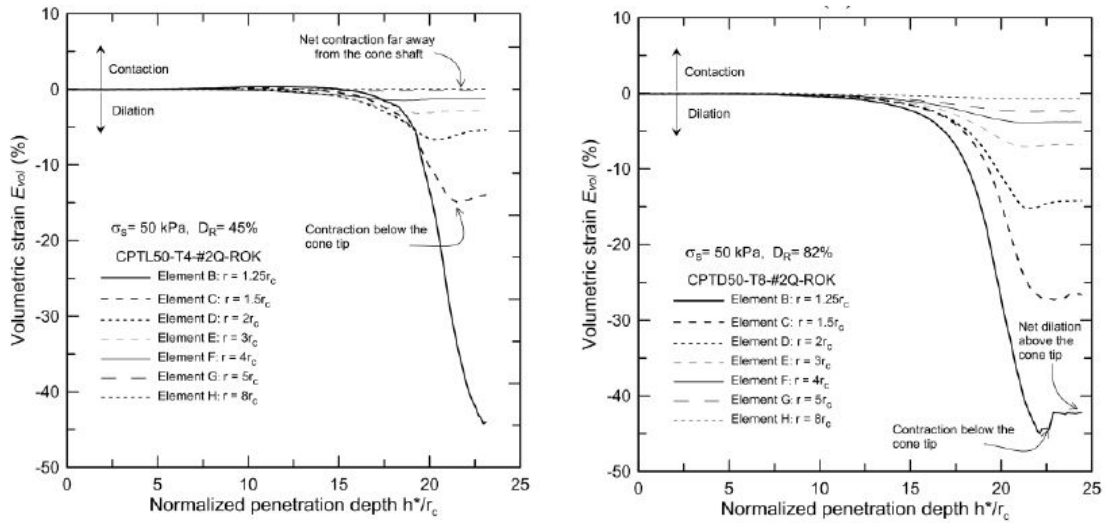


Figure 4.1: Volumetric strain development from DIC analysis by Arshad et al. (2014)

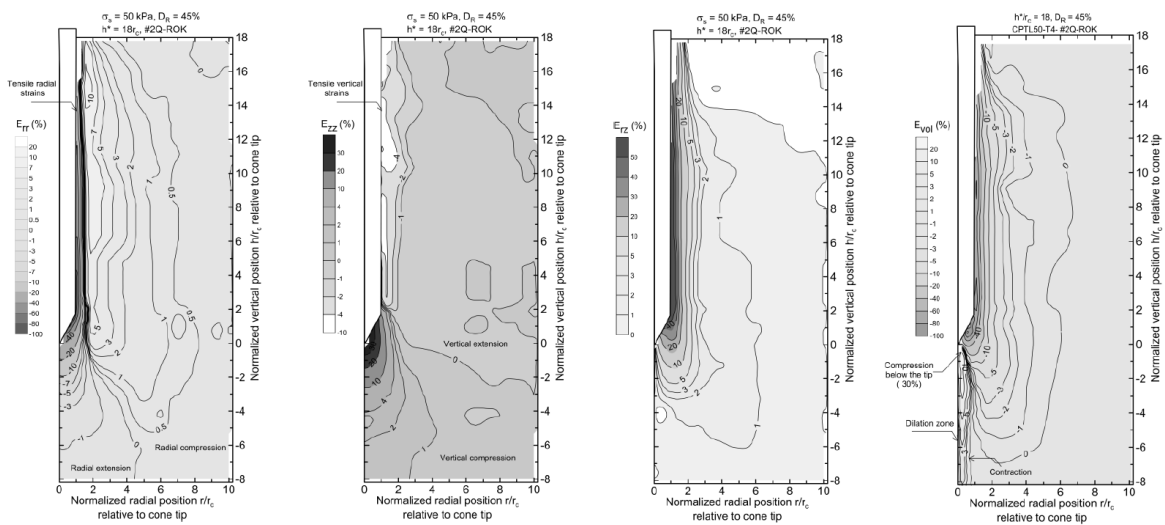


Figure 4.2: Strain contour plots of 45% relative density test (Arshad et al., 2014)

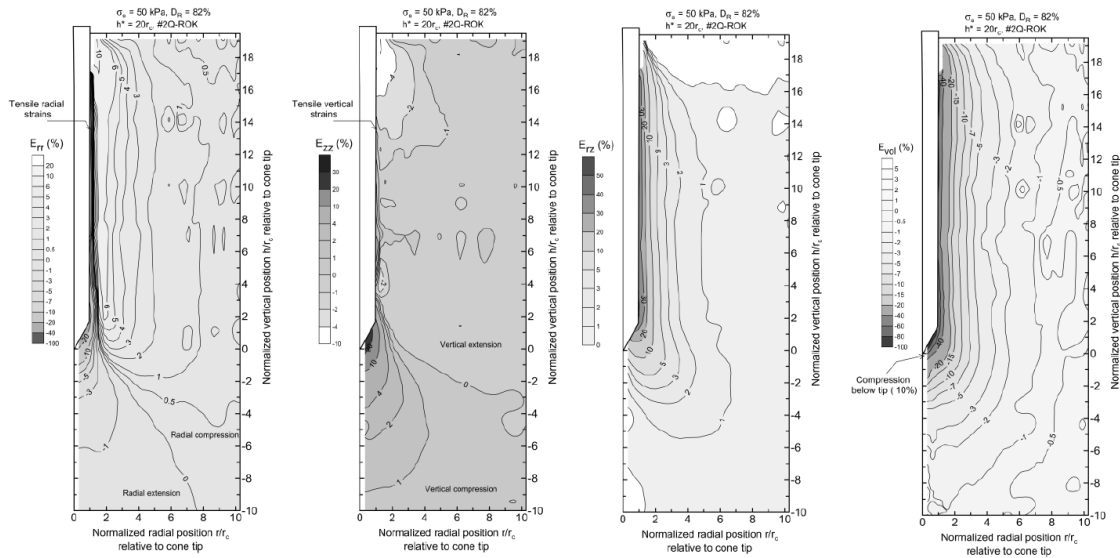


Figure 4.3: Strain contour plots of 82% relative density test (Arshad et al., 2014)

### 4.2.3 Empirical Correlations

Salgado & Prezzi (2007) proposed an equation to estimate  $q_c$  based on the critical friction angle (in degrees),  $\phi_c$ , and the relative density,  $D_R$  and is given in Equation 35

$$\frac{q_c}{p_A} = 1.64 \exp[0.1041\phi_c + (0.0264 - 0.0002\phi_c)D_R] \cdot \left(\frac{\sigma_h}{p_A}\right)^{0.841 - 0.0047D_R} \quad (35)$$

When comparing the data from Arshad et al. (2014) with the empirical relationship given in 35 we find that the correlation overestimates the cone resistance is all but one case, namely the test with  $D_R = 45\%$ . This is shown in Figure 4.4.

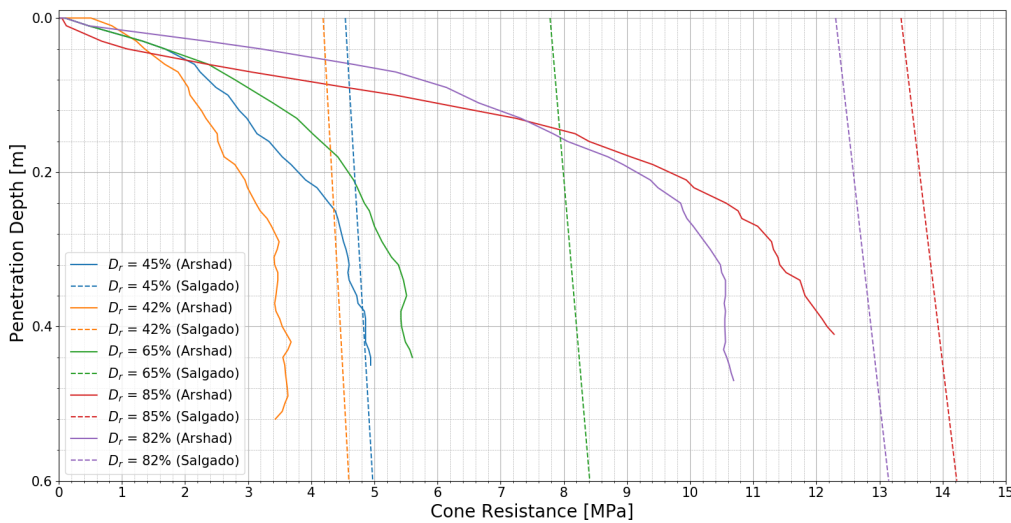


Figure 4.4: Comparison between experimental data (derived from Arshad et al. (2014)) and the empirical relationship by Salgado & Prezzi (2007)

### 4.3 Numerical Simulations

In order to validate the models, the parameters need to match the lab tests performed by Arshad et al. (2014). The only differences between the lab tests were in the relative density. A change in relative density results in a change in stiffness, peak friction angle and dilatancy angle. If soil particle were perfectly rigid and incompressible, the process of dilatancy would be purely driven by the density and arrangement of the particle structure. However, at higher pressures, particle crushing occurs reducing both the peak friction angle and the peak dilatancy angle (Bolton, 1986). In this section, the MPM models and their chosen parameters are discussed. Following that, the results alongside the comparison with the experimental data are shown.

#### 4.3.1 Model Series

Arshad et al. (2014) only reported the DIC data for the tests with  $D_R = 45\%$  and  $D_R = 82\%$ . Therefore the validation focused on those two models. Using the correlation by Bolton (1986) the model parameters were derived for the MPM models. This correlation allows for the estimation of the peak friction and dilatancy angle based on the relative density index:

$$I_R = D_R(10 - \ln p') - 1 \quad (36)$$

$$\phi'_{max} - \phi'_{res} = 0.8 \cdot \psi_{max} \quad (37)$$

$$\psi_{max} = \arctan\left(-\frac{d\varepsilon_v}{d\varepsilon_1}\right) = \arctan(0.3 \cdot I_R) \quad (38)$$

$I_R$  is the relative dilatancy index and  $p'$  is the mean effective stress at failure. The value for mean effective stress is determined from a MPM model at 0.5m depth as this is the value halfway of the shaft. The mean effective stress at this depth is 300 kPa. The shear modulus is determined using the conversion formula for homogenous isotropic linear elastic material,  $G = \frac{E}{2 \cdot (1 + \nu)}$ , where the Young's modulus,  $E$ , is assumed to be 20 MPa for a loose sand and 65 MPa for a dense sand (Obrzud & Truty, 2012). A small value for the cohesion is used for numerical stability. The model parameters are given in Table 4.2.

**Table 4.2:** Input parameters MPM models

Parameter		$D_R = 45\%$	$D_R = 82\%$
Shear Modulus	$G$	8.33 MPa	27 MPa
Poisson's Ratio	$\nu$	0.2	0.2
Peak Cohesion	$c'_{max}$	0.1 kPa	0.1 kPa
Residual Cohesion	$c'_{res}$	0.1 kPa	0.1 kPa
Peak Friction Angle	$\phi'_{max}$	37.7°	63.0°
Residual Friction Angle	$\phi'_{res}$	32.2°	32.2°
Peak Dilatancy Angle	$\psi_{max}$	7.0°	38.5°
Residual Dilatancy Angle	$\psi_{res}$	0°	0°
Shape Factor	$\eta$	50	50

#### 4.3.2 Results

Figure 4.5 shows the cone resistance profiles for the MPM models, the experimental data and the empirical relationship combined. While the MPM model for  $D_R = 45\%$  shows reasonable agreement with the experimental data in terms of steady state cone resistance, we can observe a large disagreement in the  $D_R = 82\%$  MPM model and the experimental data. The MPM model overestimates the cone resistance by roughly 40% and shows a very unstable cone resistance profile. Furthermore, the initial 0.25m of penetration differs significantly for both cases. Since the  $D_R = 82\%$  MPM model differs

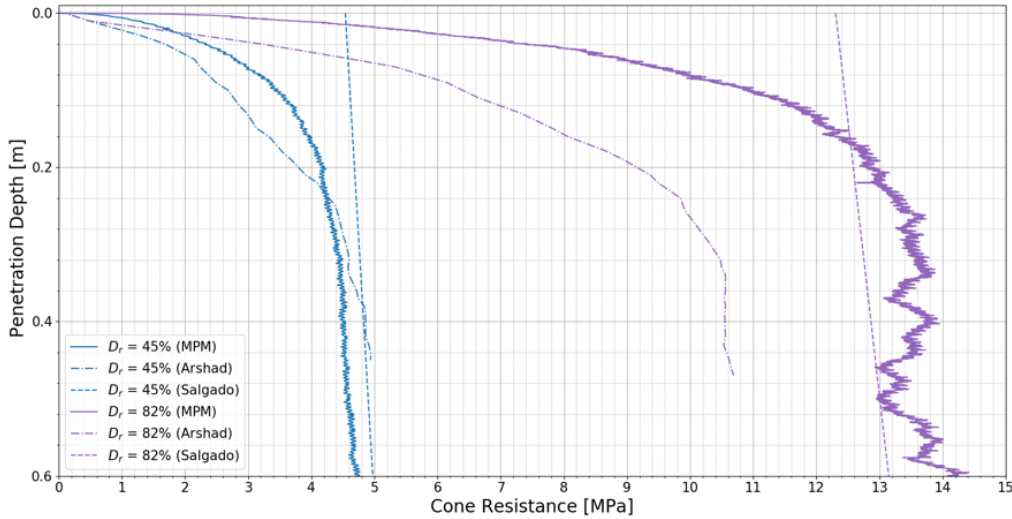


**Figure 4.5:** Comparison between the MPM models, the experimental data and the empirical relationship

significantly and it shows a very unstable cone resistance profile, a further comparison is omitted. Instead only the  $D_R = 45\%$  case will be compared in terms of strains.

The strain contour plots were created after a penetration of  $20 \cdot r_c$ . In the MPM model that would be equal to a penetration of 0.437m. Since the chosen penetration per time step was 0.02m, the strain contour plots shown are after 0.44m of penetration. Figures 4.6 through 4.9 show the comparison of the contour plots between the MPM model and the experiments. The strains from the MPM model are obtained from the strain matrix and the number indicates the location in the strain matrix which is given in Equation 39. For example, strain 0 would be  $\varepsilon_{rr}$  and strain 1 would be  $\varepsilon_{rz}$ .

$$\underline{\underline{\varepsilon}} = \begin{bmatrix} \varepsilon_{rr} & \varepsilon_{rz} & \varepsilon_{r\theta} \\ \varepsilon_{zr} & \varepsilon_{zz} & \varepsilon_{z\theta} \\ \varepsilon_{\theta r} & \varepsilon_{\theta z} & \varepsilon_{\theta\theta} \end{bmatrix} \quad (39)$$

It must be noted that the sign convention for the MPM model and the experiments is different. In the MPM model, extension is positive and contraction negative while in the experiments extension is negative and compression positive. By comparing the strains obtained from the model and those reported by Arshad et al. (2014) we can see that qualitatively the behaviour of the soil is the same as the same zones of both compression and extension can be identified. The experimental maximum volumetric and shear strains were -6% and -5% respectively. From the MPM model the maximum values were -4% for the volumetric strain which is in reasonable agreement. However the maximum shear strain from the MPM model was -10.7% which is a factor 2 difference. The location of the maximum shear strains was along the cone shaft. It could be the case that the friction angle between the cone and the sand for the MPM model was different than that from the calibration chamber tests. In the MPM models it was assumed that the friction angle between the soil and the structure was  $\frac{2}{3}\phi'_{res}$ .

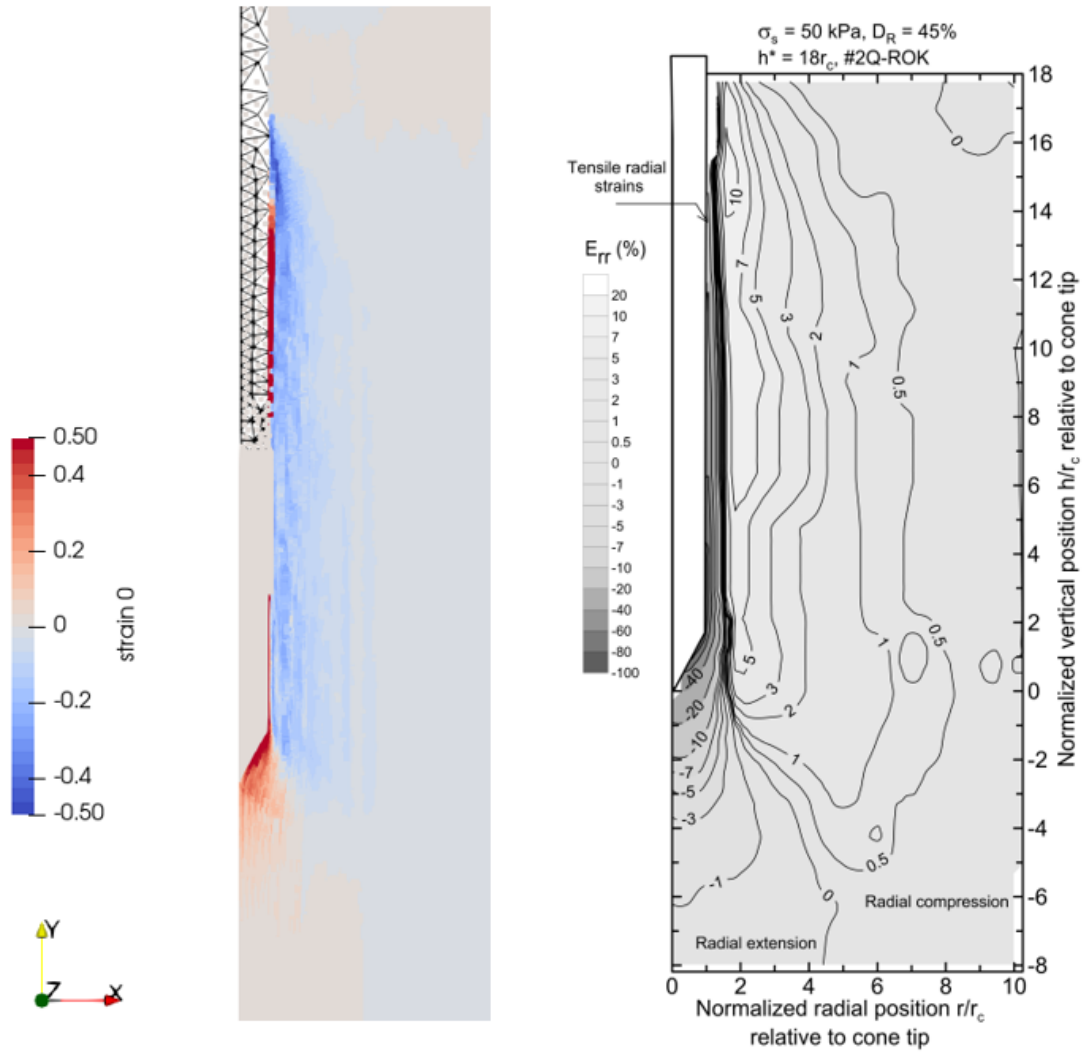


Figure 4.6: Comparison of contour plots of  $\epsilon_{rr}$

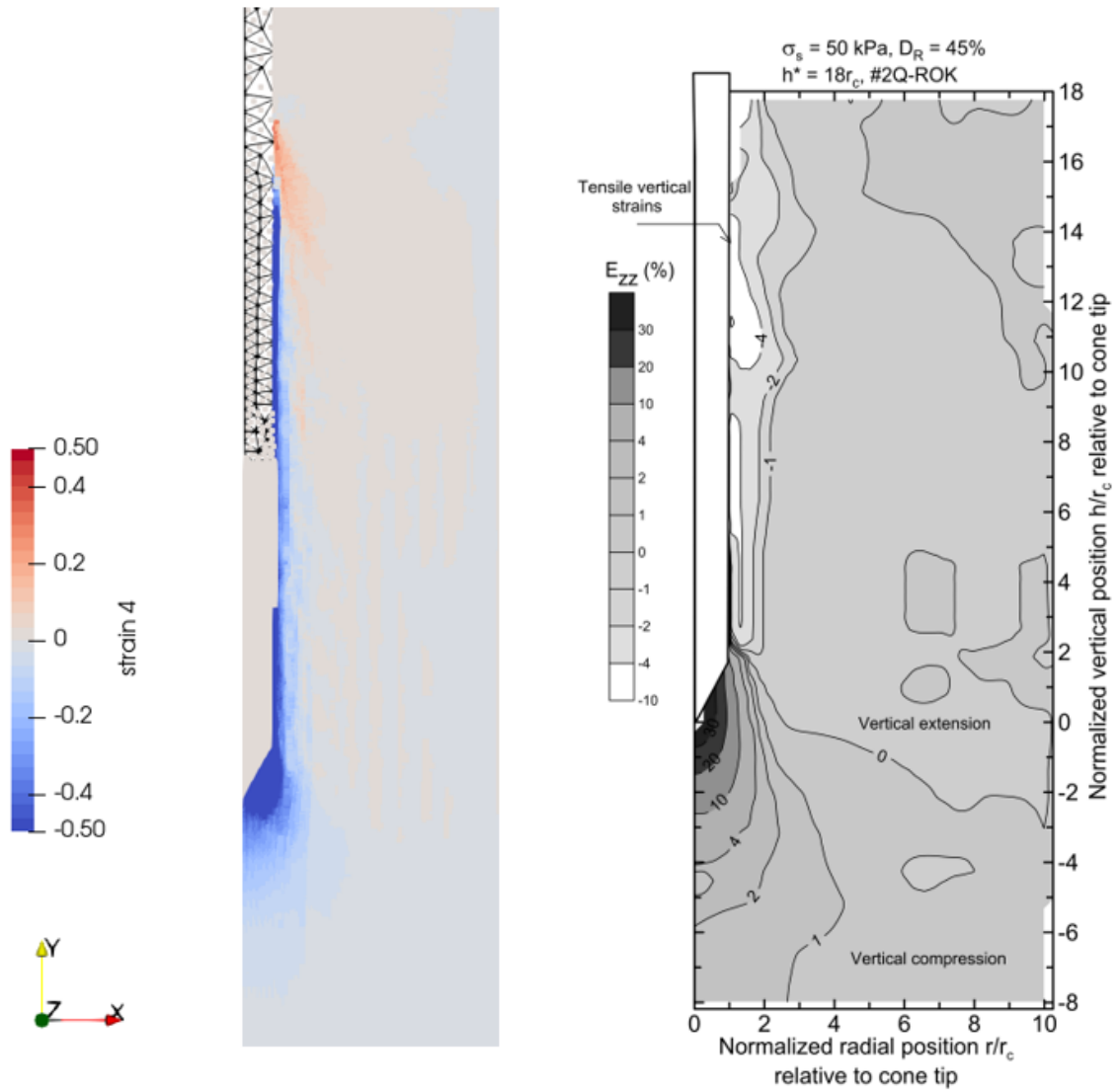


Figure 4.7: Comparison of contour plots of  $\varepsilon_{zz}$

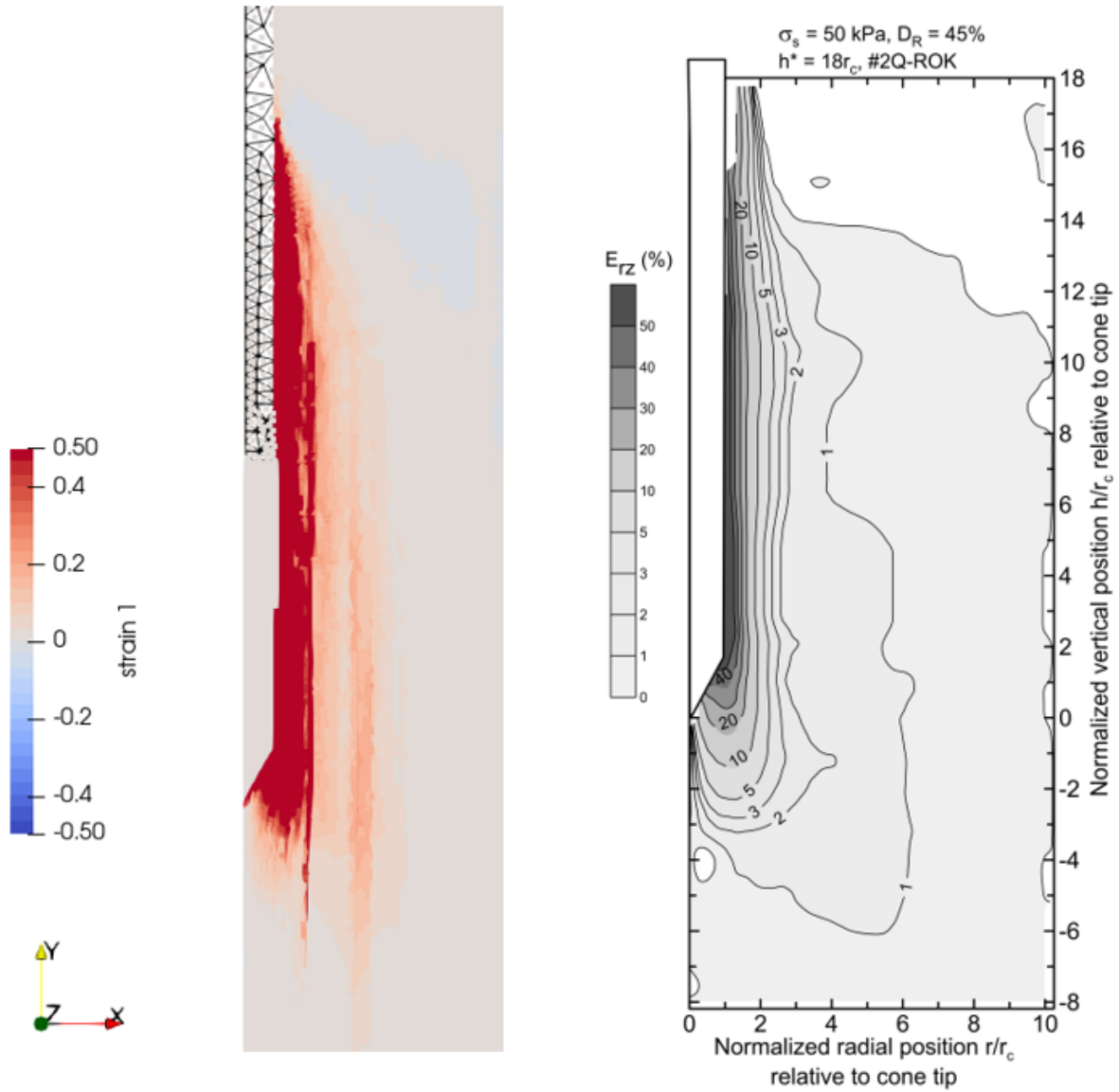


Figure 4.8: Comparison of contour plots of  $\epsilon_{rz}$

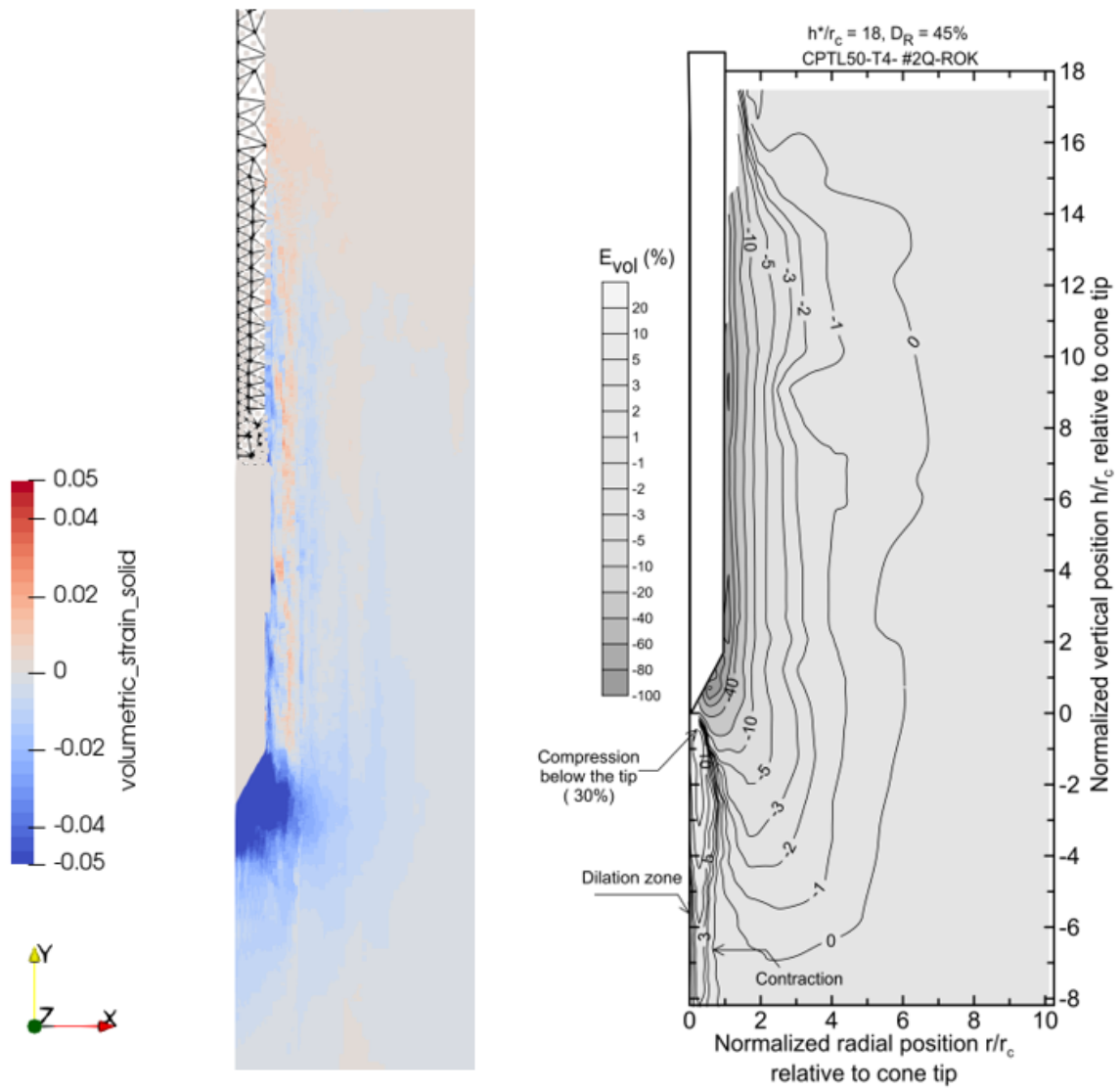
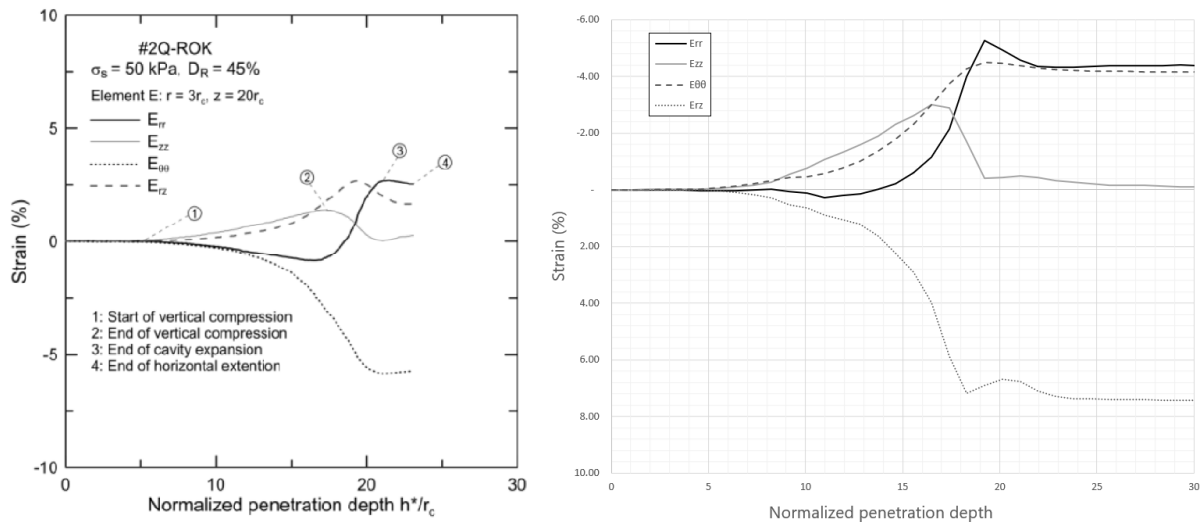


Figure 4.9: Comparison of contour plots of  $\varepsilon_{vol}$

In addition to the comparison of the contour plots, the strain paths for specific elements were also compared. In total the strain paths of four elements were investigated. These elements, named B, C, D, and E, were located at a depth of  $z = 20 \cdot r_c$  and a radial distance of  $r = 1.25 \cdot r_c, 1.5 \cdot r_c, 2.0 \cdot r_c$  and  $3.0 \cdot r_c$ . Figure 4.10 shows the comparison for element E at a radial distance of  $3.0 \cdot r_c$ . Again, the sign convention is reversed for the MPM and the experimental data. This is why the values of the y-axis in the right graph are reversed. In this comparison it was found again that the qualitative behaviour can be seen where the different phases of the installation process can be distinguished. The accumulated strains were not in agreement as differences with a factor 2 were found. The most likely explanation is that in the MPM model, the stiffness is not accurately captured as this the stiffness is constant and independent of stress in the MCSS constitutive model where in reality the stiffness is in fact not constant and stress-dependent.

Figure 4.11 shows the comparison for element B at a radial distance of  $1.25 \cdot r_c$ . Here we see the only qualitative disagreement found in the comparison of the strain paths. The MPM model predicts radial compression where the experiments showed radial extension. Also, the quantitative difference of the tangential strains between the MPM model and the experiments is much more present. A possible explanation for both discrepancies could be that in the experiments by Arshad et al. (2014) significant grain crushing occurred near the cone at the location of element B but since grain crushing is not accounted for in the used constitutive model, this can not be confirmed or denied. Appendix D shows the comparison for all elements.



**Figure 4.10:** Strain paths comparison for element E. Left: experiments; Right: MPM model

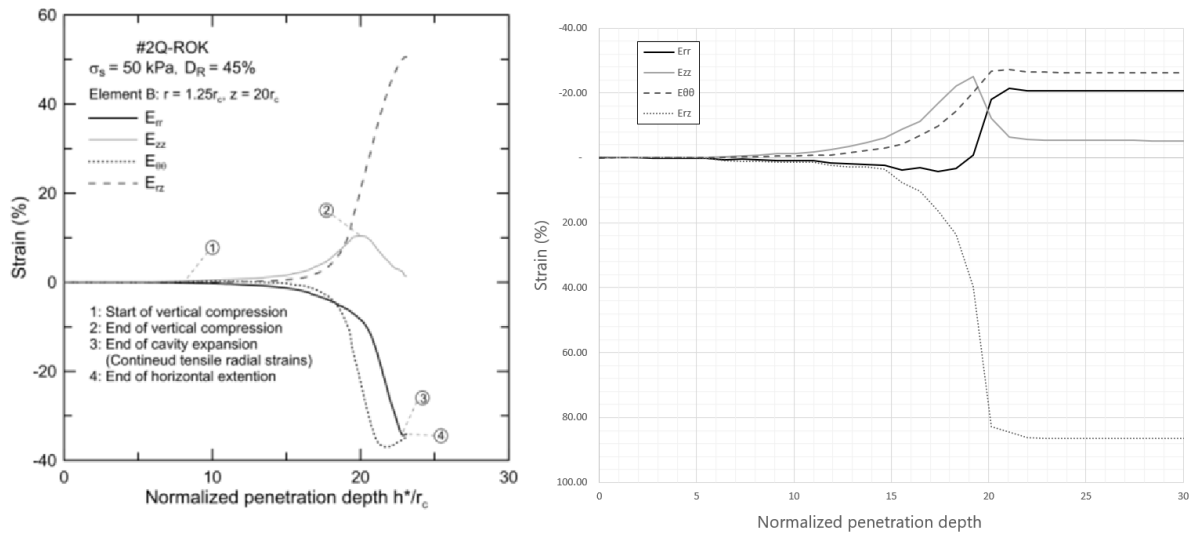


**Figure 4.11:** Strain paths comparison for element B. Left: experiments; Right: MPM model

#### 4.4 Conclusion

This chapter showed the validation process of the presented model. The validation has been done by comparing it to experimental data from half circular calibration chamber tests performed by Arshad et al. (2014). These calibration chamber tests differed from each other in terms of relative density which ranged from 45% to 85%. In addition, image-based data from this series of laboratory tests was used to investigate the strain development. The experimental data was also compared to an empirical relationship by Salgado & Prezzi (2007) which allows for an estimation of the cone resistance based on the relative density.

From the comparison between the MPM models and the experimental data it became clear that the cone resistance of the MPM models were not in agreement with the experimental data which could be attributed to errors in the soil stiffness. While the MPM model which was created to simulate the loosest test ( $D_R = 45\%$ ) was in reasonable agreement, the MPM model which was supposed to represent the densest soil ( $D_R = 85\%$ ) overestimated the cone resistance by 40%. One possible reason could be the fact that the shear modulus is kept constant in the used constitutive model. The fact that the stiffness is kept constant throughout the simulation is a limitation of the used constitutive model.

When investigating the similarities between the MPM model and the experimental data for the  $D_R = 45\%$  case, it was found the qualitative behaviour of the strains were in agreement. It was found that the same zones of compression and extension could be identified. Quantitatively speaking, differences were found in the accumulated strains and strain paths which could be attributed to a lack of information captured in the used constitutive model or an erroneous determination of the model parameters.

# Chapter 5

## Sensitivity Analysis

### 5.1 Introduction

In order to get a better understanding of the installation effects encountered with the cone penetration process, a sensitivity analysis has been conducted. The installation effects we are aiming to model are the plastic radius of the soil after the installation. The modelling of the particle crushing is not possible with the current constitutive model. Therefore, this analysis focuses on the plastic radius and the cone resistance profile and how they vary due to a change in parameters. The sensitivity analysis is performed using the MC Strain Softening model. The input parameters are listed in Table 5.1. This table also included the chosen values for the base case. The values for the peak and residual friction angle and dilatancy angle were determined using the correlations by Bolton (1986) for a sand with a relative density of 45%. The correlations are given in Equation 37. The shear modulus is determined using the conversion formula for homogenous isotropic linear elastic material,  $G = \frac{E}{2 \cdot (1 + \nu)}$ , with the Young's modulus,  $E$ , is assumed to be 20 MPa for a loose sand (Obrzud & Truty, 2012). As mentioned in Subsection 4.2.1 the residual (or critical state) friction angle is determined to be  $32.2^\circ$  by Arshad et al. (2014) from direct shear tests.

**Table 5.1:** Input parameters MC Strain Softening model

Parameter		Values base case
Shear Modulus	$G$	8.33 MPa
Poisson's Ratio	$\nu$	0.2
Peak Cohesion	$c'_{max}$	0.1 kPa
Residual Cohesion	$c'_{res}$	0.1 kPa
Peak Friction Angle	$\phi'_{max}$	$37.7^\circ$
Residual Friction Angle	$\phi'_{res}$	$32.2^\circ$
Peak Dilatancy Angle	$\psi_{max}$	$7^\circ$
Residual Dilatancy Angle	$\psi_{res}$	$0^\circ$
Shape Factor	$\eta$	50

The parameters which are varied are  $G$ ,  $\phi'_{max}$ ,  $\psi_{max}$  and  $\eta$ . Each parameter is changed both higher and lower in two steps compared to the base case value. Physically speaking,  $\phi'_{max}$  and  $\psi_{max}$  are connected to each other but are initially disconnected in order to find the sensitivity to each individual parameter. However, the combination of  $\phi'_{max}$  and  $\psi_{max}$  is also varied together to incorporate this physical aspect. The values for the parameters are summarized in Table 5.2. These parameters and their influence on the cone resistance are discussed in the next section. Following that, the influence on the plastic radius is discussed. Lastly the conclusions are drawn.

**Table 5.2:** Input parameters for sensitivity analysis

Parameter	--	-	Base	+	++
$G$ [MPa]	4.17	6.25	8.33	10.42	12.50
$\phi'_{max}$ [°]	32.2	35.0	37.7	40.5	43.3
$\psi_{max}$ [°]	0.0	3.5	7.0	10.5	14.0
$\phi'_{max}$ & $\psi_{max}$ [°]	32.2 & 0.0	35.0 & 3.5	37.7 & 7.0	40.5 & 10.5	43.3 & 14.0
$\eta$ [-]	25	37.5	50	62.5	75

## 5.2 Parameter Sensitivity of the Cone Resistance

This section discusses the influence of the variation of the parameters on the cone resistance. The different variation is discussed in the following subsections.

### 5.2.1 Variation of the Shear Modulus $G$

The shear modulus gives the relationship between the deviatoric stresses and deviatoric strains. For this sensitivity analysis the values for the shear modulus are determined from the range of possible Young's modulus values for a loose sand with an equal interval between the values. These values range from 10 MPa to 30MPa (Obrzud & Truty, 2012). Using the conversion formula given in the previous section the set of shear modulus values is: 4.17 MPa, 6.25 MPa, 8.33 MPa, 10.42 MPa and 12.50 MPa. Figure 5.1 gives the cone resistance profiles for the different shear moduli. From this Figure we can observe that the numerical oscillations are heavily influenced by the shear modulus where a higher shear modulus results in a higher frequency and amplitude. This can be seen in Figure 5.2 where parts of the cone resistance profile for the lowest and highest shear modulus (4.17 MPa and 12.50 MPa resp.) are shown together.

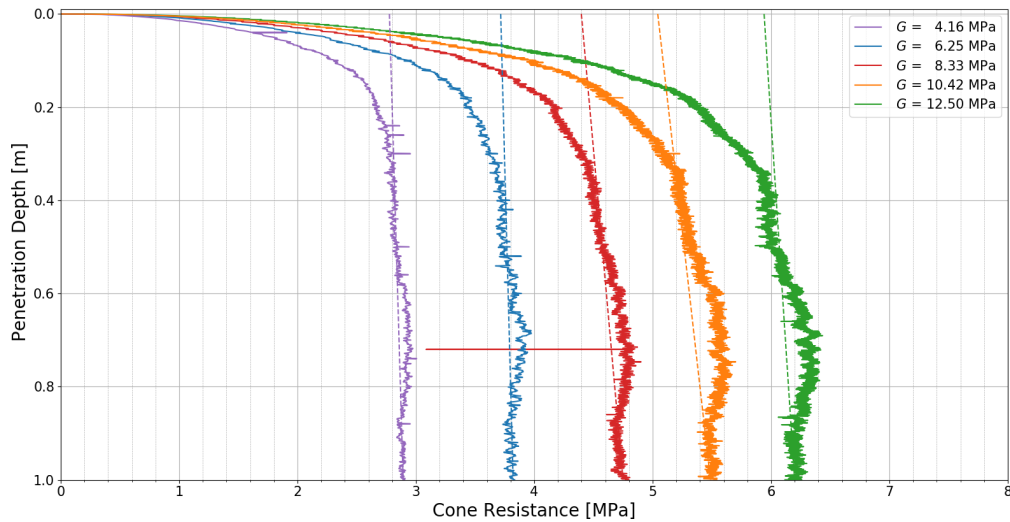


**Figure 5.1:** Cone resistance profiles for different shear moduli

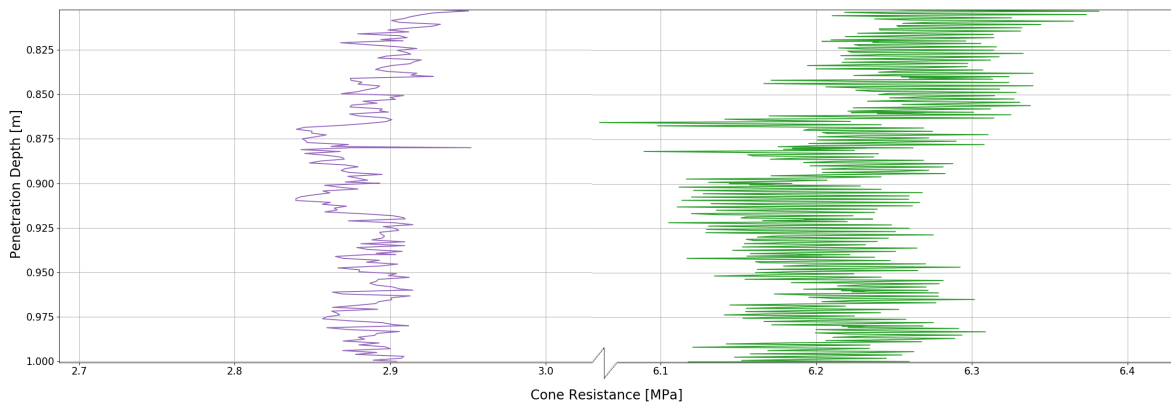


**Figure 5.2:** Oscillations for lowest and highest shear modulus

Given the oscillations in the cone resistance profile which are the result from the numerical calculations, using the tangent to determine the gradient of the steady state cone resistance is not possible. Instead, the mean value of data clusters of 15 data points is calculated and the secant line between (1) The first location where the difference between the mean values of two subsequent data clusters is less than 0.05% and (2) the mean value of the final data cluster. Figure 5.3 shows the secant lines of the steady state cone resistance. From Figure 5.3 we can observe that all cone resistance profile seem to experience a secondary increase in cone resistance before coming back to the steady state value. This bulge in the cone resistance profile which was also observed in Section 3.6 and seems to be bigger for a stiffer soil. After an investigation into this phenomenon which happens after  $\sim 0.55\text{m}$  penetration, no abnormalities were found in the simulation. The steady state cone resistance for the different shear moduli are given in Table 5.3. We can observe that the soil stiffness and the resulting cone resistance have a positive relationship which is to be expected given that a stiffer soil would require more force to penetrate.

**Table 5.3:** Steady state cone resistance for different shear moduli

Shear modulus [MPa]	Difference	Cone resistance [MPa]	Difference
4.16	-50%	2.89	-39.2%
6.25	-25%	3.82	-19.6%
8.33	-	4.75	-
10.42	+25%	5.49	+15.6%
12.50	+50%	6.2	+30.5%

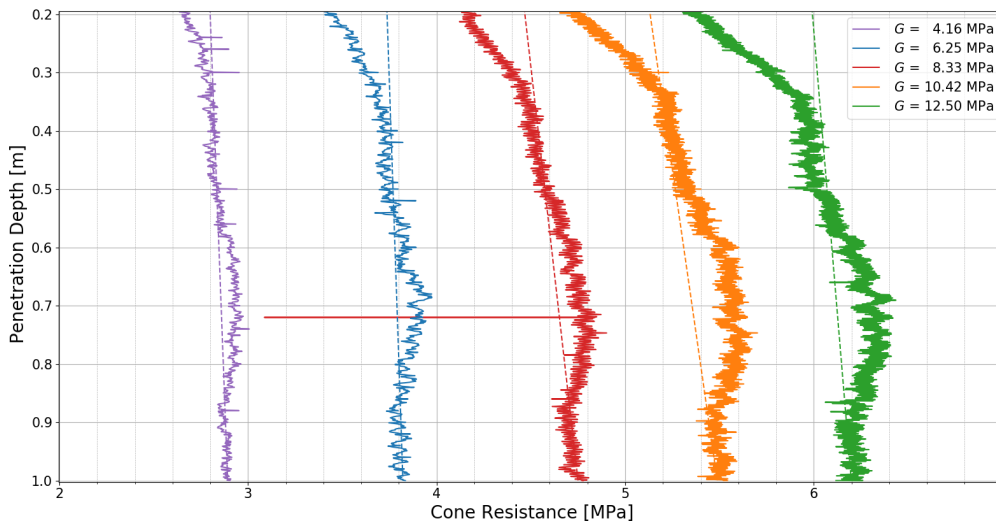


**Figure 5.3:** Steady state cone resistance for different shear moduli

### 5.2.2 Variation of the Peak Friction Angle $\phi'_{max}$

The peak friction angle has been varied with the following values:  $32.2^\circ$ ,  $35.0^\circ$ ,  $37.7^\circ$ ,  $40.5^\circ$  and  $43.3^\circ$ . This range of values was chosen with the lowest value for the peak friction angle being equal to the residual friction angle and adding one value in between the lowest and base value and continuing these steps to get the highest value of  $43.3^\circ$ . Figure 5.4 shows the cone resistance profiles for these values. It can be observed that the peak friction angle has little influence on the resulting cone resistance with the cone resistance ranging from 4.56 MPa to 4.97 MPa for a peak friction angle of  $32.2^\circ$  and

43.3° respectively. However, the simulation seems more stable for a lower value of the peak friction angle. However, the bulge which has also been observed is also present in these graphs and the magnitude of the increase in cone resistance seems to be equal for all values of peak friction angle.

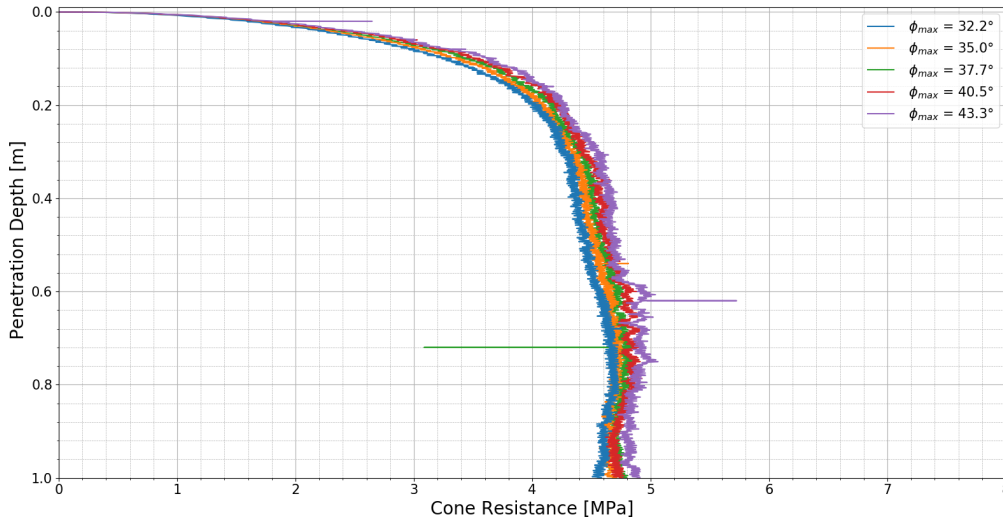


**Figure 5.4:** Cone resistance profile for different peak friction angles

### 5.2.3 Variation of the Peak Dilatancy Angle $\psi_{max}$

The dilatancy angle is a measure of the possible volume change of a soil subjected to shear strains. The dilatancy angle is a function of soil density and stress level. In the critical soil state theory, when a soil is in critical state no additional volumetric strains will occur when the soil is subjected to additional stresses and thus, the residual dilatancy angle is 0°. As mentioned before the dilatancy angle is a function of the soil density where a denser soil will dilate more than a loosely packed soil. This is due to the fact that sand particles need to override each other before a critical state is reached, assuming that the particles do not crush before this happens. The variation of the peak dilatancy angle has been conducted in a similar manner as the peak friction angle. The lowest value is the same as the residual dilatancy angle, in this case 0°, and the increment size is kept constant. Therefore, the values for the peak dilatancy angles are 0°, 3.5°, 7.0°, 10.5° and 14.0°. Figure 5.5 shows the cone resistance profiles for the various peak dilatancy angles. The peak dilatancy angle and the cone resistance have a positive relationship. The influence on the cone resistance is larger compared to the peak friction angle. Also the bulge which has been observed so far seems to be greatly influenced by the peak dilatancy angle and, while it does not disappear completely, the deviation from the steady state cone resistance is significantly less for lower values of  $\psi_{max}$  which can be seen in Figure 5.6.

### 5.2.4 Variation of $\phi'_{max}$ and $\psi_{max}$ combined

In the previous two sections, the parameters  $\phi'_{max}$  and  $\psi_{max}$  have been varied separately in order to investigate their influence on the numerical predictions. However, these two parameters are physically linked to each other. It is therefore obvious to also investigate the influence of both parameters combined on the cone resistance profile. The relation given by Bolton (1986),  $\phi' = \phi'_{res} + 0.8 \cdot \psi$ , serves as a guide to determine the values for both  $\phi'_{max}$  and  $\psi_{max}$  which coincide with the values used in the variation of both parameters individually. The values used were:

- $\phi'_{max} = 32.2^\circ$  &  $\psi_{max} = 0^\circ$
- $\phi'_{max} = 35.0^\circ$  &  $\psi_{max} = 3.5^\circ$

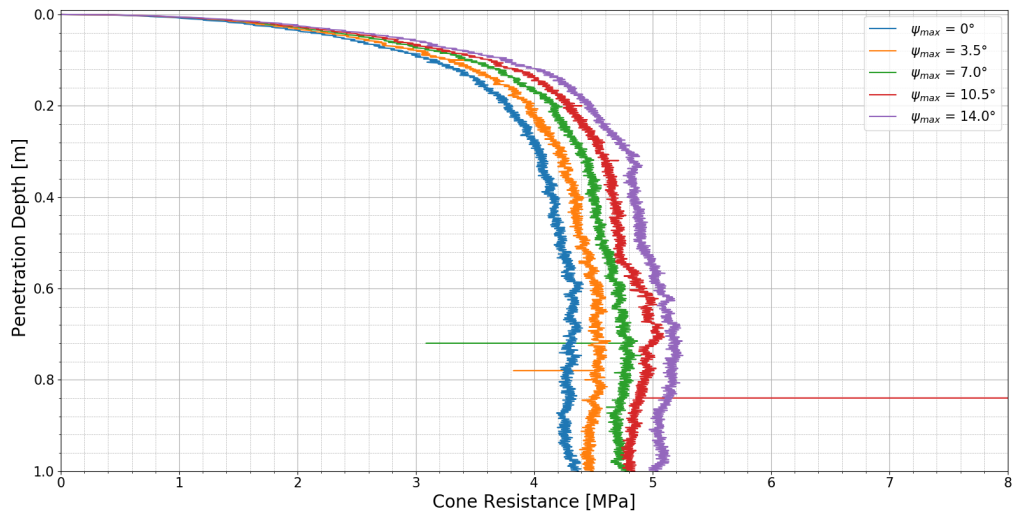


**Figure 5.5:** Cone resistance profile for different peak dilatancy angles

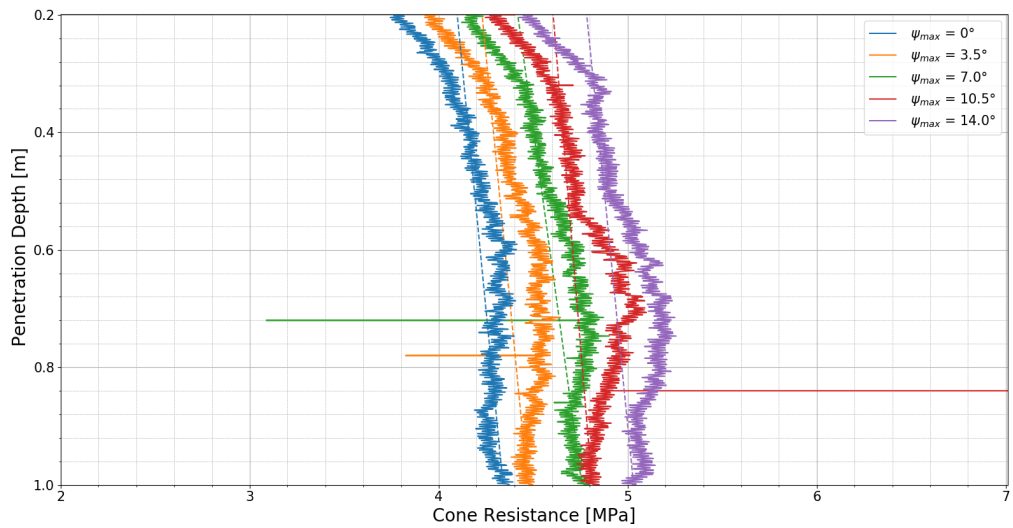


**Figure 5.6:** Steady state cone resistance for different peak dilatancy angles

- $\phi'_{max} = 37.7^\circ$  &  $\psi_{max} = 7.0^\circ$
- $\phi'_{max} = 40.5^\circ$  &  $\psi_{max} = 10.5^\circ$
- $\phi'_{max} = 43.3^\circ$  &  $\psi_{max} = 14.0^\circ$

Figure 5.7 shows the cone resistance profiles for this variation set. The first thing that can be observed is the difference in stability for the different variations. Where the model without any softening ( $\phi'_{max} = \phi'_{res} = 32.2^\circ$  &  $\psi'_{max} = \psi'_{res} = 0^\circ$ ) shows a clear steady state penetration, the models with softening show an increasingly present bulge in the cone resistance profile. In terms of cone resistance we can observe that a higher  $\phi'_{max}$  and  $\psi'_{max}$  increases the cone resistance which is to be expected since the soil should behave stronger.

From this variation we can conclude that the observed second increase in the cone resistance is the result of the combination of the used calculation method MPM-Mixed and the use of strain softening. Section 3.6 showed that using strain softening without the MPM-Mixed mitigated the bulge as well as this section which showed that no strain softening with the MPM-Mixed did the same.

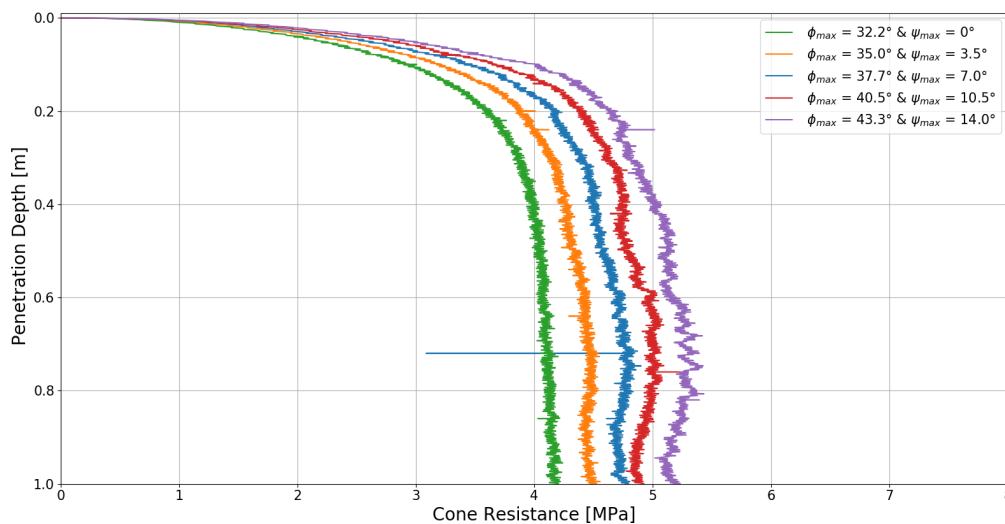


**Figure 5.7:** Cone resistance profile for different peak friction and dilatancy angles

### 5.2.5 Variation of the Shape Factor $\eta$

The shape factor  $\eta$  influences the rate of strain softening during the simulation, as shown in Equation 34. Where a higher shape factor results in a higher rate of softening. This is illustrated in Figure 3.18. The chosen shape factors are 25, 37.5, 50, 62.5 and 75. Figure 5.8 shows the resulting cone resistance profiles. From the graphs we can observe the exponential nature of the strain softening equation as the linear increase in the shape factor does not result in a linear decrease in the soil stiffness but rather an exponential one.

### 5.2.6 Summary of Parameter Sensitivity of Cone Resistance

This section provides a summary of the parameter sensitivity of the model. One of the best methods to illustrate the sensitivity to the parameter is by using a tornado plot. In this type of plot we can compare the relative importance of each parameter. Figure 5.10 shows the tornado plot for the cone resistance. We can observe that the shear modulus has the most influence on the cone resistance. This is to be expected since the cone resistance should be higher for a stiffer soil.

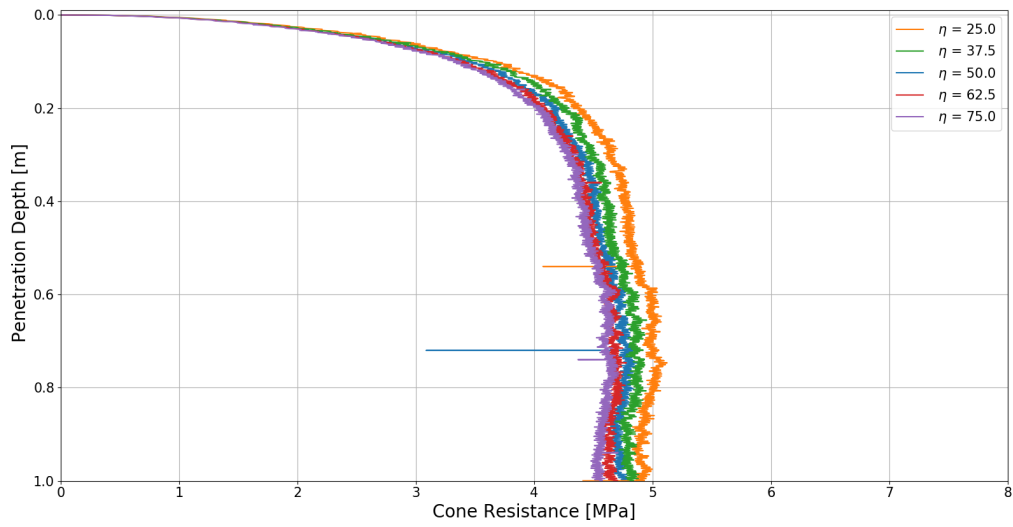


**Figure 5.8:** Cone resistance profile for different shape factors

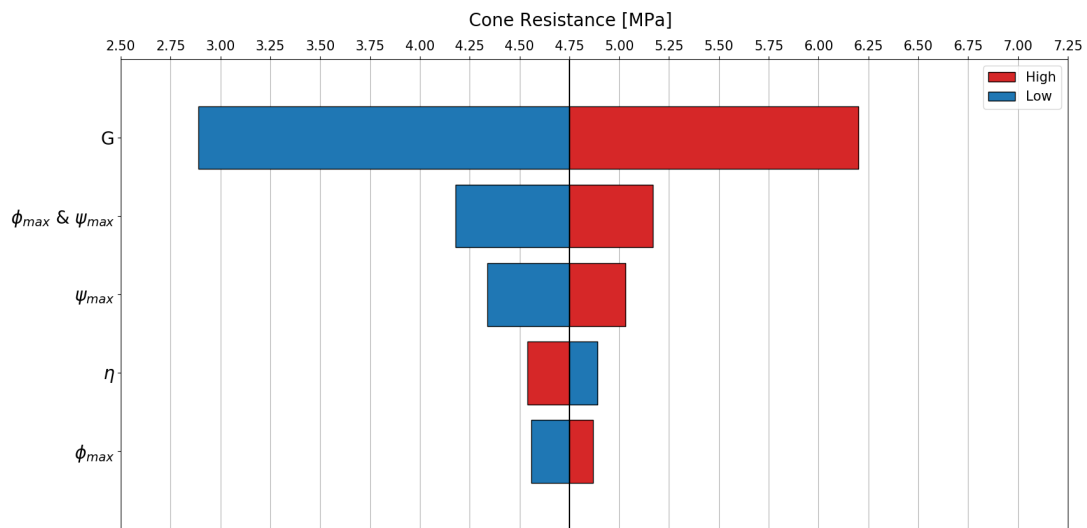


**Figure 5.9:** Tornado plot of parameter sensitivity of the cone resistance

### 5.3 Parameter Sensitivity of the Plastic Radius

For the influence of the plastic radius, shown in Figure 5.10, we can see a different pattern. The plastic radius was determined using the described methodology (Section 3.7). The shear modulus again has the most influence but in the case of the plastic radius, the friction angle has a much larger influence compared to the influence on the cone resistance. A higher friction angle does however result in a lower plastic radius which can be expected since a higher friction angle results in a higher failure criterion and the soil yielding less easily. The influence of the peak dilatancy angle is less present but reversed compared to the peak friction angle. This is why the combined influence of both the peak friction and dilatancy angle is even less since both parameters counteract each other. There is no effect of the shape factor which is obvious since the shape factor is only used after the soil experiences plasticity and therefore does not influence the plastic radius.

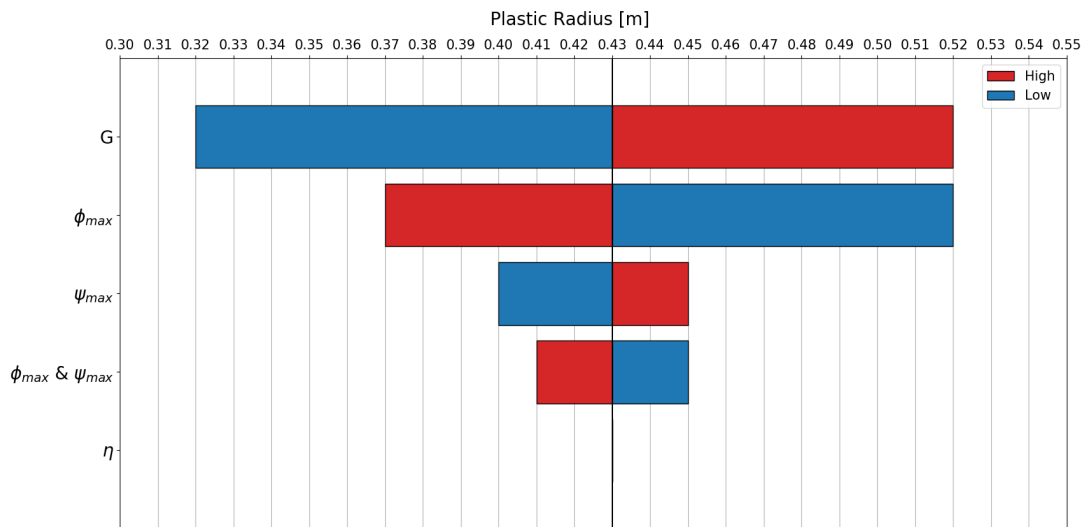


**Figure 5.10:** Tornado plot of parameter sensitivity of the plastic radius

When compared to the analytically determined plastic radius using the solution by Baguelin et al. (1978), it was found that the analytical solution overestimates the plastic radius by an average of 18%. However for the cases where the peak friction angle tends towards the residual friction angle we find the most agreement between the analytical solution and the obtained plastic radius from the model, namely only 1%. Figure 5.11 show the stresses over radial distance together with the Mohr circle at the plastic radius. In this specific model, the peak and residual friction angle were equal and the rest of the parameters were the same as the base case given in Table 5.1. The vertical dotted line shows the plastic radius which is determined from the analytical solution.

The largest difference was found in the model with the highest peak friction angle of  $43.3^\circ$  which was an overestimation of 33%. Figure 5.12 shows the stresses over radial distance together with the Mohr circle for this model. The tangential stress shows a more prominent dip in this model compared to the other model. The difference can be explained by the fact that the analytical solution of Baguelin does not take into account any softening behaviour and dilatancy of the soil which influence the development of stresses.

The magnitude of the overestimation is visualized in Figure 5.13. We see that the peak friction angle has the most influence on an erroneous estimation of the plastic radius. This means that for values of  $\phi'$  closer to  $\phi'_{res}$  the prediction is more accurate. This is reflected in the influence of the shape factor

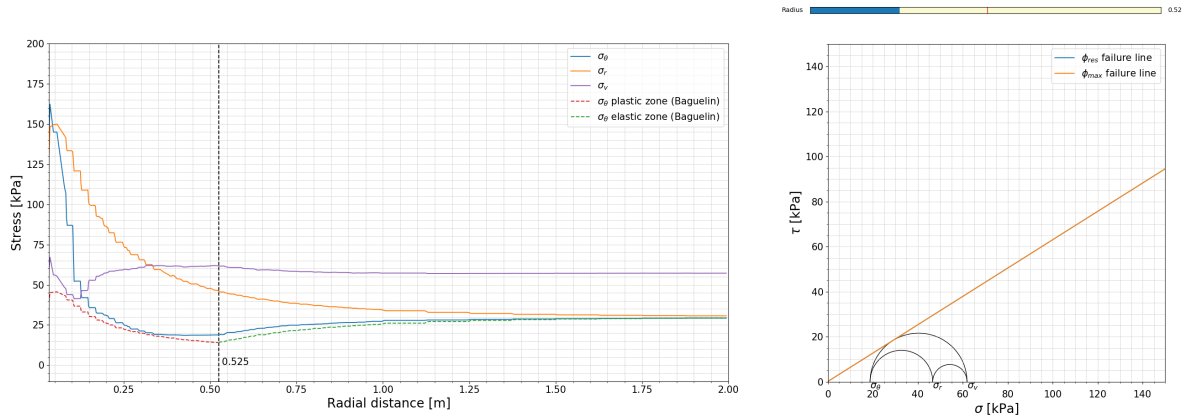


Figure 5.11: Stress state over radial distance including the Mohr circle at plastic radius

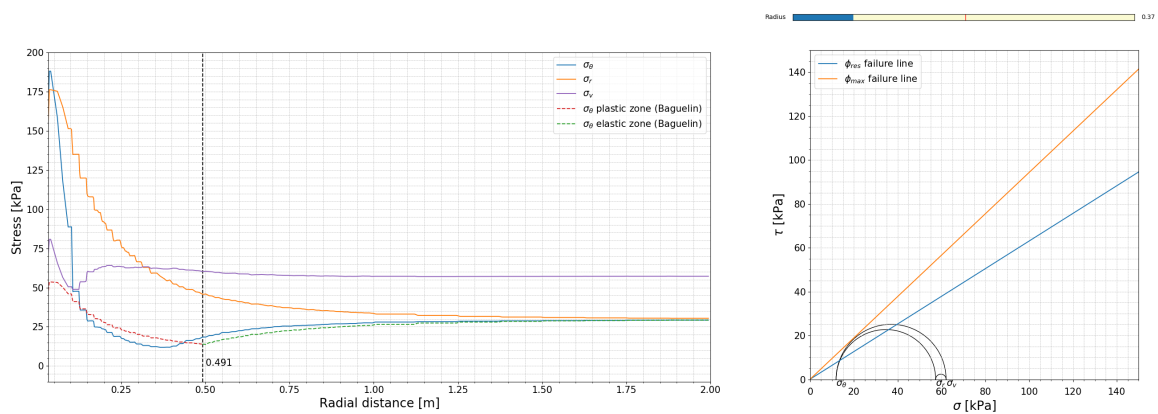
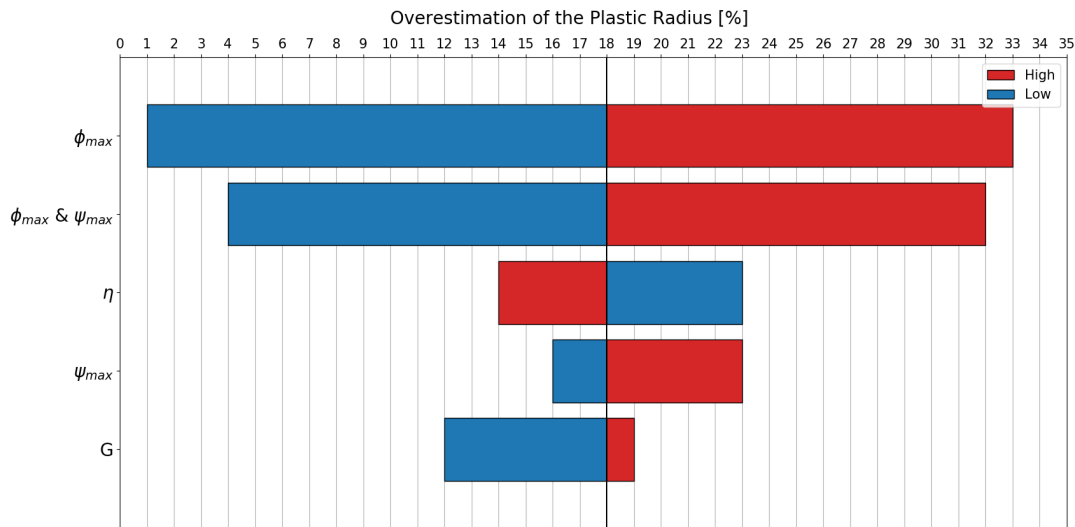


Figure 5.12: Stress state over radial distance including the Mohr circle at plastic radius

since a higher shape factor results in a higher softening rate and thus  $\phi'_{res}$  is reached quicker and a better estimation.



**Figure 5.13:** Tornado plot of the overestimation of the plastic radius

## 5.4 Conclusion

In this chapter the sensitivity analysis has been conducted to investigate both the influence of the different parameters and the robustness of the simulation. It was found that all parameters influenced the final result in the expected manner. The shear modulus had by far the most influence on both the cone resistance and the plastic radius.

It was also found that the analytical solution of Baguelin does predict the plastic radius reasonably well for the situation which it is derived, namely a frictional and cohesive soil. When other aspects of the soil come into play, like dilatancy, the analytical solution overestimates the plastic radius. Nevertheless, the analytical solution by Baguelin can serve as an upper boundary to determine the plastic radius.

Lastly it was found that the combination of the MPM-Mixed calculation method and the use of the strain softening resulted in a less accurate numerical prediction.

# Chapter 6

## Conclusions & Recommendations

### 6.1 Conclusions

The objective of this research was to investigate the feasibility of modelling the installation process of a cone penetration test (CPT) using a material point method (MPM) simulation. The main research question was:

*‘Can the installation effects, which are the result of a cone pressuremeter penetrating the soil, be accurately modelled in a 2D-axisymmetric model using the material point method?’*

In the presented research, a 2D-axisymmetric MPM simulation of a CPT has been established in order to better understand the installation effects encountered in the soil when installing the CPT. The use of MPM has allowed recent research to simulate the entire installation process of a CPT where previously finite element method (FEM) calculations could not accurately model the installation process due to issues like mesh entanglement. This research consisted of three parts: (1) Verification of the model, (2) Validation of the model and (3) Sensitivity analysis. Each component is linked to one of the three subquestions established in Chapter 1 and from these components the conclusions listed below can be drawn.

The presented MPM model has been verified by systematically examination of the model’s capabilities and limitations. From the verification it was concluded that from the available elastic-plastic constitutive models, namely Mohr-Coulomb (MC), Hardening Soil (HS) and Mohr-Coulomb Strain Softening (MCSS), the MCSS was most well-suited for this type of simulation. The MC model can not account for any hardening or softening behaviour and was therefore deemed too simplistic of this research. Given the fact that for larger strains softening of soil becomes more and more important to accurately capture a realistic soil behaviour, the HS model was not suited since it can not account for the softening of the soil. In contrast, the MCSS model is able to simulate softening behaviour is was therefore deemed to be the most appropriate constitutive model. It must be noted, however, that it was found that the stiffness of the soil has the largest influence on the numerical prediction and that this stiffness is constant and independent of the stress state in the MCSS constitutive model. We know that the stiffness of the soil is in fact not constant and in fact stress dependent. Therefore, a significant portion of the information is lost by using this constitutive model. This could be seen in the comparison of the accumulated strains between the MPM model and the experimental data. The qualitative behaviour was in agreement but quantitatively speaking, there were discrepancies. The development of strains is largely dependent of the stiffness so if the stiffness is not accurately modelled, it follows that the development of the strains will not be accurately modelled.

In the modelling process, mesh dependencies seemed unavoidable which introduce some level of errors in the simulation. Several steps were taken, for example different element types or sizes, to counteract the mesh dependencies but proved ultimately unsuccessful to completely mitigate the mesh dependencies.

In terms of boundary effects, it was found that for a cone with a radius of 0.02185m, a radial distance of 2.0m was needed in order to mitigate most of the boundary effects. This would amount to a minimum radial distance of 45.8D. For the depth of the model it was found that for a penetration depth of 1.0m, the minimum required depth to mitigate the bottom boundary effects was 3.0m or 68.6D. It must be noted however that no additional models were created with a different cone radius to verify these normalized values.

A MPM model with this size and refinement does come with the downside that the calculation time increases significantly. While the use of the 2D-axisymmetric formulation does reduce the computational effort significantly since only a 2D model has to be simulated instead of a slice in 3D, a specific calculation method, MPM-Mixed, had to be used which averages the state parameters per element. Without this calculation method, simulation time neared 100 hours while using the MPM-Mixed method reduced the calculation time by roughly 90%. The cost of this was some numerical inaccuracies when using the MCSS constitutive model but these inaccuracies were not significant enough not to use MPM-Mixed.

Several steps have been taken in the validation process of the model. The material properties were chosen to represent the same soil as the soil used in the laboratory test. However, the cone resistance profile obtained from the MPM model did not fully agree with the cone resistance profile from the calibration chamber test. This can be attributed to several sources. Firstly, the chosen constitutive model could not capture the complete soil behaviour. The laboratory tests showed that significant particle crushing took place during the cone penetration. This particle crushing effect is a behavioural aspect of the soil which is not taken into account with the MCSS constitutive model. Furthermore, the stress dependency of stiffness is not accounted for in the MCSS model which can account for the numerical differences found in the comparison of the strain paths. The qualitative behaviour of the strain developments did show to be in good agreement and it therefore can be stated that the difference are the results of erroneous parameters and possibly the lack of a stress dependent stiffness in the model. Another source of errors could be that the boundary conditions imposed on the model did not fully match with the experiments.

By utilizing one of the principles of the Mohr-Coulomb based models, the plastic radius could be determined at any cross-section of model by looking at the Mohr circle in the Mohr space. The obtained plastic radius was compared to the analytical solution by Baguelin et al. (1978) based on the cavity expansion theory and it was found that this analytical solution overestimates the plastic radius by 18%. The analytical solution always overestimated the plastic radius and can therefore be used as a upper boundary value. It was found that further away from the created cavity, the vertical stress became the major principle stress instead of the radial stress where the deviatoric stress between the vertical and the tangential stress was driving the plasticity. This highlights one of the limitations of the analytical solution by Baguelin et al. (1978) which does not include the vertical stress component.

From the sensitivity analysis it was found that the soil stiffness contributed the most to the numerical predictions. Since the stiffness of the sand can vary significantly based on the density state of the sand, extra attention has to be spend on selecting a representative value. The same holds up for the other parameters considering one of the basic principles of numerical modelling, 'Garbage in = Garbage out', but the influence of the peak friction angle for example was a lot less present. The reason being that the friction angle softened quickly from the peak friction angle to the residual friction angle due to the stress state increase underneath the cone which reduced the impact of the variation in the peak friction angle.

Concluding, it can be stated that the material point method, and especially the 2D-axisymmetric formulation, has the potential to be a good tool for modelling the installation process of a cone and for better understanding the behaviour of the installation effects accompanying the process. Setting up the model and the verification does take time and experience to ensure that the model behaves as intended. It does also require a good method of validation is you want to use it as a numerical prediction. It should be noted that this research is limited to the use of elastic-plastic model and while it allowed for additional methods of verification in the form of the cavity expansion theory which is based on the same principles, some aspects of the soil could not be captured by the used constitutive model.

## 6.2 Recommendations

Continuing from the final conclusion, it was stated that the used constitutive model did not capture every aspect of the soils behaviour which was observed in laboratory tests. As mentioned before, only a select number of constitutive models were considered in this research. Further research could be conducted in the modelling of the installation effects using other constitutive models. Especially using critical state based models could prove to be an interesting addition to this field of research since the large amount of strains could cause inaccuracies when a state independent model is chosen. Furthermore, when new constitutive models are implemented into the used MPM code, it will enable further research into the modelling of the cone penetration process. For example, a constitutive model which is especially developed to model particle crushing (Phuong, 2019) would be an interesting addition to this field of work given that during calibration chamber testing, it was found that particle crushing does occur during the penetration process. The most valuable addition in terms of constitutive models would be using a constitutive model which incorporates the stress dependency of the stiffness given that the stiffness has the largest influence on the results as previously mentioned.

One of the goals of this research was to find the plastic radius of soil. As it turned out, finding which parts of the soil experienced plasticity at any given point of the simulation was not straightforward. However, it should be able to extract this information from the model given that the elastic and plastic strains are calculated separately. One possibility could be to add flags to each of material points which simply state whether a material point is in an elastic, plastic or unloading/reloading state. If these flags are then plotted in the post-processing software, it would give a clear overview of the different zones in the soil and the plastic radius could more easily be determined.

Given the fact that this research was focused on modelling one specific case of a cone penetration process, it would be wise to broaden this research to investigate the functioning of the MPM model under different boundary conditions. This could be under a different surcharge to, for example, simulate the deep penetration process. Alternatively, a very low surcharge could be imposed to investigate the free surface movement. Different soil types and eventually a layered soil system would also be an interesting research topic. With every set of boundary conditions for which the MPM model is successfully verified, the reliability of the MPM model increases.

As mentioned in the conclusions, the logical steps in the validation process have been taken and the qualitative behaviour of the sand has been shown to be in agreement. In contrast, the quantitative behaviour was not in agreement on several fronts. The most likely reason is the some of the missing aspects in the used constitutive model. It is difficult to validate a MPM model with large strains once non-linearity's arise since no analytical solutions can be used to validate. In the opinion of the author the most logical next step in the validation process is to use a constitutive model which can more accurately capture the stress dependency of the stiffness. Furthermore, in this research some difficulties arose in determining the parameters since the experimental data was used from another research which lacked some of the essential information. It would therefore be better to set up a more elaborate research in which the laboratory experiments and especially the data acquired from these experiments are designed to better suit the validation process of the MPM model.

## References

- Ali, E. M., Osman, M. A., & Abuelhassan, M. B. (2016). Field measurement of shear modulus of hard clays a case study of kosti thermal power plant project, sudan. *Journal of Building and Road Research*, 12(1).
- Arshad, M., Tehrani, F., Prezzi, M., & Salgado, R. (2014). Experimental study of cone penetration in silica sand using digital image correlation. *Géotechnique*, 64(7), 551–569.
- Baguelin, F., Jézéquel, J.-F., & Shields, D. H. (1978). *The pressuremeter and foundation engineering* (Vol. 2). Trans Tech Publications Clausthal, Germany.
- Baligh, M. (1986a). Undrained deep penetration, ii: pore pressures. *Géotechnique*, 36(4), 487–501.
- Baligh, M. (1986b). Undrained deep penetration, i: shear stresses. *Géotechnique*, 36(4), 471–485.
- Bellotti, R., Ghionna, V., Jamiolkowski, M., Robertson, P., & Peterson, R. (1989). Interpretation of moduli from self-boring pressuremeter tests in sand. *Géotechnique*, 39(2), 269–292.
- Bolton, M. (1986). Strength and dilatancy of sands. *Géotechnique*, 36(1), 65–78.
- Bolton, M., & Whittle, R. (1999). A non-linear elastic/perfectly plastic analysis for plane strain undrained expansion tests. *Géotechnique*, 49, 133–141.
- Brinkgreve, R. (2018). *Materiaalmodellen voor grond en gesteente; lecture notes in behaviour of soils and rocks*. Technische Universiteit Delft.
- Cambridge Insitu. (2018). *Using pressuremeters*. (Technical guide)
- Cambridge Insitu. (2019). *Cone pressuremeter handbook*. (Technical guide)
- Ceccato, F., Beuth, L., & Simonini, P. (2016). Analysis of piezocone penetration under different drainage conditions with the two-phase material point method. *Journal of Geotechnical and Geoenvironmental Engineering*, 142(12), 04016066.
- Ceccato, F., Chmelnizkij, A., Di Carluccio, G., Fern, J., Marveggio, P., Murphy, J., ... Zambrano-Cruzatty, L. (2019). *Anura3d MPM software, tutorial manual*. Anura3D MPM Reseach Community c/o Stichting Deltares, Delft.
- Ceccato, F., Chmelnizkij, A., Di Carluccio, G., Fern, J., Marveggio, P., Pinyol, N., ... Yerro, A. (2019). *Anura3d MPM software, scientific manual*. Anura3D MPM Reseach Community c/o Stichting Deltares, Delft.
- Chen, W.-F. (2013). *Limit analysis and soil plasticity*. Elsevier.
- Clarke, B. G. (2014). *Pressuremeters in geotechnical design*. CRC Press.
- Courant, R., Friedrichs, K., & Lewy, H. (1967). On the partial difference equations of mathematical physics. *IBM journal of Research and Development*, 11(2), 215–234.
- Detournay, C., & Dzik, E. (2006). Nodal mixed discretization for tetrahedral elements. In *4th international FLAC symposium on numerical modeling in geomechanics* (Vol. 7).
- Fern, J., Rohe, A., Soga, K., & Alonso, E. (2019). *The material point method for geotechnical engineering: A practical guide*. CRC Press.
- Galavi, V., Tehrani, F., Martinelli, M., Elkadi, A., & Luger, D. (2019). Axisymmetric formulation. In J. Fern, A. Rohe, K. Soga, & E. Alonso (Eds.), *The material point method for geotechnical engineering: a practical guide* (p. 89-100). Boca Raton: CRC Press, Taylor & Francis Group.
- Harlow, F. H. (1962). *The particle-in-cell method for numerical solution of problems in fluid dynamics* (Tech. Rep.). Los Alamos Scientific Lab., N. Mex.
- Houlsby, G., & Withers, N. (1988). Analysis of the cone pressuremeter test in clay. *Géotechnique*, 38(4), 575–587.
- Jefferies, M., & Shuttle, D. (1995). Disturbance does not prevent obtaining reliable parameters from sbp tests in clay. In *The pressuremeter and its new avenues, proc., of the 4th int. symp. on pressuremeters* (pp. 177–183).
- Jezequel, J., Lemasson, H., & Touze, J. (1968). Le pressiomètre louis ménard: Quelques problèmes de mise en oeuvre et leur influence sur les valeurs pressiométriques. *Bull. De Liaison du LCPC*(32), 97–120.
- Moug, D. M., Boulanger, R. W., DeJong, J. T., & Jaeger, R. A. (2019). Axisymmetric simulations of cone penetration in saturated clay. *Journal of Geotechnical and Geoenvironmental Engineering*, 145(4), 04019008.

- Obrzud, R., & Truty, A. (2012). The hardening soil model-a practical guidebook z soil. *PC100701 Report*.
- Pantev, I. (2016). Contact modelling in the material point method (master thesis). Available at <https://repository.tudelft.nl/>.
- Phuong, N. (2019). Numerical modelling of pile installation using material point method (doctoral thesis). Available at <https://repository.tudelft.nl/>.
- Phuong, N., van Tol, A., Elkadi, A., & Rohe, A. (2014). Modelling of pile installation using the material point method (MPM). *Numerical Methods in Geotechnical Engineering*, 271, 276.
- Prapaharan, S., Chameau, J., Altschaeffl, A., & Holtz, R. (1990). Effect of disturbance on pressuremeter results in clays. *Journal of Geotechnical Engineering*, 116(1), 35–53.
- Prapaharan, S., & Thevanayagam, S. (1989). Discussion of “rate effects in pressuremeter tests in clays” by W.F. Anderson, I.C. Pyrah, and F.H. Ali (november, 1987, vol. 113, no. 11). *Journal of Geotechnical Engineering*, 115(5), 749–752.
- Roscoe, K. H., Schofield, A., & Wroth, C. (1958). On the yielding of soils. *Géotechnique*, 8(1), 22–53.
- Salgado, R., & Prezzi, M. (2007). Computation of cavity expansion pressure and penetration resistance in sands. *International Journal of Geomechanics*, 7(4), 251–265.
- Salgado, R., Prezzi, M., Kim, K., & Lee, W. (2013). Penetration rate effects on cone resistance measured in a calibration chamber. In *Geotechnical and geophysical site characterization: Proceedings of the 4th international conference on site characterization ISC-4* (Vol. 1, pp. 1025–1030).
- Schweiger, H. (2017). *An introduction to numerical modelling in geotechnical engineering*. ISSMGE.
- Silvestri, V. (2004). Disturbance effects in pressuremeter tests in clay. *Canadian geotechnical journal*, 41(4), 738–759.
- Sulsky, D., Chen, Z., & Schreyer, H. L. (1994). A particle method for history-dependent materials. *Computer methods in applied mechanics and engineering*, 118(1-2), 179–196.
- Sulsky, D., & Schreyer, H. L. (1996). Axisymmetric form of the material point method with applications to upsetting and taylor impact problems. *Computer Methods in Applied Mechanics and Engineering*, 139(1-4), 409–429.
- Teh, C., & Houlsby, G. (1991). An analytical study of the cone penetration test in clay. *Géotechnique*, 41(1), 17–34.
- Tehrani, F. S., & Galavi, V. (2018). Comparison of cavity expansion and material point method for simulation of cone penetration in sand. In *Cone penetration testing 2018* (pp. 611–615). CRC Press.
- White, D., & Bolton, M. (2004). Displacement and strain paths during plane-strain model pile installation in sand. *Géotechnique*, 54(6), 375–397.
- Whittle, R. (1995). The relationship between simple strain and true strain.
- Whittle, R., & Liu, L. (2013). A method for describing the stress and strain dependency of stiffness in sand. In *Proceedings of the 18th international conference on soil mechanics and geotechnical engineering, Paris, parallel session ISP* (Vol. 6).
- Wierzbicki, T. (2013). *The concept of strain; lecture notes in structural mechanics*. Massachusetts Institute of Technology.
- Withers, N., Howie, J., Hughes, J., & Robinson, P. (1989). Performance and analysis of cone pressuremeter tests in sands. *Géotechnique*, 39(3), 433–454.
- Zhang, Z. C. X., Lian, Y., Liu, Y., & Zhou, X. (2017). *Material point method*. Elsevier.
- Zuidberg, H., & Post, M. (1995). The cone pressuremeter: An efficient way of pressuremeter testing. In *Proc. 4th int. symp. on pressuremeter testing (ISP-4), “the pressuremeter and its new avenue” balkema* (pp. 387–394).



# Appendices



## A Meshes Used for Mesh Refinement Analysis

Figure A.1 and A.2 shows the different refinement steps of the elements near the cone. These models were used in the determination of the appropriate mesh refinement.

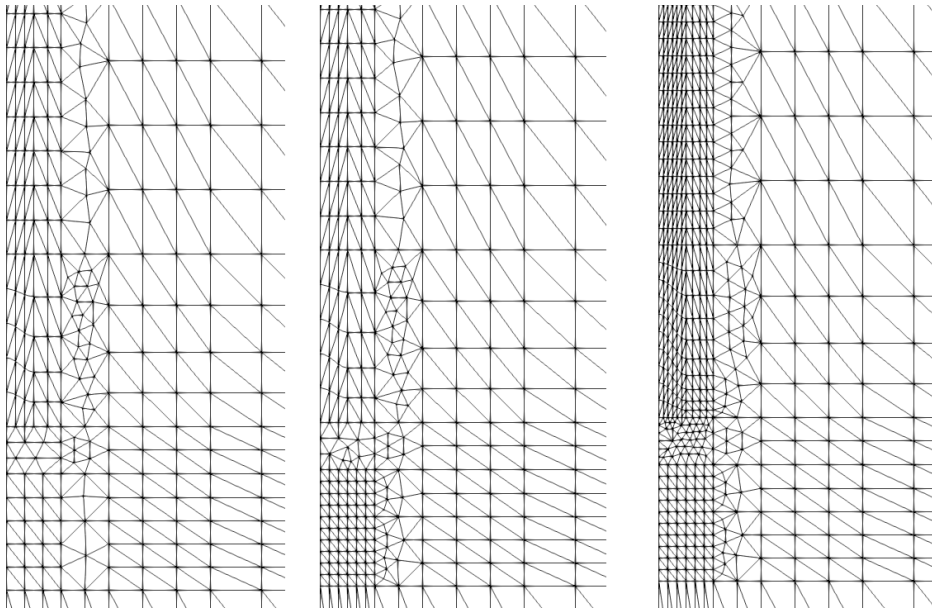


**Figure A.1:** Meshes for models MR1, MR2 and MR3 (from left to right)

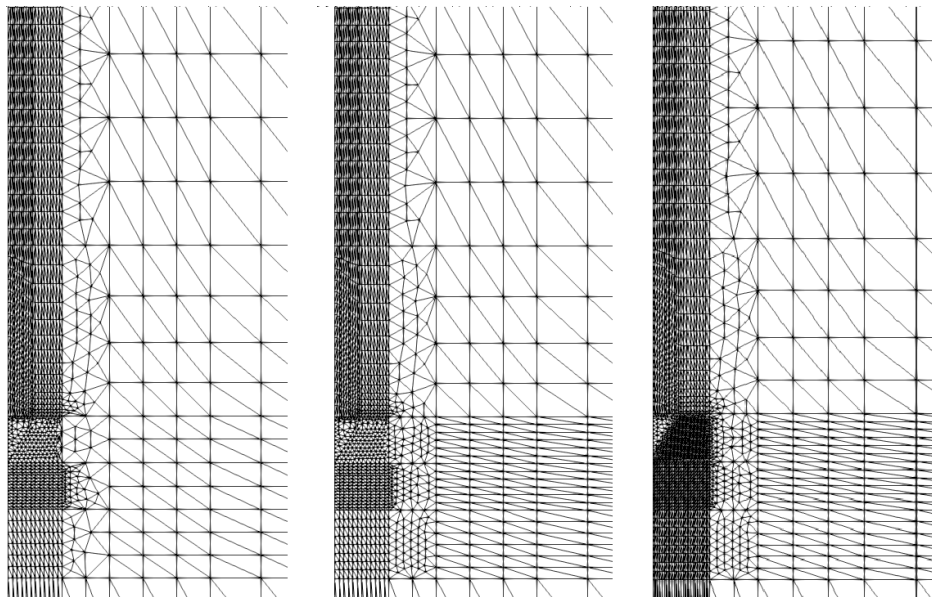


**Figure A.2:** Meshes for models MR4, MR5 and MR6 (from left to right)

## B Final Mesh

Figure A.3 shows the final mesh used in the validation and the sensitivity analysis. Given the size of the mesh and the required refinement it is difficult to distinguish the elements in the finer regions. Therefore, Figure A.4 shows the mesh refinement near the cone.

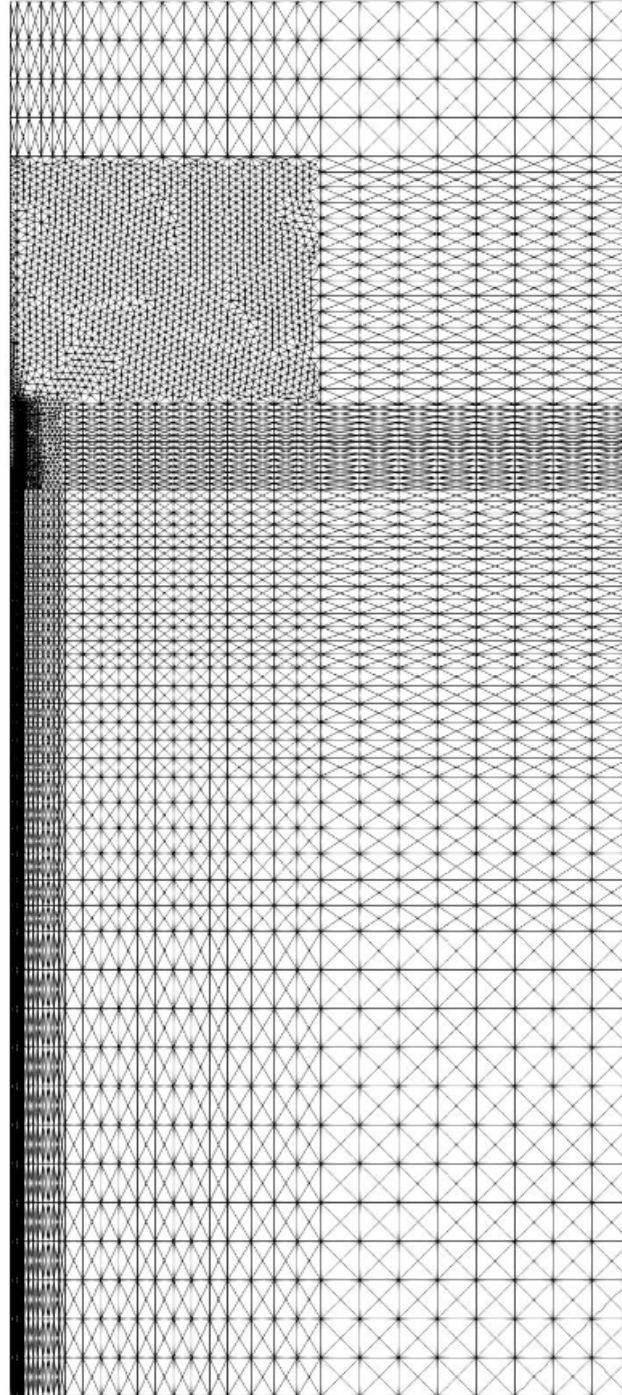


**Figure A.3:** Full mesh

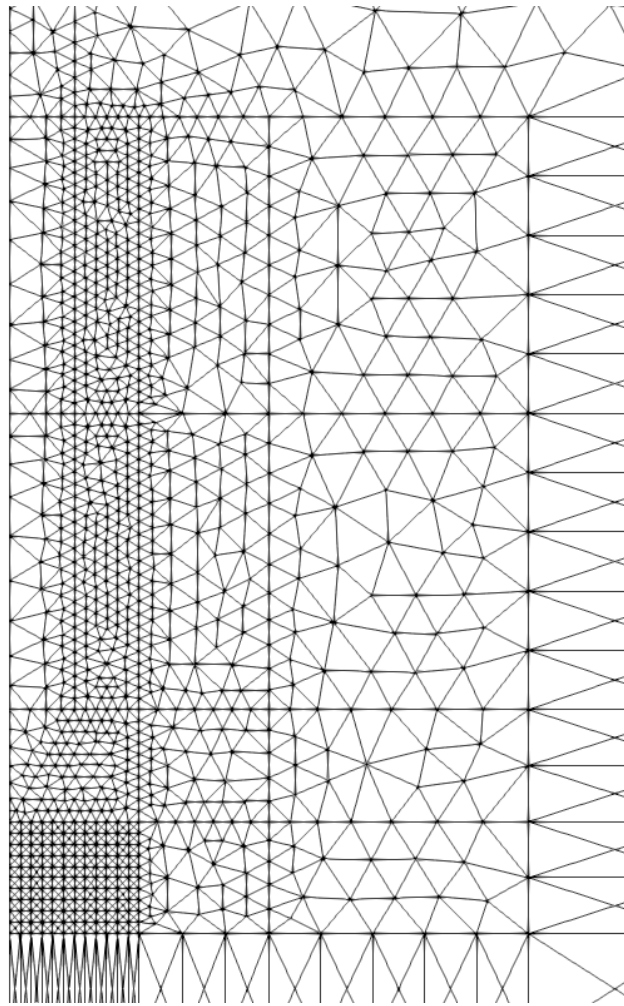


**Figure A.4:** Zoomed view of the mesh near the cone

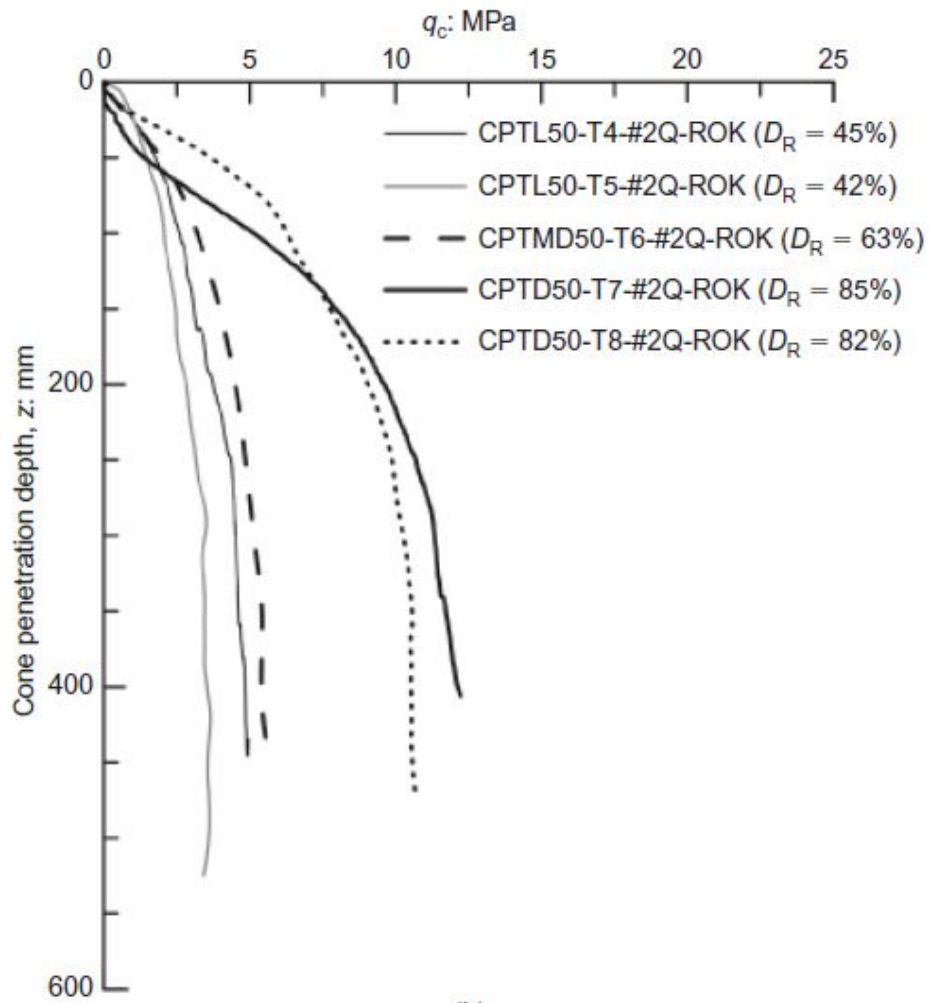
### C Test Series Performed by Arshad et al. (2014)

Figure A.5 shows the test serie performed by Arshad et al. (2014). The interest for this research were tests T4 through T8. Figure A.6 shows the resulting cone resistance profiles for these tests.

Test Code	Surcharge (kPa)	Initial void ratio $e$	Relative Density $D_R$ (%)	$d_c/D_{50}$	$d_{chamber}/d_c$
CPTL0-T1-#2Q-ROK	0	0.849	45	41.0	53.0
CPTMD0-T2-#2Q-ROK	0	0.783	65		
CPTD0-T3-#2Q-ROK	0	0.718	85		
CPTL50-T4-#2Q-ROK	50	0.849	45		
CPTL50-T5-#2Q-ROK	50	0.855	42		
CPTMD50-T6-#2Q-ROK	50	0.790	63		
CPTD50-T7-#2Q-ROK	50	0.718	85		
CPTD50-T8-#2Q-ROK	50	0.7252	82		
CPTD50-T9-Ohio Gold Frac	50	0.578	87	53.0	85.0
CPTD50-T10-ASTM 20-30	50	0.538	85	49.0	
CPTD50-T11-Mini-#2Q-ROK	50	0.849	45	25.0	85.0
CPTL50-T12-Mini-#2Q-ROK	50	0.718	85		
CPTL0-T13-#2Q-ROK	0	0.932	20	41.0	53.0
JPL0-T14-Flat-#2Q-ROK	0	0.932	20		

<sup>1</sup>L = loose; MD = medium dense; D = dense

**Figure A.5:** Test serie performed by Arshad et al. (2014)



**Figure A.6:** Cone resistance,  $q_c$ , for tests with a 50kPa surcharge (Arshad et al., 2014)

### D Strain paths of elements in MPM model

Figures A.7 through A.10 shows the strain path comparisons between the  $D_R = 45\%$  MPM model and the corresponding experiments performed by Arshad et al. (2014).

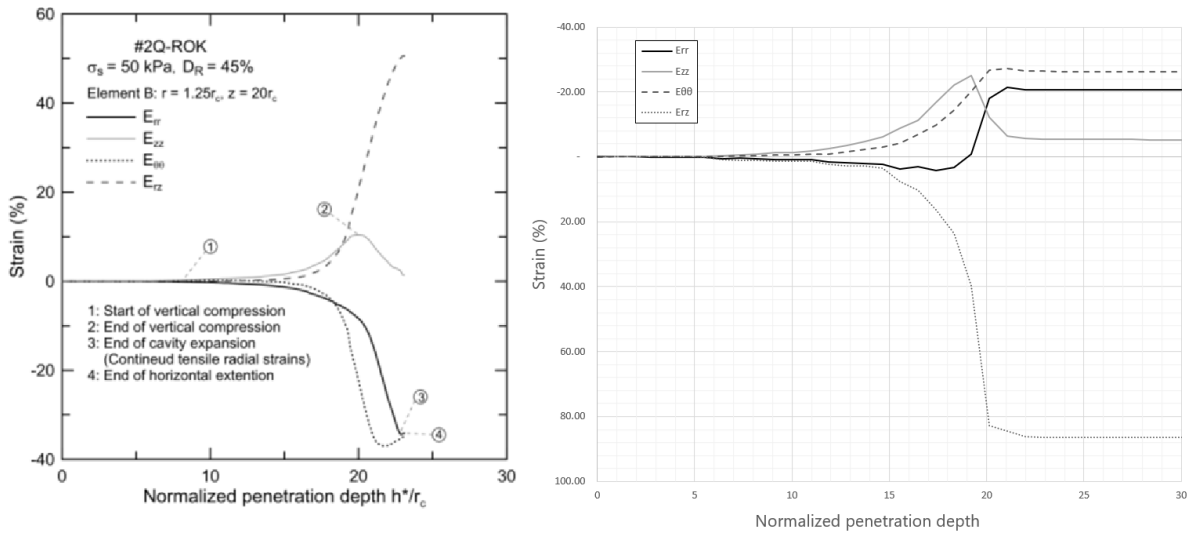


**Figure A.7:** Strain paths comparison for element B. Left: experiments; Right: MPM model

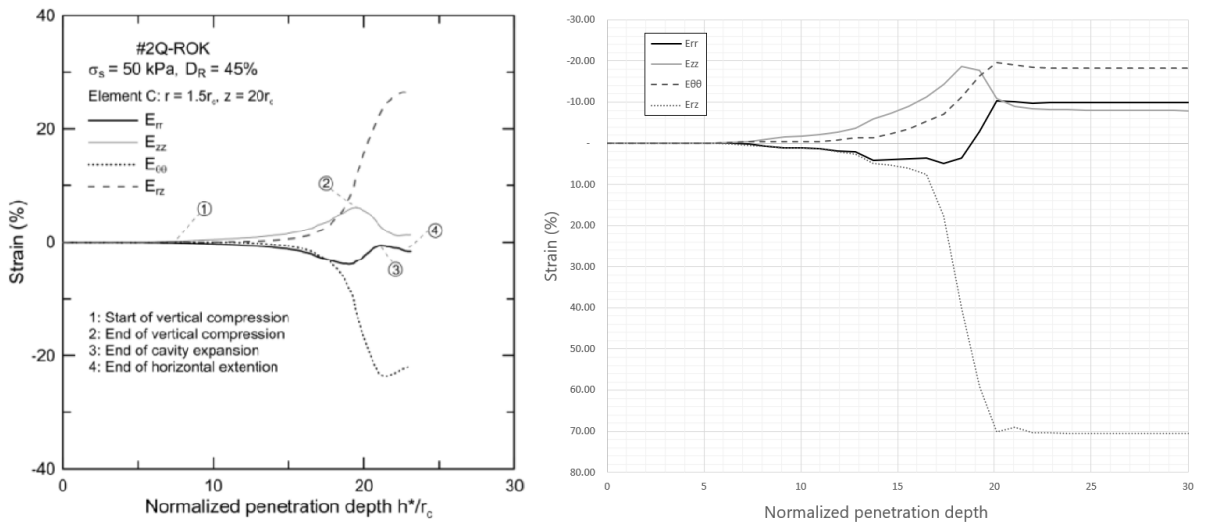


**Figure A.8:** Strain paths comparison for element C. Left: experiments; Right: MPM model

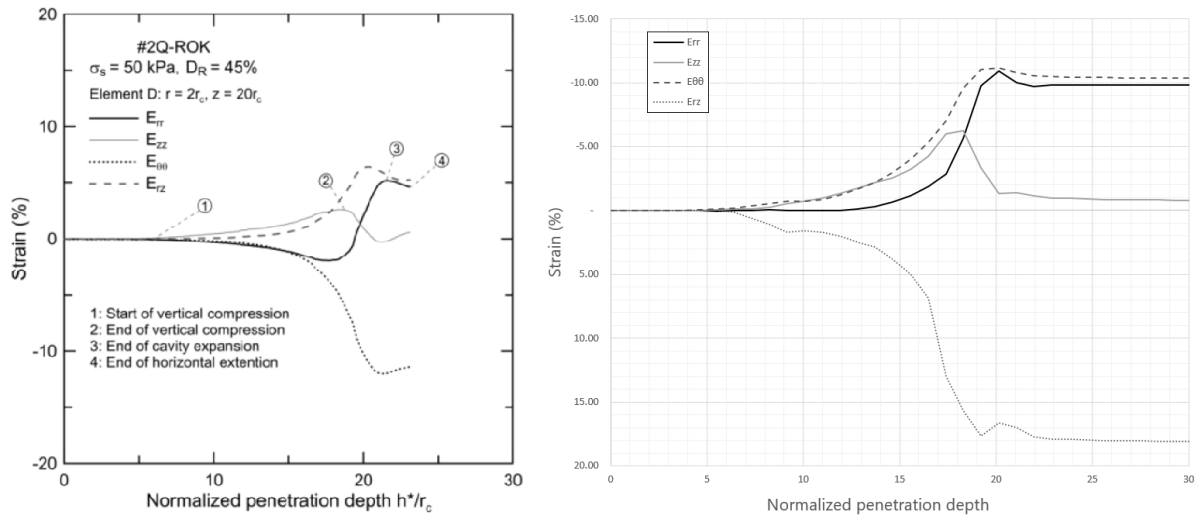


Figure A.9: Strain paths comparison for element D. Left: experiments; Right: MPM model

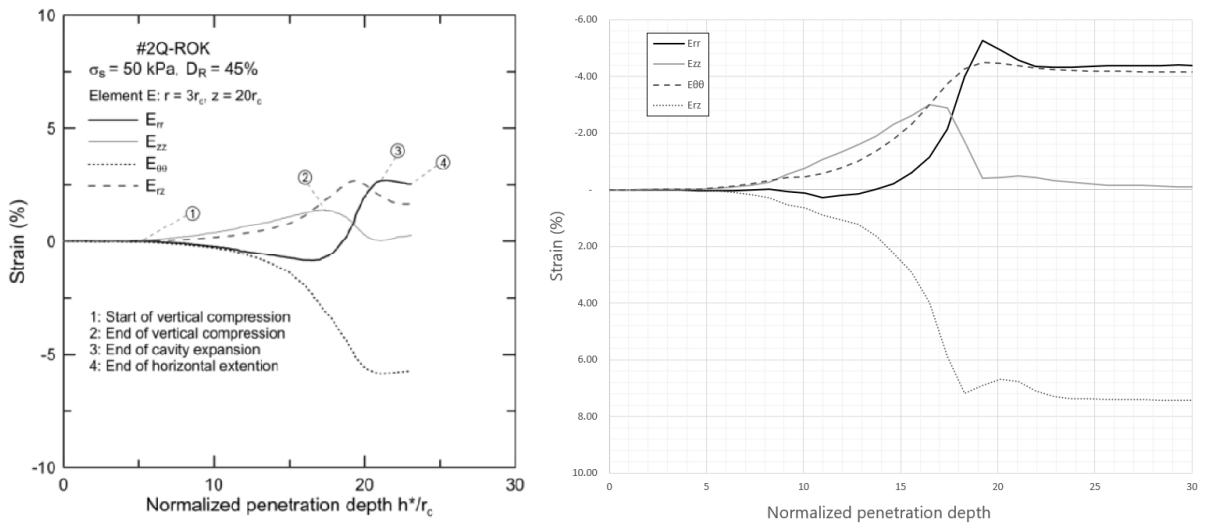


Figure A.10: Strain paths comparison for element E. Left: experiments; Right: MPM model